Travail de fin d'études et stage[BR]- Travail de fin d'études : Energy converter integration study in a series hybrid powertrain[BR]- Stage d'insertion professionnelle

Auteur : Delanaye, Louis
Promoteur(s) : Lemort, Vincent
Faculté : Faculté des Sciences appliquées
Diplôme : Master en ingénieur civil mécanicien, à finalité spécialisée en technologies durables en automobile
Année académique : 2020-2021
URI/URL : http://hdl.handle.net/2268.2/11392

Energy converter integration study in a series hybrid powertrain

Master thesis submitted in partial fulfillment of the requirements for the Degree of Master in Mechanical engineering (Sustainable Automotive Engineering) by

Louis DELANAYE

University of Liege - Faculty of Applied Sciences

Promotor : Lemort Vincent

Academic year 2020-2021

Acknowledgements

This work could not have been done on my own. I would like to thank several people for their support and good counsel.

Firstly, I want to thank my internship supervisor, Wissam Bou Nader, for the opportunity of working for such a great company as STELLANTIS and to supervise my work as closely as he did.

Secondly, I would like to thank Professor Vincent Lemort, my Master thesis's promoter, for performing a monthly review of the work advancement. I also thank Professor Nathalie Job whose fuel cells explanations helped me a lot. I eventually thank them all, as well as Professor Pierre Duysinx, for their time spent reading and evaluating this master thesis.

Thirdly, I thank all my family and especially my parents for their review of this final thesis but also for their support and help all along these five years at University.

Eventually, I thank all of the persons who made me criticize, develop ideas and improve my work along this internship.

Contents

List of Figures

List of Tables

Acronyms

CH_4	Methane.
CO	Carbon Monoxide.
CO_2	Carbon Dioxide.
H_2	Hydrogen.
H_2O	Water.
N_2	Nitrogen.
O_2	Oxygen.
atm	Atmospheric pressure.
CC	Combustion Chamber.
cp	Compressor.
Eq	Equation.
FC	Fuel Cell.
Fig	Figure.
gen	Generator.
GR	Global Reforming.
GT	Gas Turbine.
heat	Heater.
HEX	Heat Exchanger.
HT-SOFC	High Temperature Solid Oxide Fuel Cell.
i	Inlet.
IRSOFC	Indirect Reforming Solid Oxide Fuel Cell.
IT-SOFC	Intermediate Temperature Solid Oxide Fuel Cell.
LSM	Lanthanum Strontium Manganite.
LT-SOFC	Low Temperature Solid Oxide Fuel Cell.
MM	Molar mass.
o	Outlet.

SR	Steam Reforming.
TC	Turbocharger.
tot	Total.
tu	Turbine.
WGS	Water Gas Shift.
YSZ	Yttria Stabilized Zirconia.

Glossary

$\dot{\mathrm{H}}$	Enthalpy flow [W].
$\dot{\mathrm{V}}$	Volume flow [$\mathrm{m^3/s}$].
$\dot{\mathrm{m}}$	Mass flow [kg/s].
$\dot{\mathrm{n}}$	Molar flow [mol/s].
ΔG_0	Standard change in free Gibbs energy [J].
ΔH	Change in enthalpy [kJ/mol].
ΔP	Pressure loss [kPa].
δ	Thickness [cm].
η	Efficiency [-].
γ	Pre-exponential factor [$\mathrm{A/cm^2}$].
λ	Air-fuel ratio [-].
ρ	Resistivity [Ω cm].
A	Area [$\mathrm{cm^2}$].
B	Ohmic loss coefficient [K].
c_p	Heat capacity [$\mathrm{kJ/(kg \cdot K)}$].
C_R	Conversion ratio [-].
D	Diffusivity [$\mathrm{cm^2/s}$].
E	Molar energy [J/mol].
e	Air excess [-].
e_c	Elementary charge [C].
F	Faraday constant [C/mol].
h	Specific enthalpy [J/kg].
I	Current [A].
i	Current density [$\mathrm{A/cm^2}$].
K	Equilibrium constant [-].
LHV	Net heating value [J/kg].

M	Mass [kg]].
N_A	Avogadro number [1/mol].
N_{cells}	Number of cells [-].
nb_{el}	Number of electrons [-].
O	Ohmic loss coefficient [Ω cm].
p	Pressure [kPa].
P_{el}	Electric power [W].
p_{el}	Electric power density [W/cm^2].
Q	Heat flow [W].
R	Rate (of reaction or formation) [dm^2/s].
R_m	Gas constant [J/mol $\cdot K$].
r_p	Compression/expansion ratio[-].
R_R	Recirculation ratio [-].
s	Entropy [J/(kg · K)].
T	Temperature [K].
U_f	Fuel utilization [-].
V	Voltage [V].
x	Molar fraction [-].

Chapter 1

Introduction

Fuel cells are becoming more and more important for the energy transition [1]. They can offer clean and stable power compared to other renewable energy conversion systems such as photovoltaic, wind, etc. Their efficiency can be further improved when connected to other systems such as gas turbines, steam turbines, etc.

The focus of this master thesis is to evaluate a fuel cell, in particular a solid oxide fuel cell, combined to a micro gas turbine, as a range extender in a series hybrid electric vehicle. For this purpose, a complete thermodynamic modelling tool is developed to predict and compare the performance of various system layouts. The implementation of the tool is performed with MATLAB language. All chemical and thermophysical properties of the fluids are obtained through the REFPROP 9.1 package.

Various SOFC modelling methodologies can be found in the literature as described by Colpan et al. and Zabihian and Fung ([24] [71]). They notably differ from the level of details of the modelling. Indeed, the 0D modelling, or macro-modelling is mainly based on the resolution of the global thermodynamics and electrochemistry equations. This corresponds to a system modelling level which assesses the connection of the SOFC to other systems. This is the approach adopted in this work. Three other types of modelling (1D, 2D and 3D) focus on the simulation of the internal physics of the SOFC. We can refer them to micro-modelling. They are usually not implemented in a system point of view because of the complexity of the problem to solve. In the 1D modelling level, the SOFC is represented as a system with parameters varying along a single geometrical coordinate, and constant in the two other dimensions ([11] [12]). In the 2D modelling level, we simply add a dimension to the equations ([19] [20] [21] [28]). In addition, authors also attempt to combine micro- and macro-modelling to improve the physics representation ([11] [12]). CFD modelling, often used in 3D models, is employed to simulate the detailed physics and be further representative to reality ([42] [43] [65]). Such models were also used to compare in details various types of SOFC, e.g. anode- and cathode-supported SOFC [64].

Multiple combinations of SOFC with gas turbines are described in the literature [13]. Micro-turbine cycles complexity can vary from simple ones such as the recuperative gas turbine (RGT) to more sophisticated such as the intercooled recuperative gas turbine (IRGT) or the intercooled recuperative reheat gas turbine (IRReGT) [9].

The layout of this thesis is organized as follows. Chapter 1 describes the tech-

nology of fuel cells and particularly solid oxide fuel cells, its auxiliary components and potential combination with gas turbines, as well as research and industrial applications. Chapter 2 is focused on the description of the physics of a SOFC stack and its thermodynamic and electrochemistry modelling. Chapter 3 is dedicated to the understanding and modelling of specific fuel processing inside the stack such as the anode gas recirculation while considering other improvements in reforming and water management. As the full SOFC system includes several additional components to the SOFC stack and reformer, Chapter 4 is devoted to the modelling of such auxiliaries. The performance of the full SOFC system is analyzed in Chapter 5. The connection between the SOFC system and the gas turbine is studied in Chapter 6. Eventually, this work is concluded by a brief technological analysis of the integration of the system in a series hybrid electrical vehicle in Chapter 7.

1.1 Fuel cell

A fuel cell is a device capable of directly converting a fuel into electricity using an electrochemical process. It is an open system in which fuel enters at the anode and air at the cathode. Fuel and air are the reactants. The products are composed of the unreacted fuel, the remaining air and water.

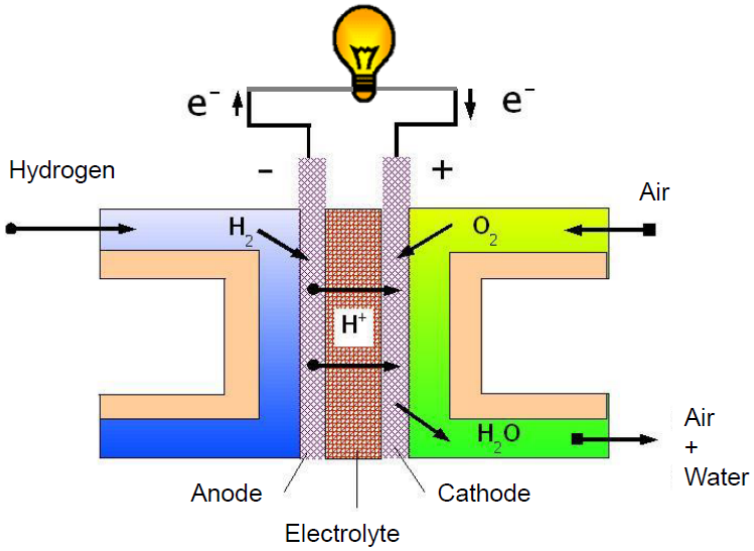

Figure 1.1: Schema of a fuel cell [41].

The fuel cell is actually the location of two independent reactions. The first one takes place at the anode and consists of the oxidation of hydrogen.

$$\begin{array}{lcll} H_2 & \rightarrow & 2H^+ + 2e^- & \text{Acid electrolyte} \\ H_2 + 2OH^- & \rightarrow & 2H_2O + 2e^- & \text{Basic electrolyte} \end{array} \tag{1.1}$$

The second one takes place at the cathode and corresponds to the reduction of oxygen.

$$\begin{array}{lcll} \frac{1}{2}O_2 + 2H^+ + 2e^- & \rightarrow & H_2O & \text{Acid electrolyte} \\ \frac{1}{2}O_2 + H_2O + 2e^- & \rightarrow & 2OH^- & \text{Basic electrolyte} \end{array} \tag{1.2}$$

The balance equation stands as follows with the reaction being exothermic and releasing heat.

$$H_2 + \frac{1}{2}O_2 \rightarrow H_2O + \text{heat}$$

Various fuel cell technologies exist, and differ through notably materials used, operating temperatures, architectures, conversion efficiencies and fuel. The following list gives an overview of all the technologies. Fig. 1.2 classifies the technologies in function of their operating temperature.

AFC	:	Alkaline Fuel Cell
PEMFC	:	Polymer Exchange Membrane Fuel Cell
DMFC	:	Direct Methanol Fuel Cell
DBFC	:	Direct Biomass Fuel Cell
PAFC	:	Phosphoric Acid Fuel Cell
MCFC	:	Molten Carbonate Fuel Cell
SOFC	:	Solid Oxide Fuel Cell

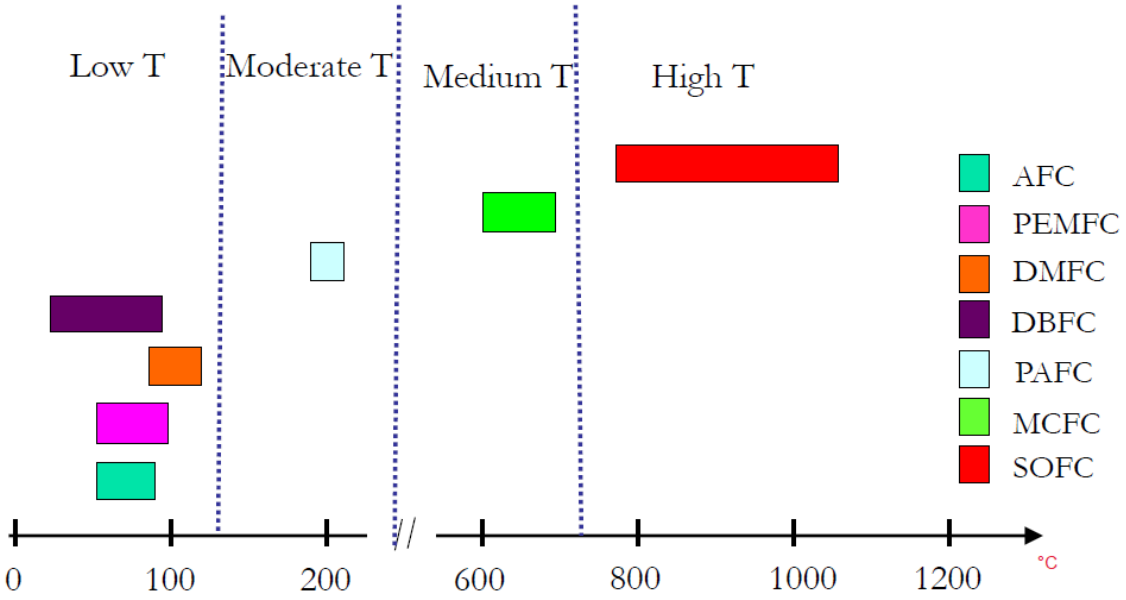

Figure 1.2: Technologies of fuel cells according to their operating temperature [31].

Fuel cells are low pollutant devices, have no moving parts and have low maintenance. They are reliable, induce no noise pollution and yield larger efficiencies than conventional conversion systems.

1.2 Solid Oxide Fuel Cell

A solid oxide fuel cell (SOFC) is a particular type of fuel cells operating at very high temperature which makes it suitable for a combination with a gas turbine.

Although, research is also undertaken for SOFC working with protons electrolyte membranes ([29] [48]), in most SOFC, the electrolyte is permeable to oxygen ions and not to hydrogen protons, as illustrated in Fig. 1.3. Therefore, anodic and cathodic reactions are different than Eq. 1.1 and 1.2:

$$\begin{aligned} \text{Anode} &: H_2 + O^{2-} \rightarrow H_2O + 2e^- \\ \text{Cathode} &: \frac{1}{2}O_2 + 2e^- \rightarrow O^{2-} \end{aligned}$$

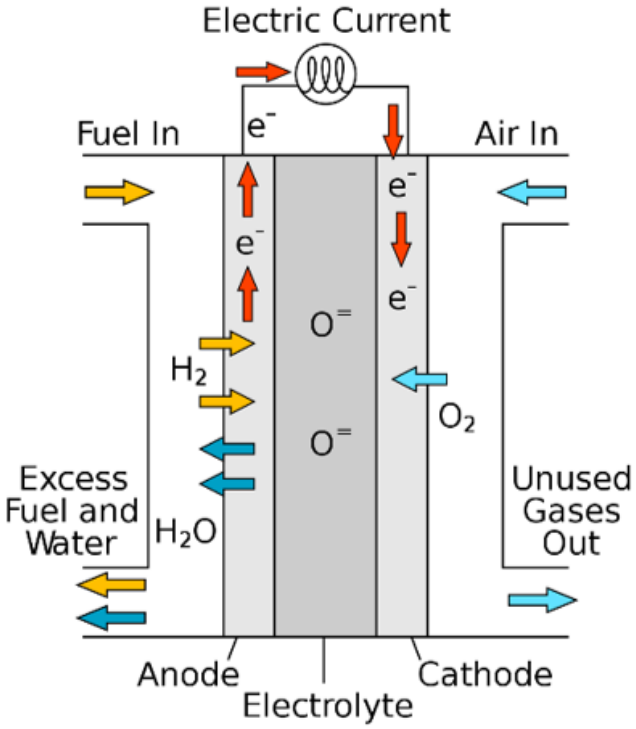

Figure 1.3: Schema of a solid oxide fuel cell [2].

Although its high operating temperature could be seen as a drawback, the SOFC has nevertheless a lot of advantages in comparison to other fuel cells as summarized by Duysinx, Job and Zhang et al. ([31] [41] [72]).

- Higher efficiency

  Solid oxide fuel cells can reach efficiencies as high as 60% [32].

- Fuel flexibility

  Practically all hydrocarbons can be used with SOFC thanks to internal reforming. Focus is put on methane in this study.

- Wide power range

  Prototypes from 200 W until 1 MW are being developed.

- Less sensible to impurities

  Carbon deposition is less an issue in this system thanks to internal reforming. However, sulphur is an absolute poison for this fuel cell, fuel desulphurization is required [57].

- No use of platinum

  No precious metals such as platinum are required as catalyst thanks to the high temperatures.

Some additional drawbacks are related to the materials which can prove expensive, fragile (ceramic) and prone to corrosion.

Additionally, SOFC can be further classified according to operating temperature, cell and stack design, type of support, flow configuration and fuel reforming type [24].

Classification criteria	**Types**
Operating temperature	Low temperature SOFC (LT-SOFC) (500-650°C)
	Intermediate temperature SOFC (IT-SOFC) (650-800°C)
	High temperature SOFC (HT-SOFC) (800-1000°C)
Cell and stack design	Planar SOFC (flat-planar, radial-planar)
	Tubular SOFC (micro-tubular, tubular)
	Segmented-in-series SOFC (or integrated-planar SOFC)
	Monolithic SOFC
Type of support	Self-supporting (anode-, cathode-, electrolyte-supported)
	External-supporting (interconnect-, porous substrate supported)
Flow configuration	Co-flow
	Cross-flow
	Counter flow
Fuel reforming type	External reforming SOFC (ER-SOFC)
	Direct internal reforming SOFC (DIR-SOFC)
	Indirect internal reforming SOFC (IIR-SOFC)

Table 1.1: Classification of solid oxide fuel cells [24].

As far as the materials are concerned, they have to sustain high temperatures while keeping their electrical properties which can represent a difficult challenge. The SOFC contains four parts : anode, cathode, electrolyte and interconnection between cells. Each part has a specific purpose [59]:

- Anode :

  Anode should have a good electrical conductivity as well as thermal expansion compatibility and porosity. Nickel is usually employed while mixed with yttria stabilized zirconia (YSZ) which is also the material of the electrolyte. Mechanical support is sometimes provided by the anode, but other combinations exist and compared e.g. in Su et al. [64].

- Cathode :

  Cathode must have the same characteristics as the anode but essentially porous to allow oxygen to reach the electrolyte. It is affected by a very oxidizing environment and hence requires specific materials. The most commonly used is lanthanum manganite (LaM_nO_3) doped with strontium which is referred by LSM ($La_{1-x}Sr_xM_nO_3$).

- Electrolyte :

  Electrolyte transfers the oxygen ions from the cathode to the anode. It must exhibit a high ionic conductivity and no electrical conductivity. The most suitable material is yttria stabilized zirconia (YSZ).

- Interconnection :

  Interconnection plates must have a 100% electrical conductivity and are exposed to harsh environments at the cathode and the anode, which makes them very prone to mechanical problems. Research has shown that doped lanthanum chromite is a suitable material for this purpose. For low operating temperatures, other alloys such as inconel and stainless steels may be used which decreases the total cost.

Bianco et al. [7] describes in details problems found in SOFC operations. Specific difficulties are notably :

- Cycling :

  Cycling may be an issue related to inappropriate selection of materials and interconnections as concluded by Pan et al. [56]. More information about different types of cycling are found in Hanasaki et al. [35].

- Slow start-up :

  Most commercial products and prototypes slowly increase their temperature until the operating temperature to avoid gradients and stresses. Nevertheless, research is currently undertaken to increase the start-up speed. For example, a 200 W SOFC stack was developed by Bossel [8] which is capable of reaching a temperature of 750°C in less than 5 minutes by using electric heaters.

- Material brittleness :

  Most used materials are ceramic based because of the high temperatures. They are known for their fragile behavior especially under frequent mechanical and thermal shocks and vibrations. This is the reason why they are more common for stationary than mobile applications. However, Delphi is currently developing an auxiliary power unit for trucks and already has a viable prototype [50].

- Lifetime :

  The lifetime of a SOFC is a critical parameter. It can be shortened by rapid material degradation, which may impair the return on investment.

1.3 Reforming

Reforming is an import part of the fuel cell system and more specifically with solid oxide fuel cells. In the latter, the high operating temperature allows to use internal reforming which can bring several benefits such as a reduction in cost and size. Different types of reforming are currently available and their advantages are summarized by Liso et al. and Zabihian and Fung ([45] [71]) and analyzed in details by Barelli et al. [5].

- Steam reforming :

$$CH_4 + H_2O \rightleftharpoons CO + 3H_2$$

Steam reforming is the most commonly used reforming process. It yields a high SOFC electrical efficiency since the molar ratio of the production of H_2 versus CO is the highest among the other reforming techniques. Since it is endothermic, heat released by the anodic exothermic reaction can be recycled. However, a major drawback concerns the additional equipment required such as a heat exchanger or a preheater for the water [63].

- Partial oxydation :

$$CH_4 + \frac{1}{2}O_2 \rightleftharpoons CO + 2H_2$$

Partial oxydation is another type of reforming in which the fuel reacts with a limited amount of oxygen. It is an exothermic process and produces less hydrogen than steam reforming. Research is currently undertaken to improve this technique especially in the reforming of liquid fuels [39].

- Auto-thermal reforming :

Autothermal reforming combines both steam reforming and partial oxydation to take advantage of their respective benefits. Heavy hydrocarbons are reformed using this technique [44].

- Dry reforming :

$$CH_4 + CO_2 \rightleftharpoons 2CO + 2H_2$$

Dry reforming is characterized by a reaction between a hydrocarbon and carbon dioxide. It is interesting from an environmental point of view since it has the advantage to avoid the use of distilled water for steam reforming or air for partial oxidation. Despite being promising, it is a complex technology because of catalyst issues and carbon deposition.

- Tri-reforming :

Tri-reforming combines three reforming processes : steam reforming, partial oxydation and dry reforming and is attractive because of its potential to form a large amount of hydrogen [47].

These types of reforming can be external or internal as represented in Fig. 1.4. In the case of external reforming (a), the reformer is not integrated in the stack. When the reaction is endothermic, an external source of heat is required. In general, it is more often used in large scale stationary systems. Internal reforming can be categorized as indirect (b) or direct (c). In the case of indirect reforming, the reformer is located in the stack before the anode. Heat released by the exothermic anode reaction is directly recycled, which reduces the need for cooling of the stack. It is simpler and less costly than external reforming but can incur temperature gradients. Direct internal reforming is simpler than indirect internal reforming and yields the most efficient systems. Anode integrates catalysts which reform the fuel. Temperature gradients can also appear. Research is currently limited to reforming of methane [22]. Internal reforming allows more efficient systems but faster

material degradation can sometimes occur. Therefore, some authors recommend a combination of external and internal reforming [34].

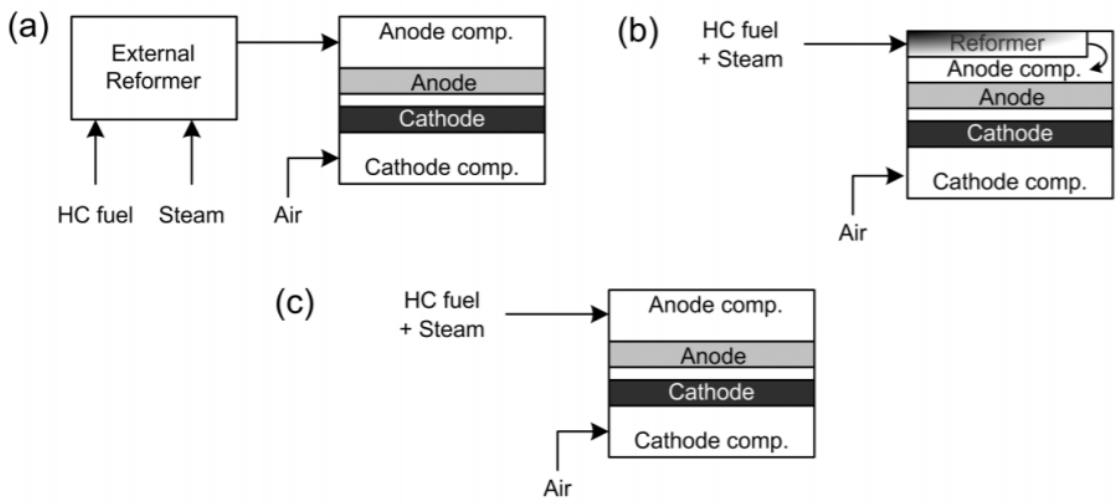

Figure 1.4: Schema of external (a), indirect internal (b) and direct internal (c) fuel reforming [22].

1.4 SOFC and SOFC-GT system

The SOFC system layout is based on a stack, an internal or external reformer, an afterburner and a preheating system of the reactants with heat exchangers and/or electric heaters. Fig. 1.5 shows various layouts for a SOFC system with potential anode and cathode gas recirculation. In household applications, SOFC systems are developed as CHP boilers.

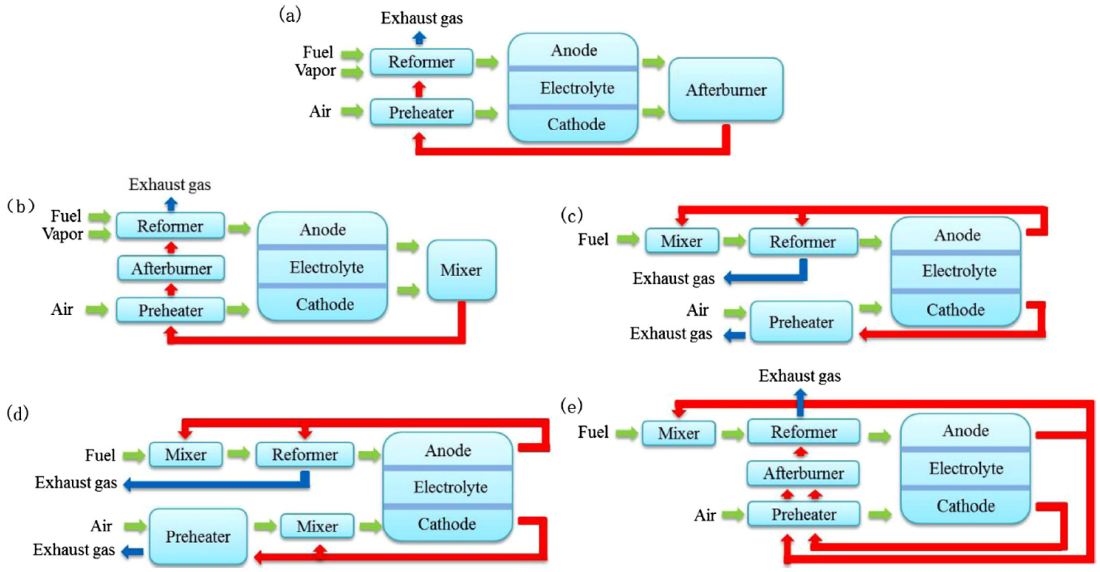

Figure 1.5: SOFC-CHP systems with or without exhaust gas recycle [72].

Many SOFC-GT system layouts are found in the literature and are summarized in Buonomano et al. [13]. Some examples include the IRSOFC-GT layout developed

by Chan et al. [16] shown in Fig. 1.6, two alternative systems described by Chinda and Brault [18] shown in Fig. 1.7 and a system based on the research of Calise et al. [14] shown in Fig. 1.8.

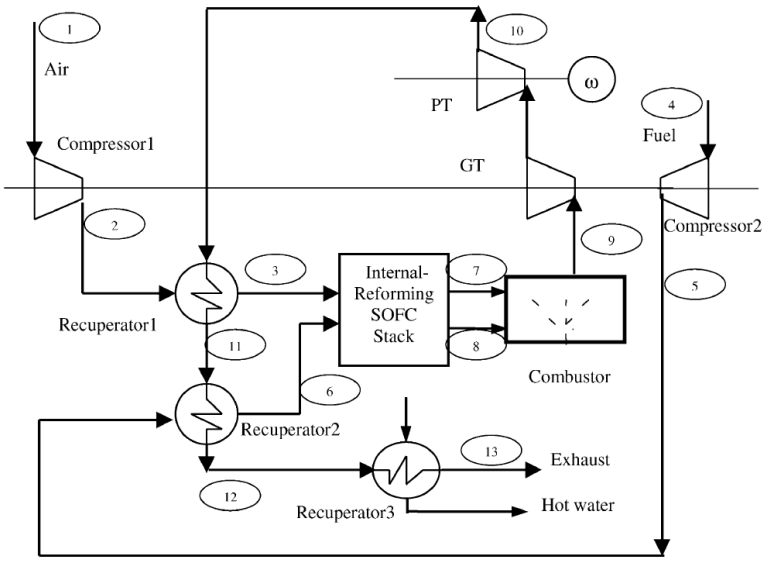

Figure 1.6: Schema of the IRSOFC-GT cycle developed by Chan et al. [16].

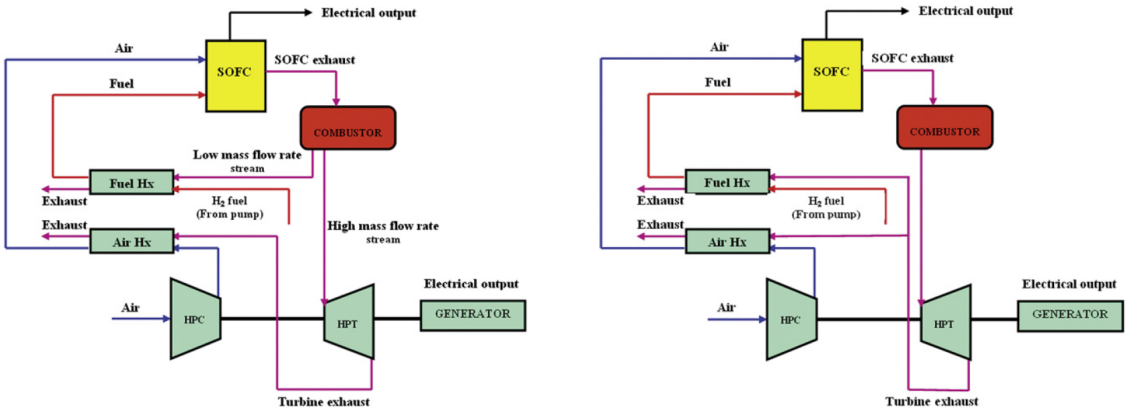

(a) Configuration 1.

(b) Configuration 2.

Figure 1.7: Schema of both configurations developed by Chinda and Brault [18].

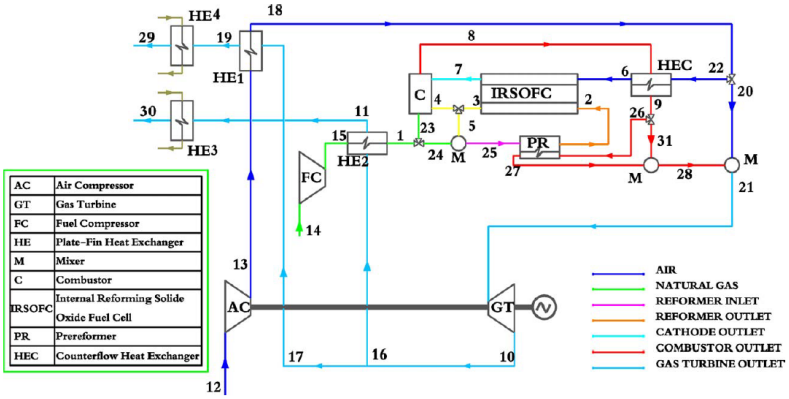

Figure 1.8: Schema of the SOFC-GT cycle developed by Calise et al. [14].

Buonomano et al. [13] conclude their review paper with the following statements:

- Almost all the possible SOFC-GT connections have been investigated in the literature.
- Reforming is mainly done indirect internally but an external pre-reformer is advised. Steam reforming is the most used reforming process while anode recirculation is systematically employed.
- Control of the connection is very complex, especially at part-load operations ([6] [14] [17] [40]).
- Experimental validation in the literature is poor due to the large cost of the stack. Moreover, these tests show unsatisfactory results in comparison to the theoretical ones.
- Focus should be placed on SOFC stack material improvements and low cost manufacturing techniques to further permit their commercialization. Only when these technologies will be widespread and viable, connections shall be investigated.

1.5 Application

Thousands of patents have been filed to improve all aspects of the solid oxide fuel cells. Focus is mostly put on the development of the connection to a gas turbine and on direct internal reforming.

Some actors have already a commercialized product or at least a running prototype. This section summarizes in a non exhaustive list the major actors on the market. A more detailed list of products and market segments can be found in Bianco et al. [7].

Siemens Westinghouse	Rolls Royce Fuel Cell Systems
Mitsubishi Heavy Industries	ZTEK Technology
Elcogen	Convion
Bluegen (Solidpower)	Elringklinger
Nexceris	Kerafol
Bloom Energy Server	Hexis/Viesman
Doosan	mPower GmBH
Bosh Thermotechnology	Sunfire
Atrex	Aisin
Ceramatec	CCTC
Versa Power systems	Huatsing Jingkun
Delphi	MHI
LGFCS	SOFCMAN
MSRI	ULTRA USSI
Adelan	Ceres Power

Table 1.2: Non exhaustive list of market actors [7].

Chapter 2

SOFC stack modelling

This chapter is devoted to the description of the thermodynamics and electrochemistry of the SOFC with the objective to develop a 0D thermodynamic model. It is mainly based on the theory developed by Winkler [68] with additional inputs from [16], [18], [23], [24], [30], [47], [71] and [72]. Since this work is essentially theoretical, we will rely on parameters values found from the literature to obtain a realistic modelling of the stack.

2.1 Main assumptions

Our focus is to assess the performance of steady-state systems. Additional assumptions commonly used in the literature as summarized in Colpan et al. and Zabihian and Fung ([23] [71]) are the following :

- Steady-state conditions :

  A sufficient time has passed to ensure that SOFC operating conditions are stable.

- Isothermal and uniform temperature :

  Inlets and outlets are maintained at the same temperature. This is a reasonable assumption since temperature gradients could damage the electrolyte and reduce the efficiency.

- Isopressure and uniform pressure :

  Pressure losses inside the SOFC are considered negligible.

- Uniform operating voltage :

  Cells have all the same voltage and contribute equally to the stack performance.

- Chemical reaction :

  One of the main assumptions in the development of the model is the fact that hydrogen is the only reactant at the reaction site. Similarly, only oxygen takes part in the reaction. All other gases are inert and only contribute to the partial pressures of the substances.

- Air composition :

  Air is assumed to be only composed of oxygen and nitrogen. Molar percentages are respectively 21% and 79% and mass percentages are 23% and 77%.

- Fuel composition :

  Mixture at anode inlet is only composed of methane, carbon dioxide, carbon monoxide, hydrogen, water and no sulphur. A desulfurization process is assumed to take place outside of the considered system.

- Heat losses to the atmosphere :

  They are considered negligible.

- Kinetic and potential energy :

  They are considered negligible.

2.2 Electrochemistry

As seen before (Section 1.2), the main reaction which takes place in a SOFC is the oxidation of hydrogen. In order to derive the partial pressures, an analysis of the chemical reaction is performed here after.

The reaction in a pure hydrogen and oxygen fuel cell is:

$$H_2 + \frac{1}{2}\, O_2 \rightarrow H_2O \tag{2.1}$$

In general, the mixture present at the anode side is composed of the outlet gases of the reforming process. In that case, methane (CH_4), water (H_2O), carbon monoxide (CO) and carbon dioxide (CO_2) are mixed with hydrogen (H_2). The fluid entering the cathode side is air. Assuming that hydrogen is the only one to react with oxygen, the oxidation reaction is better described by:

$$H_2 + CH_4 + CO + CO_2 + \frac{1}{2}\, O_2 + N_2 + H_2O \rightarrow CH_4 + CO + CO_2 + N_2 + H_2O \tag{2.2}$$

Moreover, hydrogen is never totally consumed before reaching the outlet of the anode, which is defined by the fuel utilization parameter U_f. Its value is usually fixed around 70% with steam reforming [66].

$$U_f = 1 - \frac{\dot{m}_{H_2,o}}{\dot{m}_{H_2,i}} \tag{2.3}$$

Introducing U_f in Eq. 2.2 gives:

$$\begin{aligned} \alpha U_f\ H_2 + \beta\ CH_4 + \gamma\ CO + \delta\ CO_2 + \frac{1}{2}\epsilon\ O_2 + \zeta\ N_2 + \theta\ H_2O \\ \rightarrow \beta\ CH_4 + \gamma\ CO + \delta\ CO_2 + \zeta\ N_2 + \eta\ H_2O \end{aligned} \tag{2.4}$$

where,

α : Number of moles of H_2 at anode inlet
β : Number of moles of CH_4 at anode inlet and outlet
γ : Number of moles of CO at anode inlet and outlet
δ : Number of moles of CO_2 at anode inlet and outlet
$\frac{1}{2}\epsilon$: Number of moles of O_2 needed
ζ : Number of moles of N_2 at cathode inlet and outlet
θ : Number of moles of H_2O at anode inlet
η : Number of moles of H_2O at anode outlet

In equilibrium, the number of moles of O_2, N_2 and H_2O can be deduced by:

$$\begin{aligned} \frac{1}{2}\epsilon &= \frac{1}{2}\alpha U_f \\ \zeta &= 0.5\frac{0.79}{0.21}\alpha U_f \\ \eta &= \theta + \alpha U_f \end{aligned}$$

Reorganizing, Eq. 2.4 becomes:

$$\begin{aligned} \alpha U_f\ H_2 + \beta\ CH_4 + \gamma\ CO + \delta\ CO_2 + \frac{1}{2}\alpha U_f\ O_2 + \frac{1}{2}\frac{0.79}{0.21}\alpha U_f\ N_2 + \theta\ H_2O \\ \rightarrow \beta\ CH_4 + \gamma\ CO + \delta\ CO_2 + \frac{1}{2}\frac{0.79}{0.21}\alpha U_f\ N_2 \\ + (\theta + \alpha U_f)\ H_2O \end{aligned} \quad (2.5)$$

2.2.1 Mass flows

In this model, the mass flow of the fuel entering the reformer is fixed. Depending on different parameters such as length, temperature and pressure, the reformer produces a mixture of methane (CH_4), carbon dioxide (CO_2), hydrogen (H_2), carbon monoxide (CO) and water (H_2O).

The mass flow of oxygen required to have a stoechiometric chemical reaction can then be evaluated using the mass flow of hydrogen.

The stoechiometric relation means that 1 mole of hydrogen reacts with 0.5 mole of oxygen. Using the molar masses of both substances, the mass flow of oxygen is obtained by :

$$\dot{m}_{O_2} = 2 \cdot \frac{MM_{O_2}}{MM_{H_2}} \cdot \dot{m}_{H_2} = 32 \cdot \dot{m}_{H_2} \quad (2.6)$$

with,

$$\begin{aligned} MM_{O_2} &= 32 \quad [\text{g/mol}] \\ MM_{H_2} &= 2 \quad [\text{g/mol}] \end{aligned}$$

In general, pure oxygen is replaced by air at cathode inlet. Assuming the composition of air (Section 2.1), the mass flow of air at cathode inlet is then obtained by:

$$\dot{m}_{cath,i} = \dot{m}_{O_2} + \dot{m}_{N_2} = \dot{n}_{O_2} \cdot MM_{O_2} + \dot{n}_{N_2} \cdot MM_{N_2} \quad (2.7)$$

$$\dot{m}_{cath,i} = \frac{1}{2}\alpha U_f \cdot MM_{O_2} + \frac{1}{2}\frac{0.79}{0.21}\alpha U_f \cdot MM_{N_2} \tag{2.8}$$

$$\dot{m}_{cath,i} = \left(\frac{1}{2}U_f \cdot MM_{O_2} + \frac{1}{2}\frac{0.79}{0.21}U_f \cdot MM_{N_2}\right) \cdot \dot{n}_{H_2} \tag{2.9}$$

$$\dot{m}_{cath,i} = \left(\frac{1}{2}U_f \cdot MM_{O_2} + \frac{1}{2}\frac{0.79}{0.21}U_f \cdot MM_{N_2}\right) \cdot \frac{\dot{m}_{H_2}}{MM_{H_2}} \tag{2.10}$$

If an air excess (e) is present, Eq. 2.10 becomes :

$$\dot{m}_{cath,i} = \lambda \cdot \left(\frac{1}{2}U_f \cdot MM_{O_2} + \frac{1}{2}\frac{0.79}{0.21}U_f \cdot MM_{N_2}\right) \cdot \frac{\dot{m}_{H_2}}{MM_{H_2}} \tag{2.11}$$

with,

$$\lambda = 1 + e$$

2.2.2 Partial pressures

In this model, we assume that the partial pressures are taken at the SOFC outlet as commonly used in the literature [68]. However, other assumptions could be made such as partial pressures taken at the inlet or a mixed of inlet and outlet. The definition of the partial pressure is given by:

$$p_i = x_i \cdot p_t = \frac{\dot{n}_i}{\dot{n}_t} \cdot p_t \tag{2.12}$$

where,

p_i	:	Partial pressure of substance i	[kPa]
p_t	:	Total pressure of mixture	[kPa]
x_i	:	Molar fraction of substance i	[-]
$\dot{n}_i$	:	Flow of moles of substance i	[mol/s]
$\dot{n}_t$	:	Total flow of moles	[mol/s]

2.3 Energy balance of the SOFC

Let us define a control volume as represented in Fig. 2.1. Power inputs and outputs of the SOFC are related through the following balance equation:

$$\dot{H}_{cath,i} + \dot{H}_{an,i} = \dot{H}_{cath,o} + \dot{H}_{an,o} + P_{el} + Q_{FC} \tag{2.13}$$

where,

$\dot{H}_{cath,i}$	:	Enthalpy flow at cathode inlet	[W]
$\dot{H}_{an,i}$	:	Enthalpy flow at anode inlet	[W]
$\dot{H}_{cath,o}$	:	Enthalpy flow at cathode outlet	[W]
$\dot{H}_{an,o}$	:	Enthalpy flow at anode outlet	[W]
P_{el}	:	Electric power produced	[W]
Q_{FC}	:	Heat released	[W]

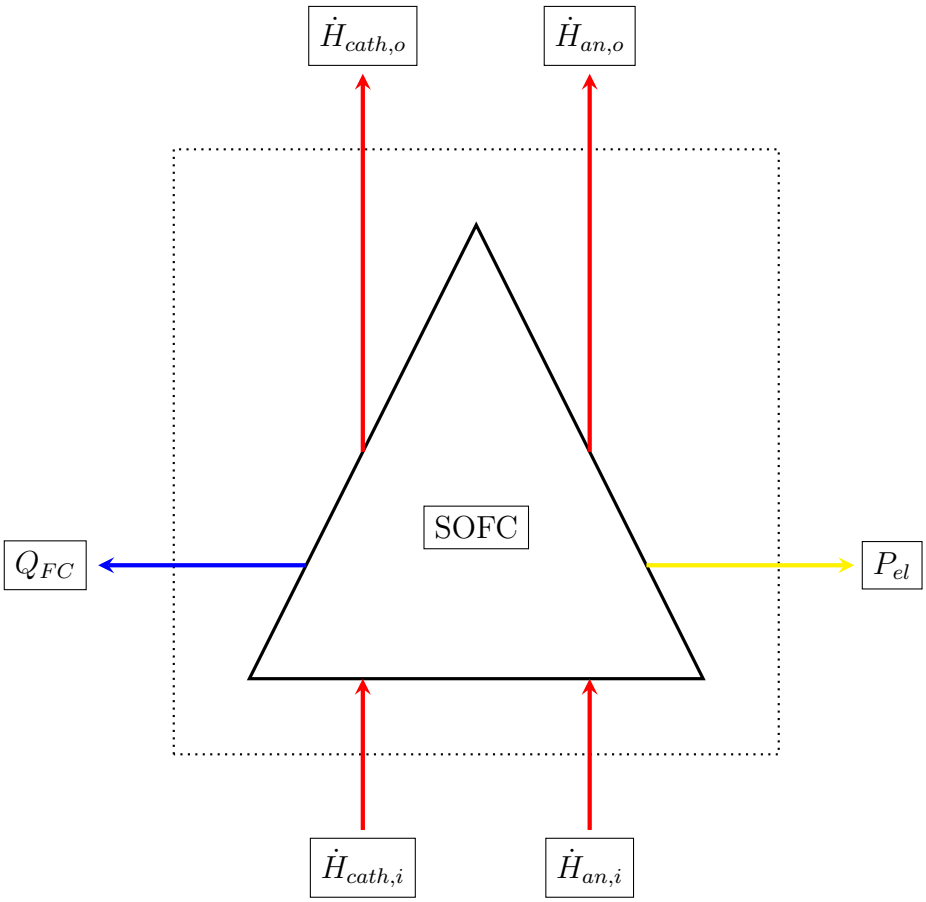

Figure 2.1: SOFC control volume.

2.3.1 Anode

The outlet gas of the reformer enters the anode inlet. The total enthalpy flow depends on the mass flow, the composition, the temperature and the pressure inside the SOFC.

As the hydrogen is the only one to react inside the SOFC, the total enthalpy flow at the inlet depends on the specific enthalpy of the total mixture and the net heating value (LHV) of hydrogen.

$$\dot{H}_{an,i} = \dot{m}_{an,i} \cdot h_{an,i} + \dot{m}_{H_2,i} \cdot LHV_{H_2} \tag{2.14}$$

At the outlet, the composition has changed as water is produced during the chemical reaction:

$$\dot{H}_{an,o} = \dot{m}_{an,o} \cdot h_{an,o} + \dot{m}_{H_2,o} \cdot LHV_{H_2} \tag{2.15}$$

The outlet flow of hydrogen is obtained using the fuel utilization (U_f):

$$\dot{m}_{H_2,o} = (1 - U_f) \cdot \dot{m}_{H_2,i} \tag{2.16}$$

2.3.2 Cathode

At the cathode, air is injected at the inlet and oxygen fraction is reduced at the outlet. The mass flow of oxygen ions crossing the electrolyte is related to the mass

flow of hydrogen present at the anode as seen in Section 2.2.1. The main assumption is that only the reacting oxygen is transported to the anode side.

The total enthalpy flow of the air at inlet is given by the product between the mass flow of air and the specific enthalpy of air:

$$\dot{H}_{cath,i} = \dot{m}_{cath,i} \cdot h_{cath,i} \tag{2.17}$$

Similarly, the outlet enthalpy flow of air at cathode is given by:

$$\dot{H}_{cath,o} = \dot{m}_{cath,o} \cdot h_{cath,o} \tag{2.18}$$

The outlet mass flow of air at cathode is the inlet mass flow reduced by the mass flow of oxygen transferred to the anode side:

$$\dot{m}_{cath,o} = \dot{m}_{cath,i} - \dot{m}_{O_2} \tag{2.19}$$

2.4 Electric power and internal heat

The electric power (P_{el}) and the generated heat (Q_{FC}) are related to the enthalpy flows at inlets and outlets by Eq. 2.13. Both electric power and generated heat are unknown. An expression of the generated heat is developed in this section assuming a given electric power.

The electric power is the product of the voltage and the current:

$$P_{el} = V_o \cdot I \tag{2.20}$$

In a fuel cell, the output voltage corresponds to the Nernst voltage reduced by irreversible losses occurring inside the stack.

2.4.1 Current

The current is proportional to the flow of electrons coming from the oxidation of hydrogen. The flow of electrons depends on the rate of the oxidation reaction and consequently on the flow of hydrogen:

$$I = \dot{n}_{el} \cdot e_c \cdot N_A = \dot{n}_{el} \cdot F = 2 \cdot \dot{n}_{H_2} \cdot F \tag{2.21}$$

with,

$$\begin{array}{lcll} e_c & = & 1.6021733 \cdot 10^{-19} & [\mathrm{C}] \\ N_A & = & 6.0221409 \cdot 10^{23} & [1/\mathrm{mol}] \\ F & = & 96485.3329 & [\mathrm{C/mol}] \end{array}$$

2.4.2 Voltage

Assuming an ideal gas, the Nernst potential is expressed by:

$$V_N = -\frac{\Delta G_0(T)}{nb_{el} \cdot F} - \frac{R_m \cdot T}{nb_{el} \cdot F} \cdot ln\,(K) \tag{2.22}$$

with,

ΔG_0	:	Change in standard free energy of Gibbs	[J]
nb_{el}	:	Number of electrons produced during oxidation	[-]
K	:	Equilibrium constant	[-]

The equilibrium constant depends on the partial pressures of each reactant and product of Eq. 2.5:

$$K = \frac{p_{CH_4}^{\beta} \cdot p_{CO}^{\gamma} \cdot p_{CO_2}^{\delta} \cdot p_{N_2}^{(0.5\frac{0.79}{0.21}\alpha U_f)} \cdot p_{H_2O}^{(\theta+\alpha U_f)}}{p_{H_2}^{\alpha U_f} \cdot p_{CH_4}^{\beta} \cdot p_{CO}^{\gamma} \cdot p_{CO_2}^{\delta} \cdot p_{O_2}^{0.5\alpha U_f} \cdot p_{N_2}^{(0.5\frac{0.79}{0.21}\alpha U_f)} \cdot p_{H_2O}^{\theta}} \tag{2.23}$$

After simplifications, the following expression is obtained:

$$K = \frac{p_{H_2O}^{\alpha U_f}}{p_{H_2}^{\alpha U_f} \cdot p_{O_2}^{0.5\alpha U_f}} \tag{2.24}$$

Considering standard free enthalpy variation, the only impacting substance is water since pure substances as oxygen and hydrogen have a standard energy of Gibbs of 0. The change in enthalpy is evaluated at standard pressure (1 atm) and standard temperature (T = 298.15 K). The following value is based on [61]:

$$\Delta G_0(T) = -228.582 \text{ kJ/mol} \tag{2.25}$$

2.4.3 Irreversible losses

The output voltage of the fuel cell does not exactly correspond to the Nernst potential. Indeed, irreversible losses decrease the reversible voltage depending on the current density present in the fuel cell. Three types of losses can be identified : the actuation losses, the ohmic losses and the concentration losses.

Actuation losses

The actuation losses appear at small current densities when the reactions are initiated because an activation energy barrier is present and must be overcome. When the circuit is open and current is not flowing, the rates of both reactions are equal. In that case, the exchange current densities at anode and cathode are equal. The extra voltage (or energy) called "activation voltage" shifts the reaction in one way or another to flow electrons in an external circuit. That specific voltage can be modelled using the Butler-Volmer equation (Eq. 2.26) [30]:

$$V_{act} = V_{act,a} + V_{act,c} = \frac{R_m \cdot T}{F} \cdot \left[\sinh^{-1}\left(\frac{i}{2 \cdot i_{0,a}}\right) + \sinh^{-1}\left(\frac{i}{2 \cdot i_{0,c}}\right) \right] \tag{2.26}$$

with,

$i_{0,a}$	:	Exchange current density at anode	[A/cm^2]
$i_{0,c}$	:	Exchange current density at cathode	[A/cm^2]

The exchange current densities are calculated using the Arrhenius law [69]. An experimental validation can be found in [70]:

$$\begin{aligned} i_{0,a} &= \gamma_a \frac{p_{H_2,o} \cdot p_{H_2O,o}}{p_t^2} \cdot \exp\left(-\frac{E_{act,a}}{R_m \cdot T}\right) \\ i_{0,c} &= \gamma_c \left(\frac{p_{O_2,o}}{p_t}\right)^{0.25} \cdot \exp\left(-\frac{E_{act,c}}{R_m \cdot T}\right) \end{aligned} \tag{2.27}$$

with,

$\gamma_{a,c}$	:	Pre-exponential factor at anode or cathode	[A/cm^2]
$E_{act_{a,c}}$	:	Activation energies at anode and cathode	[J/mol]

Ohmic losses

Ohmic losses appear due to the internal ionic and electronic resistances in electrolyte, anode, cathode and interconnections. They depend on the thickness of each item, on the resistivity of the materials and on temperature. The overvoltage is given by [69]:

$$V_{ohm} = i \cdot \sum \rho_j \cdot \delta_j = i \cdot \sum O_j \cdot \delta_j \cdot \exp\left(\frac{B_j}{T}\right) \tag{2.28}$$

with,

ρ_j	:	Resistivity of the material	[Ωcm]
O_j	:	Ohmic loss coefficient	[Ωcm]
B_j	:	Ohmic loss coefficient	[K]
δ_j	:	Thickness	[cm]

Notice that the contact resistances have been so far neglected which is common in the literature as explained in Colpan et al. [24].

Concentration losses

As the current density increases inside the fuel cell, the flows of ions and electrons are more important. Concentration gradients can then appear and induce a loss in concentration of reactants at the reaction sites. At high current densities, this concentration can drop to zero and the limiting current density is achieved. The concentration overvoltage in Eq. 2.29 is calculated using an empirical formulation validated through experimentation. It corresponds to the sum of the overvoltages at the anode and the cathode [69]:

$$V_{conc} = V_{conc,a} + V_{conc,c} \tag{2.29}$$

$$V_{conc,a} = \frac{R_m \cdot T}{nb_{el} \cdot F} \left[-\ln\left(1 - \frac{i}{i_{L,a}}\right) + \ln\left(1 + \frac{p_{H_2,o} \cdot i}{p_{H_2O,o} \cdot i_{L,a}}\right)\right] \tag{2.30}$$

$$V_{conc,c} = -\frac{R_m \cdot T}{2 \cdot nb_{el} \cdot F} \cdot \ln\left(1 - \frac{i}{i_{L,c}}\right) \tag{2.31}$$

with,

$i_{L,a}$	:	Limiting current density at anode	[A/cm^2]
$i_{L,c}$	:	Limiting current density at cathode	[A/cm^2]

The limiting current densities also derive from empirical formulations:

$$\begin{aligned} i_{L,a} &= \frac{2 \cdot F \cdot p_{H_2,o} \cdot D_{eff,a}}{R_m \cdot T \cdot \delta_a} \\ i_{L,c} &= \frac{4 \cdot F \cdot p_{O_2,o} \cdot D_{eff,c}}{\left(\frac{p_t - p_{O_2,o}}{p_t}\right) \cdot R_m \cdot T \cdot \delta_c} \end{aligned} \tag{2.32}$$

with,

$D_{eff_{a,c}}$: Effective diffusivity of the anode and the cathode [cm²/s]

Irreversible losses estimate

Irreversible losses (Eq. 2.26, 2.28, 2.29) are estimated as a function of the current density with parameters values listed in Table 2.1 ([65] [69] [71] [72]) . Much work is being carried out in the literature to measure and predict more accurately the values of these parameters such as the effective diffusivity [36].

Activation			
Pre-exponential factor (Anode)	:	70000	[A/cm²]
Pre-exponential factor (Cathode)	:	70000	[A/cm²]
Activation energy (Anode)	:	100000	[J/mol]
Activation energy (Cathode)	:	110000	[J/mol]
Ohmic			
Ohmic loss coefficient (Anode)	:	0.00105	[Ωcm]
Ohmic loss coefficient (Cathode)	:	0.00238	[Ωcm]
Ohmic loss coefficient (Electrolyte)	:	$\frac{2.994}{T}$	[Ωcm]
Thickness (Anode)	:	0.05	[cm]
Thickness (Cathode)	:	0.005	[cm]
Thickness (Electrolyte)	:	0.004	[cm]
Concentration			
Effective diffusivity (Anode)	:	0.07	[cm²/s]
Effective diffusivity (Cathode)	:	0.054	[cm²/s]

Table 2.1: Irreversible losses parameters.

Fig. 2.2 shows the evolution of the irreversible losses as a function of the current density inside the fuel cell. As far as the activation losses are concerned, they grow nearly linearly and are the most predominant losses until high current densities. Ohmic losses are linear and are the least important. The concentration losses become non negligible at high current densities due to the important movements of ions and electrons.

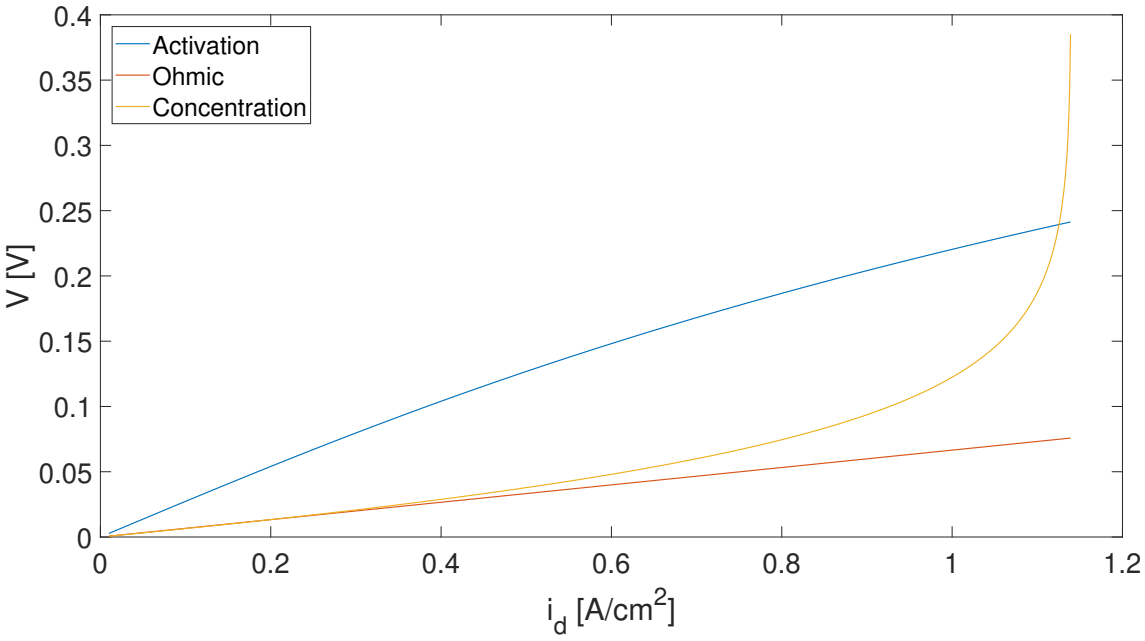

Figure 2.2: Irreversible losses [V] as a function of the current density [A/cm²] ($T = 1173.15$ [K], $p_t = 200$ [kPa]).

2.4.4 Output voltage and power

The output voltage is calculated using the Nernst potential and the irreversible losses. As the losses increase with the current density, the output voltage will thus decrease.

$$V_o = V_N - V_{act} - V_{ohm} - V_{conc} \tag{2.33}$$

Fig 2.3 shows the evolution of the output voltage as a function of the current density. As expected, it decreases almost linearly because of the predominant actuation and ohmic losses at low and moderate current densities. At high current densities, the concentration losses are more important and the voltage drops.

From Eq. 2.20, the electrical power is computed by multiplying the output voltage and the current. Similarly, the electric power density is obtained by multiplying the voltage with the current density:

$$p_{el} = V_o \cdot i \tag{2.34}$$

Fig 2.4 shows the evolution of the power density with respect to the current density. The power density reaches a maximum. As shown in Section 2.5, power density and efficiency have opposite behaviors. Power density and efficiency allows for a compact system and a reduction of fuel consumption respectively. The choice thus results from a trade-off and designer objective.

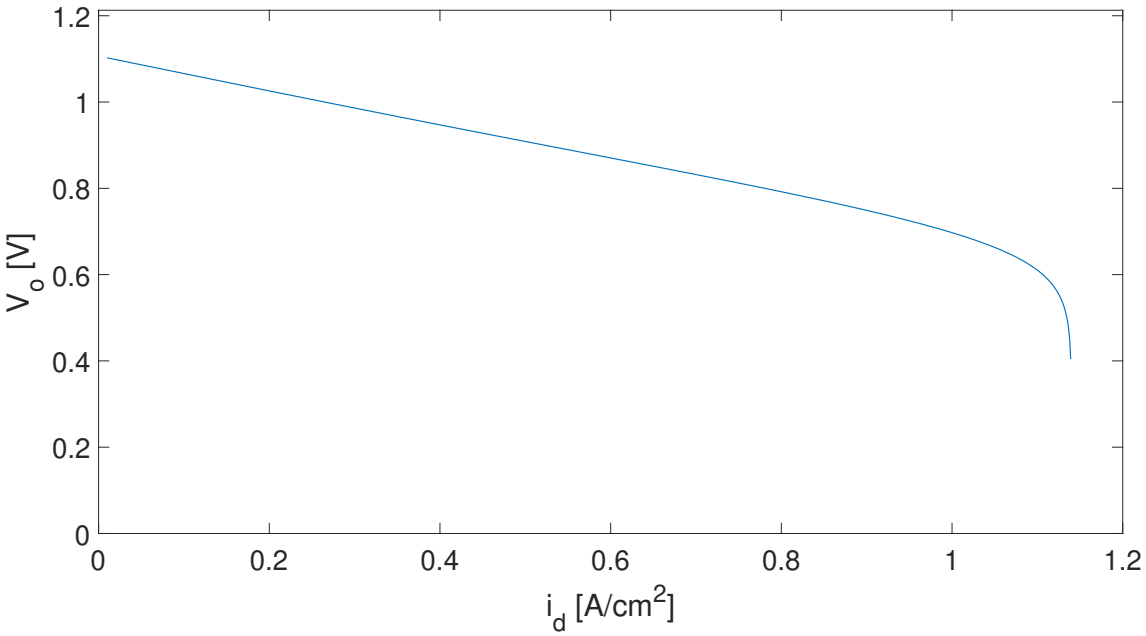

Figure 2.3: Output voltage [V] as function of the current density [A/cm²] (T = 1173.15 [K], p_t = 200 [kPa], U_f = 0.7 [-], λ = 1.5 [-], $\dot{m}_{CH_4}$ = 3.2E-4 [kg/s], $\dot{m}_{H_2O}$ = 4.95E-4 [kg/s]).

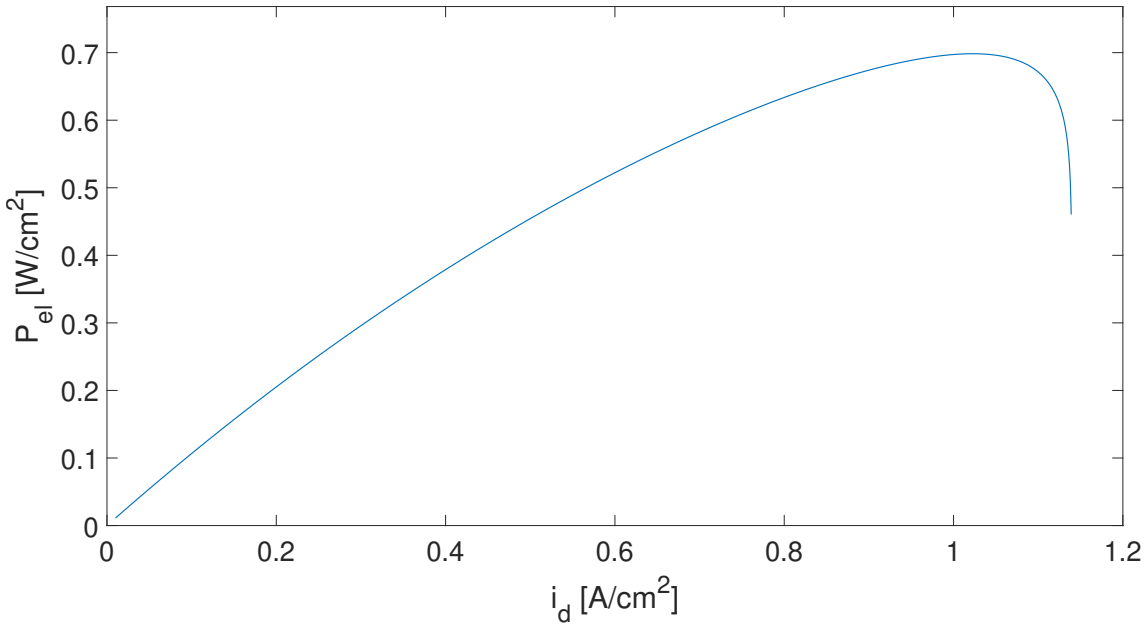

Figure 2.4: Electric power density [W/cm²] as a function of the current density [A/cm²] (T = 1173.15 [K], p_t = 200 [kPa], U_f = 0.7 [-], λ = 1.5 [-], $\dot{m}_{CH_4}$ = 3.2E-4 [kg/s], $\dot{m}_{H_2O}$ = 4.95E-4 [kg/s]).

The electric power can also be represented as a function of the current density, as shown in Fig. 2.5, and is naturally following the curve of the output voltage.

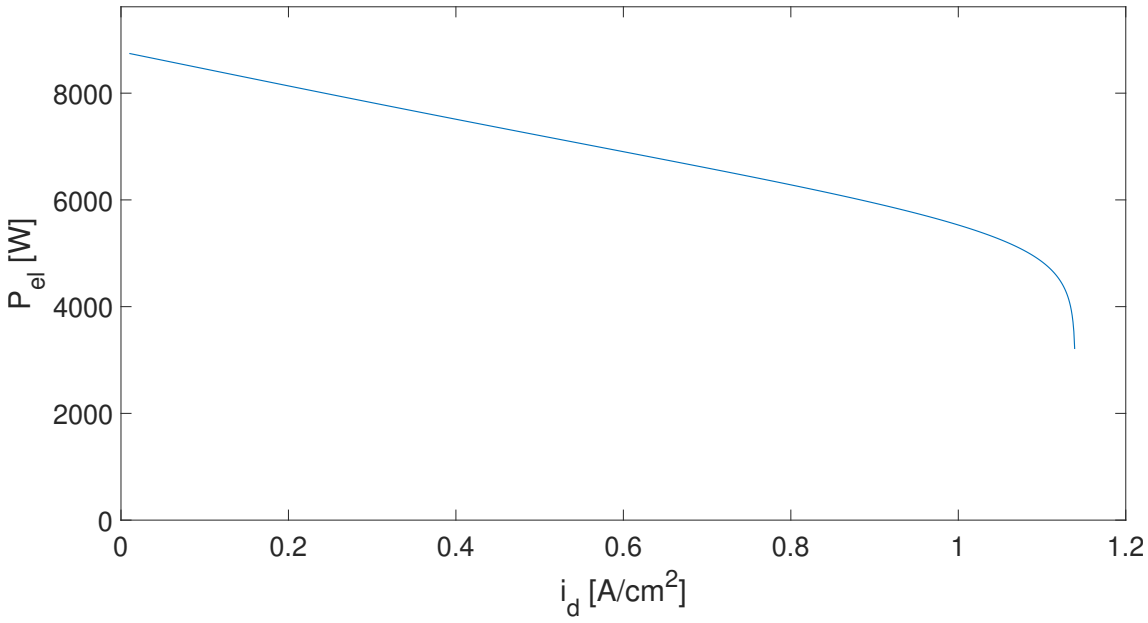

Figure 2.5: Electric power [W] as a function of the current density [A/cm²] (T = 1173.15 [K], p_t = 200 [kPa], U_f = 0.7 [-], λ = 1.5 [-], $\dot{m}_{CH_4}$ = 3.2E-4 [kg/s], $\dot{m}_{H_2O}$ = 4.95E-4 [kg/s]).

2.4.5 Internal heat

The chemical reaction happening at the anode side is exothermic, with released heat denoted Q_{FC}. The latter is related to the electric power using Eq. 2.13:

$$Q_{FC} = \dot{H}_{cath,i} + \dot{H}_{an,i} - \dot{H}_{cath,o} - \dot{H}_{an,o} - P_{el} \tag{2.35}$$

Fig. 2.6 shows the evolution of the generated heat with respect to the current density. As seen in Eq. 2.35, the heat generated is a constant minus the total electric power, which obviously gives an opposite shape than in Fig. 2.5.

2.5 Efficiency

The electrical efficiency of the SOFC is defined as the ratio between the produced electric power and the energy contained in the fuel entering the SOFC stack. In this case, we consider the efficiency with the reforming fuel (methane). The low heating value is taking at 25° C and at 1 atm.

The electric power is obtained by the multiplication of the electric power density and the area of reaction (A). This area is obtained by dividing the total current of Eq. 2.21 by the current density.

$$P_{el} = p_{el} \cdot A \tag{2.36}$$

with,

$$A = \frac{I}{i} = \frac{2 \cdot \dot{n}_{H_2} \cdot F}{i}$$

The evolution of the area is described in Fig. 2.7 using the number of cells considering the single cell area (A_{1cell}) to be 100 cm² as an example:

$$A = N_{cells} \cdot A_{1cell}$$

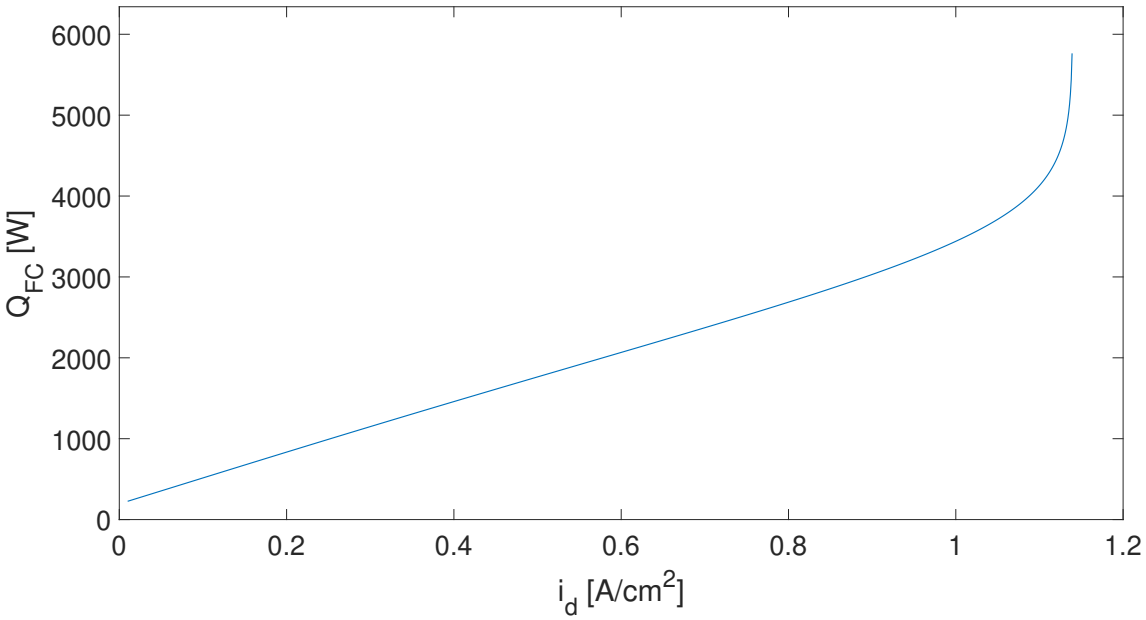

Figure 2.6: Generated heat [W] as a function of the current density [A/cm²] (T = 1173.15 [K], p_t = 200 [kPa], U_f = 0.7 [-], λ = 1.5 [-], $\dot{m}_{CH_4}$ = 3.2E-4 [kg/s], $\dot{m}_{H_2O}$ = 4.95E-4 [kg/s]).

The number of cells (Fig. 2.7) exponentially decreases with respect to current density. Notice that the most important constant that defines the electric power output is the mass flow of hydrogen entering the anode side or, in an analogous way, the mass flow of methane entering the reformer.

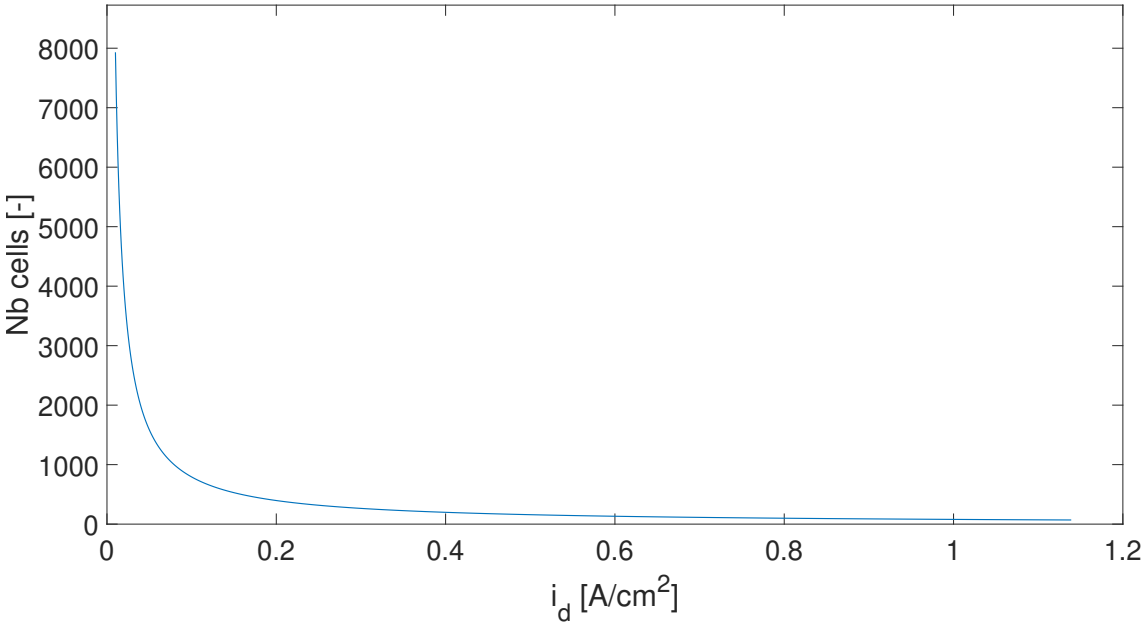

Figure 2.7: Number of cells [-] as a function of the current density [A/cm²] (T = 1173.15 [K], p_t = 200 [kPa], U_f = 0.7 [-], λ = 1.5 [-], $\dot{m}_{CH_4}$ = 3.2E-4 [kg/s], $\dot{m}_{H_2O}$ = 4.95E-4 [kg/s]).

The expression for the efficiency is given by:

$$\eta_{SOFC} = \frac{P_{el}}{\dot{m}_{CH_4} \cdot LHV_{CH_4}} \tag{2.37}$$

with,

$\dot{m}_{CH_4,i}$	:	Mass flow of methane at the inlet	[kg/s]
LHV_{CH_4}	:	Net heating value of methane	[J/kg]

Fig. 2.8 shows the evolution of the efficiency of the SOFC as a function of the current density. It follows the same behavior as the output voltage because of the linear relationship between the power density and the output voltage as seen in Eq. 2.34.

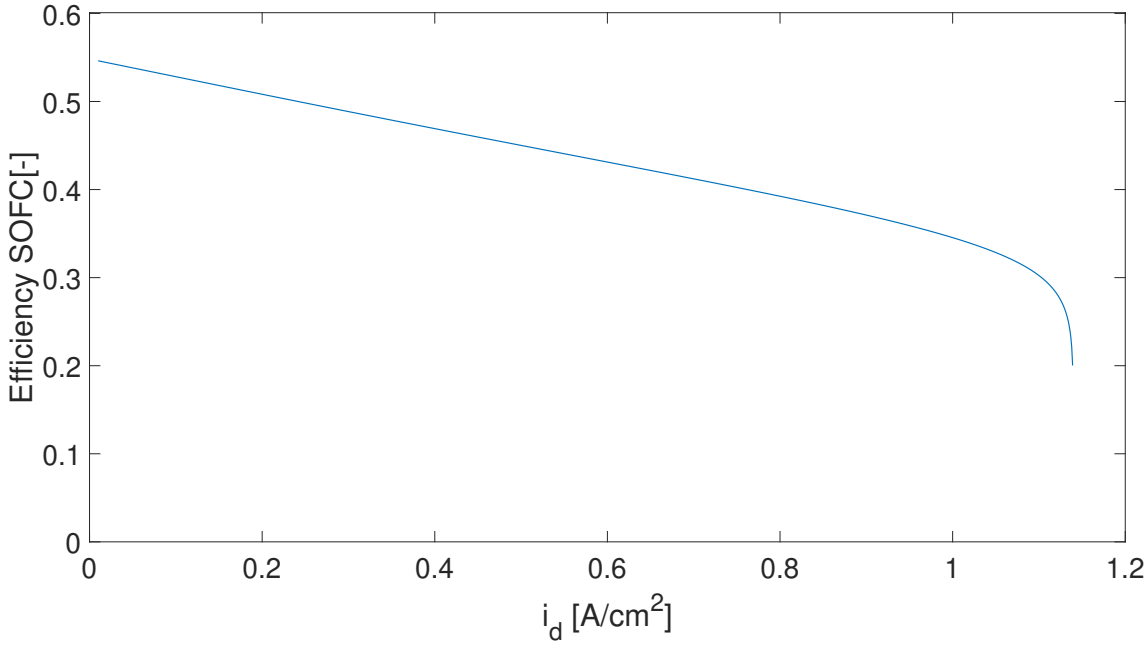

Figure 2.8: Efficiency [-] as a function of the current density [A/cm²] ($T = 1173.15$ [K], $p_t = 200$ [kPa], $U_f = 0.7$ [-], $\lambda = 1.5$ [-], $\dot{m}_{CH_4} = 3.2\text{E-}4$ [kg/s], $\dot{m}_{H_2O} = 4.95\text{E-}4$ [kg/s]).

2.6 Influence of operating conditions

In this section, stack performance is analyzed with respect to varying operating parameters such as temperature, pressure and air excess. Stack performance is evaluated through output voltage, power density and efficiency as a function of the current density. The behavior of the number of cells and generated heat is given in Annex B. The irreversible losses are calculated based on parameter values listed in Table 2.1.

The reformer performance is taken into account into this analysis. Its modelling is described in the Chapter 3.

2.6.1 Temperature

Fig. 2.9 shows the output voltage as a function of the current density for different temperatures. The Nernst voltage could be slightly affected by increasing temperature while irreversible losses will decrease especially at high current densities. From Eq. 2.32, the limiting current densities mostly decrease with increasing temperature. However, at sufficient low temperatures, the reformer performance is altered which impacts the partial pressure of reactants at outlet and yield to lower limiting current densities.

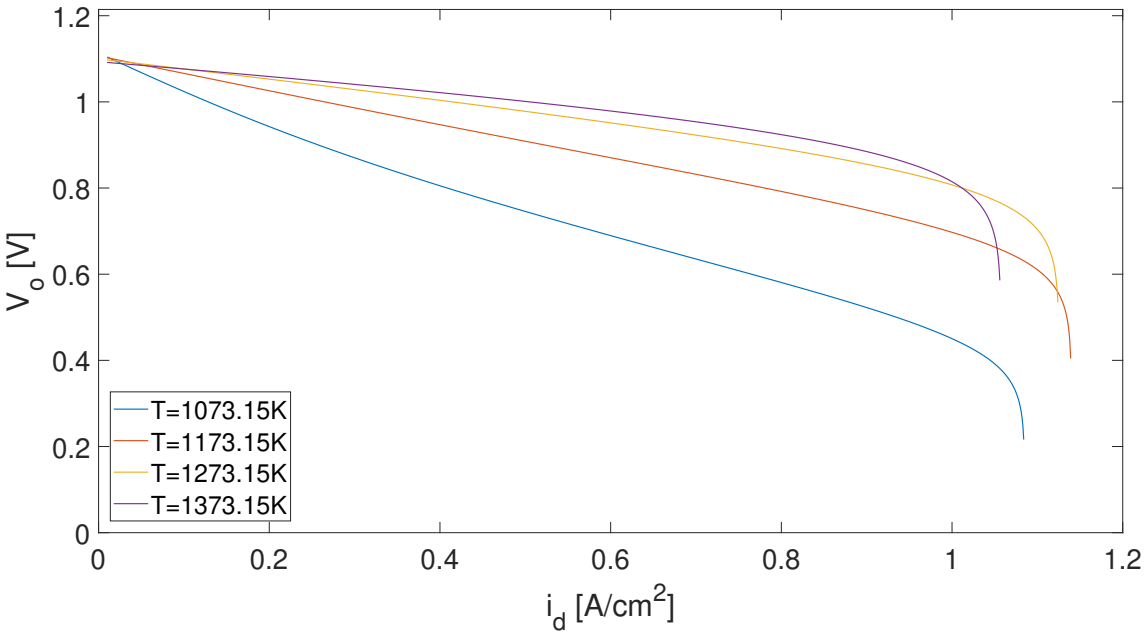

Figure 2.9: Output voltage [V] as a function of the current density [A/cm²] for different temperatures (p_t = 200 [kPa], U_f = 0.7 [-], λ = 1.5 [-], $\dot{m}_{CH_4}$ = 3.2E-4 [kg/s], $\dot{m}_{H_2O}$ = 4.95E-4 [kg/s]).

The electric power density (2.10) exhibits an increasing maximum with increasing temperature but with a lower limit in current density.

The efficiency is for most of the current densities higher at high temperature. Nevertheless, it seems that at low current densities, the efficiency increases for lower temperatures. It is probably due to the fact that the number of cells in Fig B.1 for the lowest temperatures is far more important than at other temperatures which results in higher electric power and efficiency. The operation of the SOFC in these current densities is however not usual.

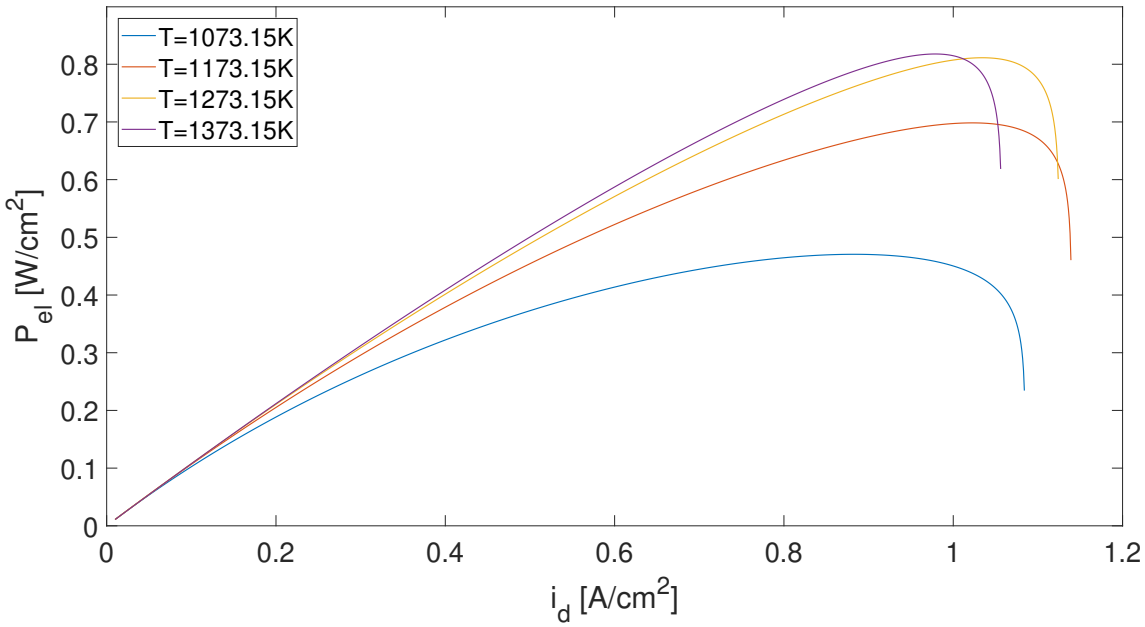

Figure 2.10: Electric power density [W] as a function of the current density [A/cm²] for different temperatures (p_t = 200 [kPa], U_f = 0.7 [-], λ = 1.5 [-], $\dot{m}_{CH_4}$ = 3.2E-4 [kg/s], $\dot{m}_{H_2O}$ = 4.95E-4 [kg/s]).

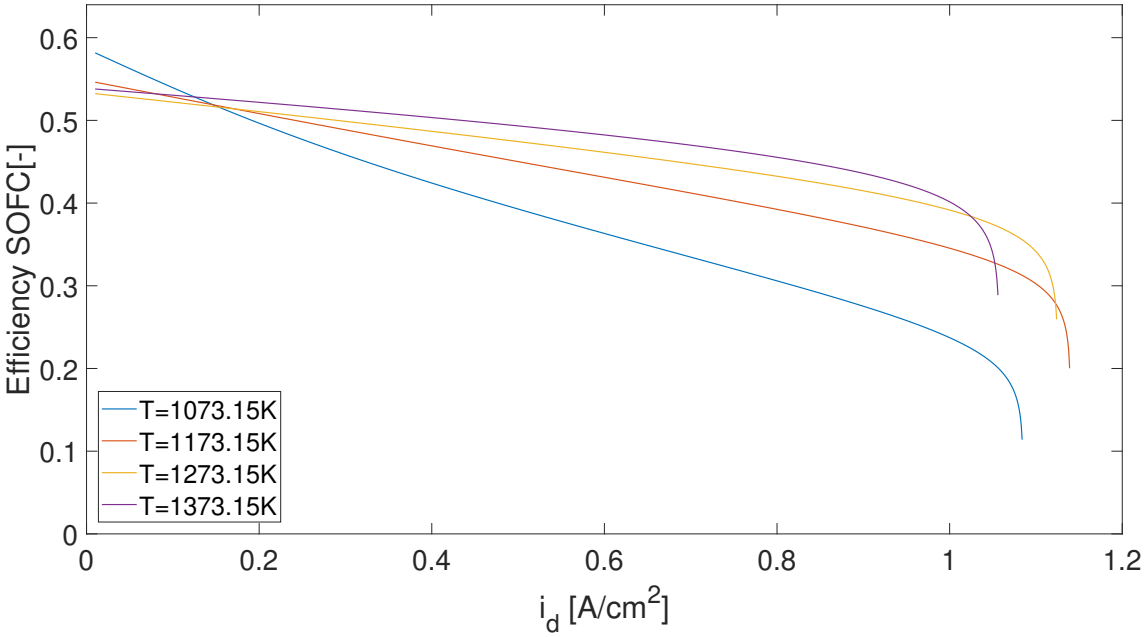

Figure 2.11: Efficiency of the SOFC [-] as a function of the current density [A/cm²] for different temperatures (p_t = 200 [kPa], U_f = 0.7 [-], λ = 1.5 [-], $\dot{m}_{CH_4}$ = 3.2E-4 [kg/s], $\dot{m}_{H_2O}$ = 4.95E-4 [kg/s]).

2.6.2 Pressure

The first thing to notice on Fig. 2.12, 2.13 and 2.14 is that increasing the pressure increases the limiting current density, which offers a great advantage from the compactness point of view.

Output voltage also increases with increasing pressure most notably at high current densities (Fig 2.12).

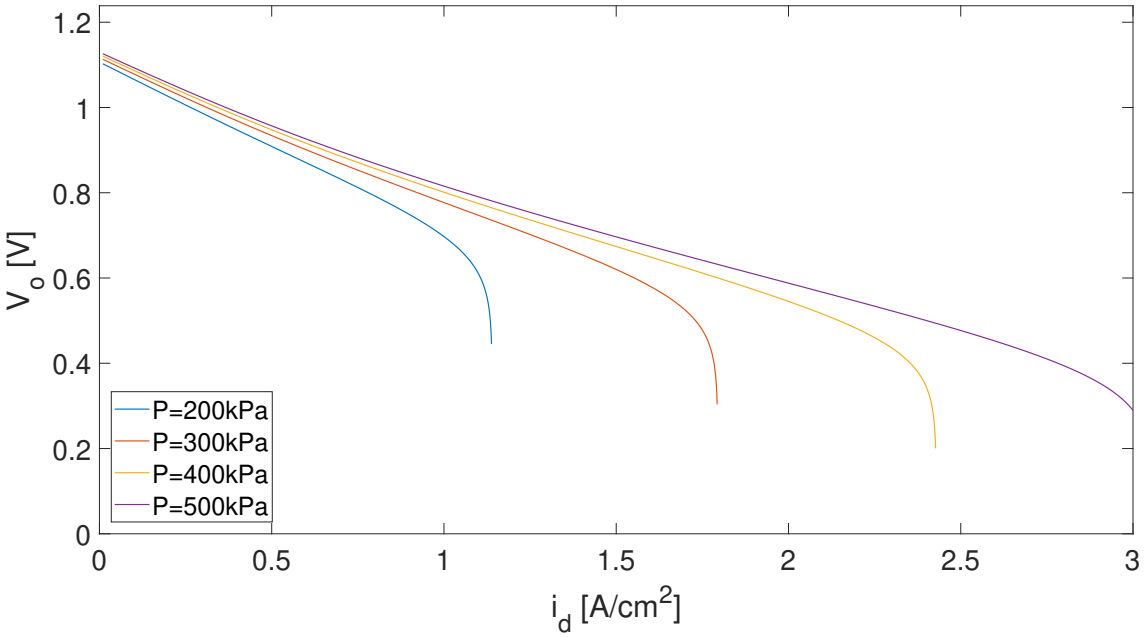

Figure 2.12: Output voltage [V] as a function of the current density [A/cm²] for different pressures (T = 1173.15 [K], U_f = 0.7 [-], λ = 1.5 [-], $\dot{m}_{CH_4}$ = 3.2E-4 [kg/s], $\dot{m}_{H_2O}$ = 4.95E-4 [kg/s]).

The increase of pressure has a greater impact on maximum power density which nearly doubles between 200 kPa and 500 kPa (Fig. 2.13) and therefore increases the compactness of the SOFC.

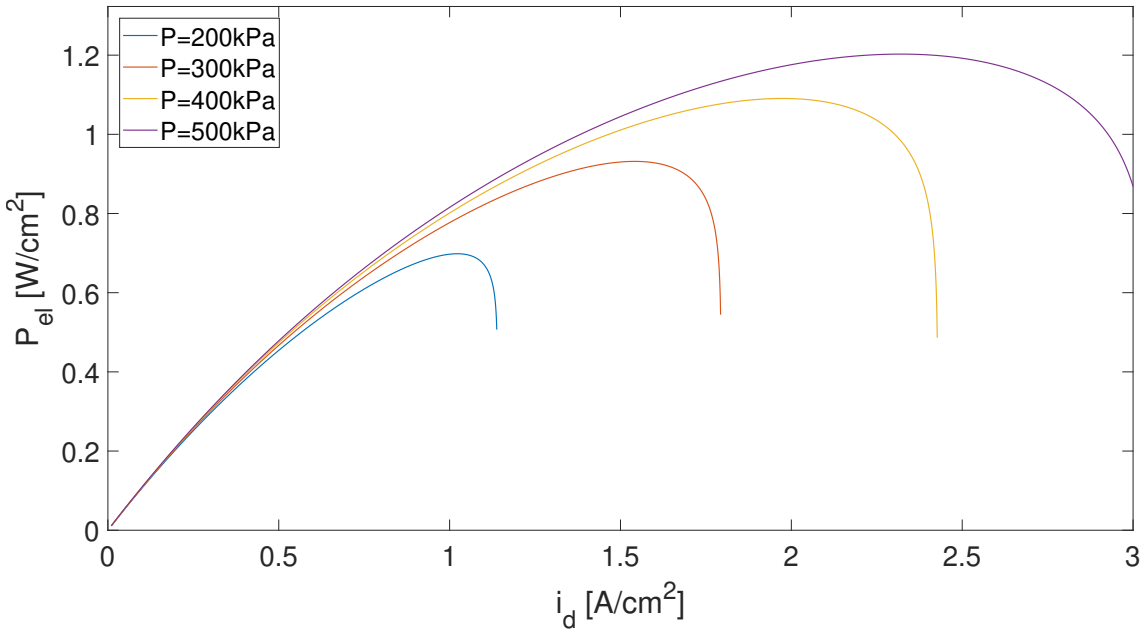

Figure 2.13: Electric power density [W/cm²] as a function of the current density [A/cm²] for different pressures (T = 1173.15 [K], U_f = 0.7 [-], λ = 1.5 [-], $\dot{m}_{CH_4}$ = 3.2E-4 [kg/s], $\dot{m}_{H_2O}$ = 4.95E-4 [kg/s]).

Efficiency similarly behaves as the output voltage and therefore the same conclusions can be drawn.

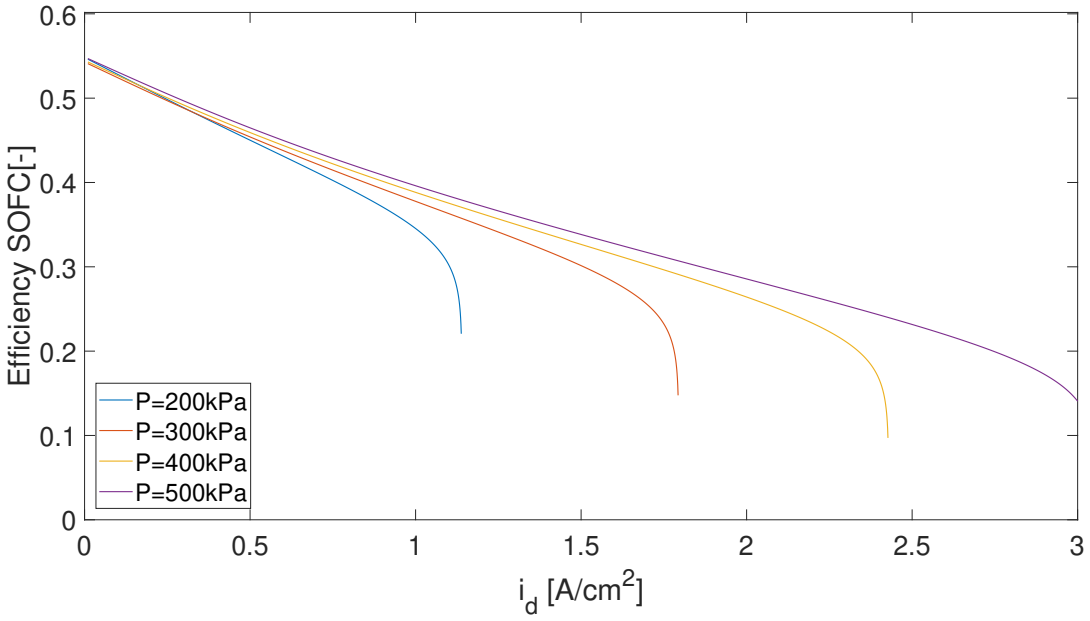

Figure 2.14: Efficiency of the SOFC [-] as a function of the current density [A/cm²] for different pressures (T = 1173.15 [K], U_f = 0.7 [-], λ = 1.5 [-], $\dot{m}_{CH_4}$ = 3.2E-4 [kg/s], $\dot{m}_{H_2O}$ = 4.95E-4 [kg/s]).

2.6.3 Air excess

Fig. 2.15, 2.16 and 2.17 show the evolution of output voltage, electric power density and efficiency with respect to air excess. For all, the air excess does not appear to be a critical parameter.

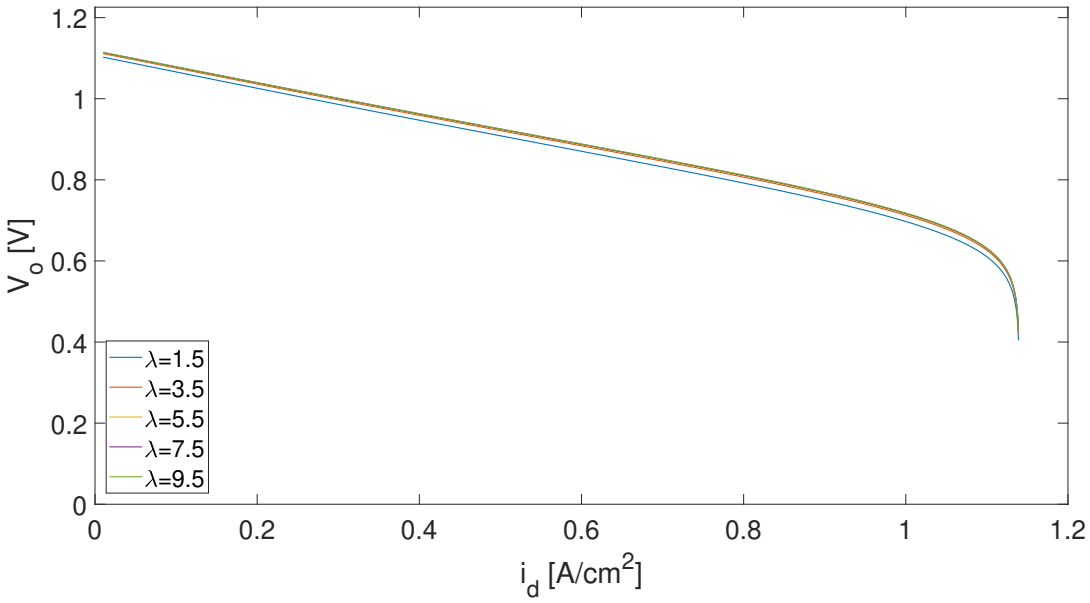

Figure 2.15: Output voltage [V] as a function of the current density [A/cm²] for different air excesses (T = 1173.15 [K], p_t = 200 [kPa], U_f = 0.7 [-], $\dot{m}_{CH_4}$ = 3.2E-4 [kg/s], $\dot{m}_{H_2O}$ = 4.95E-4 [kg/s]).

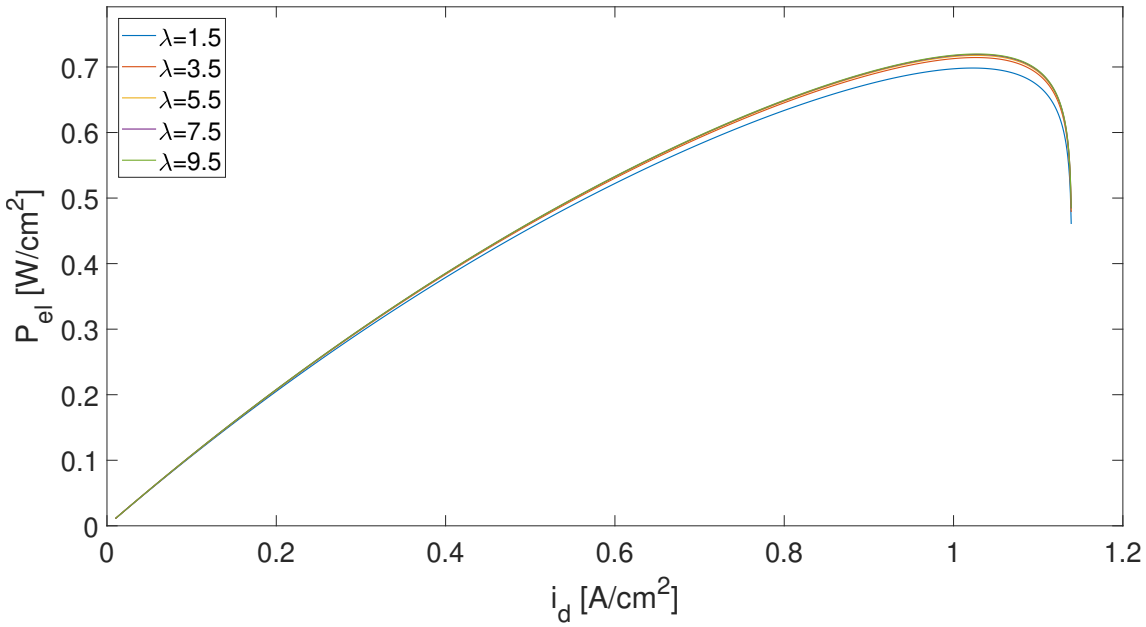

Figure 2.16: Electric power density [W/cm²] as a function of the current density [A/cm²] for different air excesses ($T = 1173.15$ [K], $p_t = 200$ [kPa], $U_f = 0.7$ [-], $\dot{m}_{CH_4} = 3.2\text{E-}4$ [kg/s], $\dot{m}_{H_2O} = 4.95\text{E-}4$ [kg/s]).

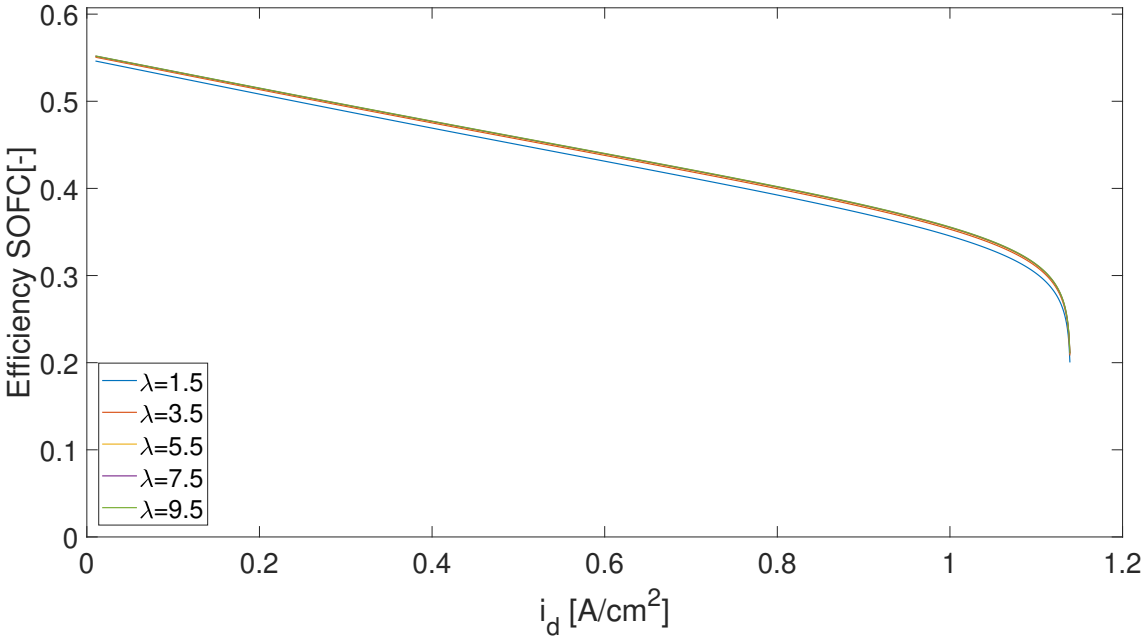

Figure 2.17: Efficiency of the SOFC [-] as a function of the current density [A/cm²] for different air excesses ($T = 1173.15$ [K], $p_t = 200$ [kPa], $U_f = 0.7$ [-], $\dot{m}_{CH_4} = 3.2\text{E-}4$ [kg/s], $\dot{m}_{H_2O} = 4.95\text{E-}4$ [kg/s]).

Chapter 3

Fuel processing

This chapter is dedicated to the understanding and modelling of specific fuel processing inside the stack such as the anode gas recirculation while considering other improvements in reforming and water management.

3.1 Reforming

In this work, we assume that the reforming is indirect internal with a steam reforming reaction since it is proving to be the most efficient and relatively easy to implement in a stack (see Section 3.1).

The implementation of the reforming model follows the 1D model developed by Hester [37] which solves equations commonly used in the literature ([60] [25] [26] [52] [15] [73]).

The objective is to simulate the steam reforming of methane using two reactions: the steam reforming and the water gas shift. The model is based on mass and energy balances as well as kinetics of the combined reactions computed along the reactor length.

- Steam reforming (SR):

$$CH_4 + H_2O \rightleftharpoons CO + 3H_2 \qquad \Delta H_{298} = 206 \text{ kJ/mol} \qquad (3.1)$$

- Water gas shift (WGS) equilibrium:

$$CO + H_2O \rightleftharpoons CO_2 + H_2 \qquad \Delta H_{298} = -41 \text{ kJ/mol} \qquad (3.2)$$

- Global reforming reaction (GR):

$$CH_4 + 2H_2O \rightleftharpoons CO_2 + 4H_2 \qquad \Delta H_{298} = 165 \text{ kJ/mol} \qquad (3.3)$$

3.1.1 Reformer mathematical model

- Molar composition :

  The kinetics of the equations are based on the rates of formation of each substance which depend on the rates of each reaction described above.

$$\begin{array}{rcl} R_{CH_4} & = & -R_{SR} - R_{GR} \\ R_{CO_2} & = & R_{WGS} + R_{GR} \\ R_{H_2} & = & 3R_{SR} + R_{WGS} + 4R_{GR} \\ R_{CO} & = & R_{SR} - R_{GR} \\ R_{H_2O} & = & -R_{SR} - R_{WGS} - 2R_{GR} \end{array} \tag{3.4}$$

  The rates of reaction are given by:

$$\begin{array}{rcl} R_{SR} & = & k_1 \cdot \exp\left(-\dfrac{E_1}{R_m \cdot T}\right) \cdot \dfrac{p_{CH_4} \cdot p_{H_2O} - p_{H_2}^3 \cdot p_{CO}}{\exp\left(\frac{-26830}{T} + 30.144\right)} \\ R_{WGS} & = & k_3 \cdot \exp\left(-\dfrac{E_3}{R_m \cdot T}\right) \cdot \dfrac{p_{CO} \cdot p_{H_2O} - p_{H_2} \cdot p_{CO_2}}{\exp\left(\frac{4400}{T} - 4.036\right)} \\ R_{GR} & = & k_2 \cdot \exp\left(-\dfrac{E_2}{R_m \cdot T}\right) \cdot \dfrac{p_{CH_4} \cdot p_{H_2O}^2 - p_{H_2}^4 \cdot p_{CO_2}}{\exp\left(\frac{-26830}{T} + 30.144\right) \cdot \exp\left(\frac{4400}{T} - 4.036\right)} \end{array} \tag{3.5}$$

  with the corresponding parameters,

$$\begin{array}{rcll} k_1 & = & 5.19\text{E}9 & [\text{MPa}^2] \\ k_2 & = & 9.9\text{E}3 & [-] \\ k_3 & = & 1.32\text{E}10 & [\text{MPa}^2] \\ E_1 & = & 257.01\text{E}3 & [\text{kJ/mol}] \\ E_2 & = & 89.23\text{E}3 & [\text{kJ/mol}] \\ E_3 & = & 236.7\text{E}3 & [\text{kJ/mol}] \end{array}$$

  The rates of reaction are further integrated along the span s (length of the reformer) to obtain the mass flows:

$$\begin{array}{rcl} d\dot{n}_{CH_4} \cdot ds & = & (1-b) \cdot \rho_{cat} \cdot R_{CH_4} \cdot A \\ d\dot{n}_{CO_2} \cdot ds & = & (1-b) \cdot \rho_{cat} \cdot R_{CO_2} \cdot A \\ d\dot{n}_{H_2} \cdot ds & = & (1-b) \cdot \rho_{cat} \cdot R_{H_2} \cdot A \\ d\dot{n}_{CO} \cdot ds & = & (1-b) \cdot \rho_{cat} \cdot R_{CO} \cdot A \\ d\dot{n}_{H_2O} \cdot ds & = & (1-b) \cdot \rho_{cat} \cdot R_{H_2O} \cdot A \end{array} \tag{3.6}$$

  with,

$$\begin{array}{lcrcll} \text{Porosity} & : & b & = & 0.4 & [-] \\ \text{Molar concentration of catalyst} & : & \rho_{cat} & = & 1870 & [\text{mol/dm}^3] \\ \text{Area of the reformer} & : & A & = & 1 & [\text{dm}^2] \end{array}$$

  Fig 3.1 shows the evolution of the composition of the fluid as a function of the length of the reformer. The inputs are 0.02 mol/s of methane and 0.04 mol/s

of water at 900°C and 200 kPa. The length of the span abviously influences the output composition.

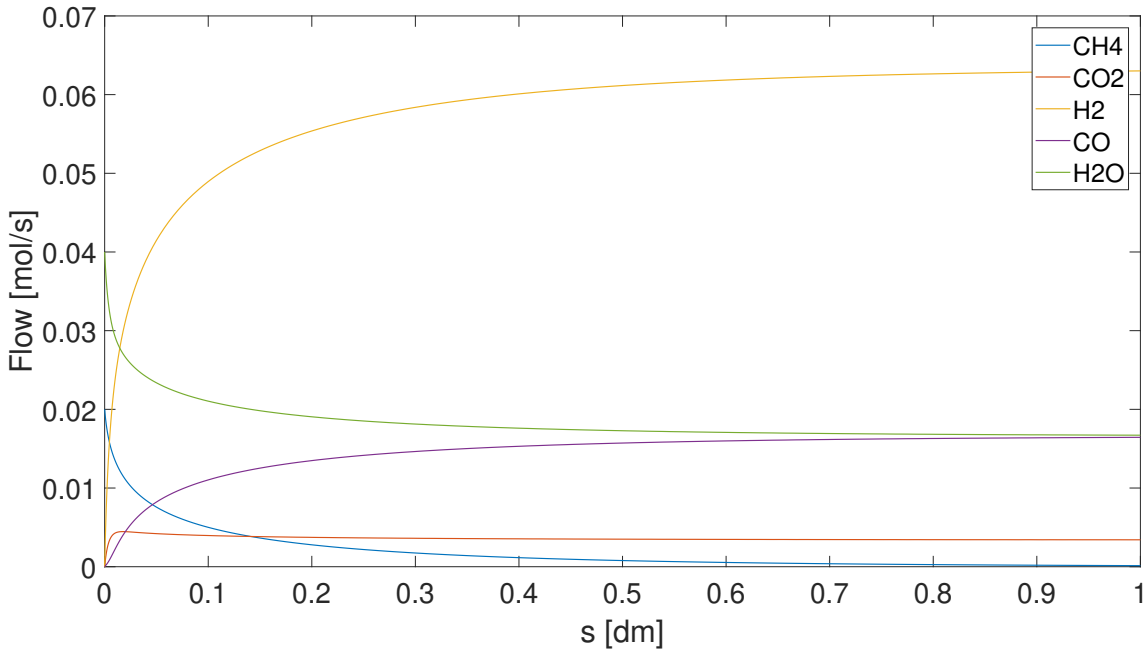

Figure 3.1: Composition of the fluid [mol/s] along the reformer span [dm] (T = 1173.15 [K], p_t = 200 [kPa], $\dot{m}_{CH_4}$ = 3.2E-4 [kg/s], $\dot{m}_{H_2O}$ = 7.2E-4 [kg/s]).

- Operating temperature of the reformer

  The temperature evolution along the span is obtained by energy balance:

$$dT \cdot ds = \frac{(1-b) \cdot \rho_{cat} \cdot (-\Delta H_{SR} \cdot R_{SR} - \Delta H_{WGS} \cdot R_{WGS} \cdot \Delta H_{GR} \cdot R_{GR})}{c_p \cdot \rho_{gas} \cdot \dot{V}} \tag{3.7}$$

  with,

Heat capacity of the gas	:	c_p	=	0.4	10· kJ/(kg· K)
Density of the gas	:	ρ_{gas}	=	0.2	[kg/m^3]
Volume flow	:	$\dot{V}$	=	$\frac{\dot{n}_t \cdot R_m \cdot T}{p_t}$	[m^3/s]
Enthalpy change of SR	:	ΔH_{SR}	=	206	[kJ/mol]
Enthalpy change of WGS	:	ΔH_{WGS}	=	-41	[kJ/mol]
Enthalpy change of GR	:	ΔH_{GR}	=	165	[kJ/mol]

  The steam reforming reaction is endothermic hence temperature decreases along the length as shown in Fig 3.2.

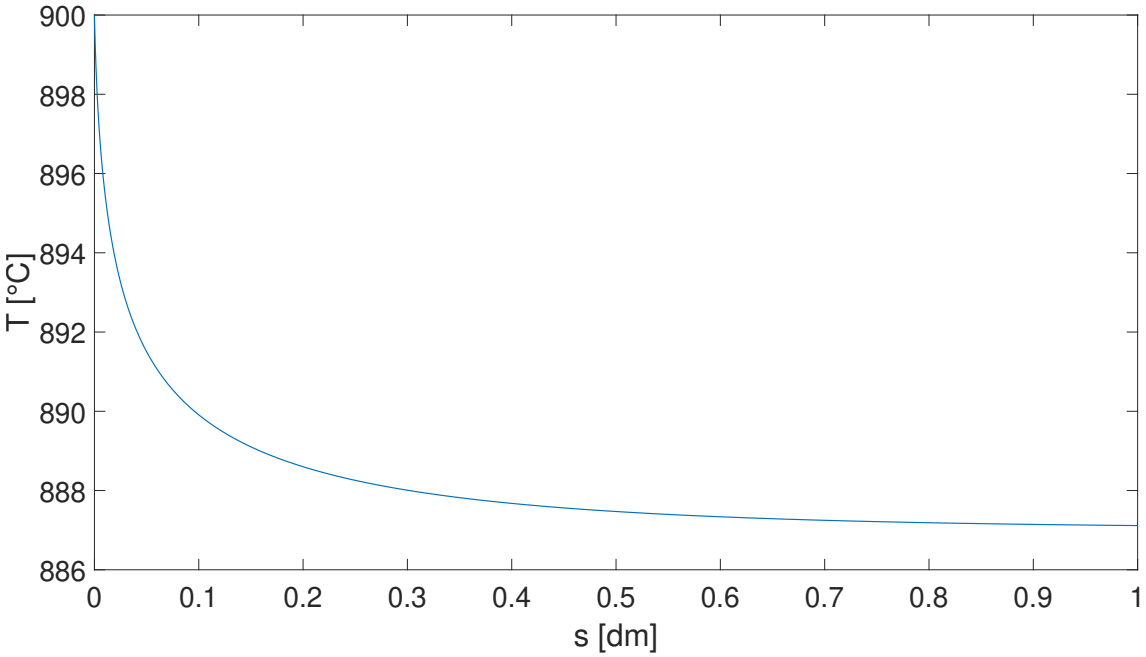

Figure 3.2: Temperature of the fluid [°C] along the reformer span [dm] ($T = 900$°C, $p_t = 200$ kPa, $\dot{m}_{CH_4} = 3.2$E-4 [kg/s], $\dot{m}_{H_2O} = 7.2$E-4 [kg/s]).

In the case of internal reforming, heat is directly transferred from the anode reaction site to the reforming site. It is assumed that the temperature along the reformer span is constant and equal to that of the SOFC stack operating temperature and that no temperature gradients are present. This requires a proper design of the SOFC stack.

- Operating pressure of the reformer :

  No pressure losses are considered in the reformer.

3.1.2 Influence of operating conditions

The optimization of the reformer is important since it produces the hydrogen necessary for the anode side reaction.

Water/methane ratio

The amount of water introduced at the inlet of the reformer significantly influences the reaction rates. The conversion ratio can be optimized to maximize the product flow of hydrogen which ensures the best efficiency of the fuel cell.

The conversion ratio is defined by:

$$C_R = \frac{\dot{n}_{CH_4,i} - \dot{n}_{CH_4,o}}{\dot{n}_{CH_4,i}} \tag{3.8}$$

The objective is to obtain a conversion ratio of minimum 95% by increasing step by step the amount of water introduced at the inlet. Therefore, a convergence loop (Fig. 3.4) is implemented which seeks the appropriate amount of inlet water.

Fig. 3.3 shows the evolution of the conversion ratio as a function of the water input. It can be seen that increasing the operating temperature allows to decrease the amount of water required to maximize the value of the conversion ratio.

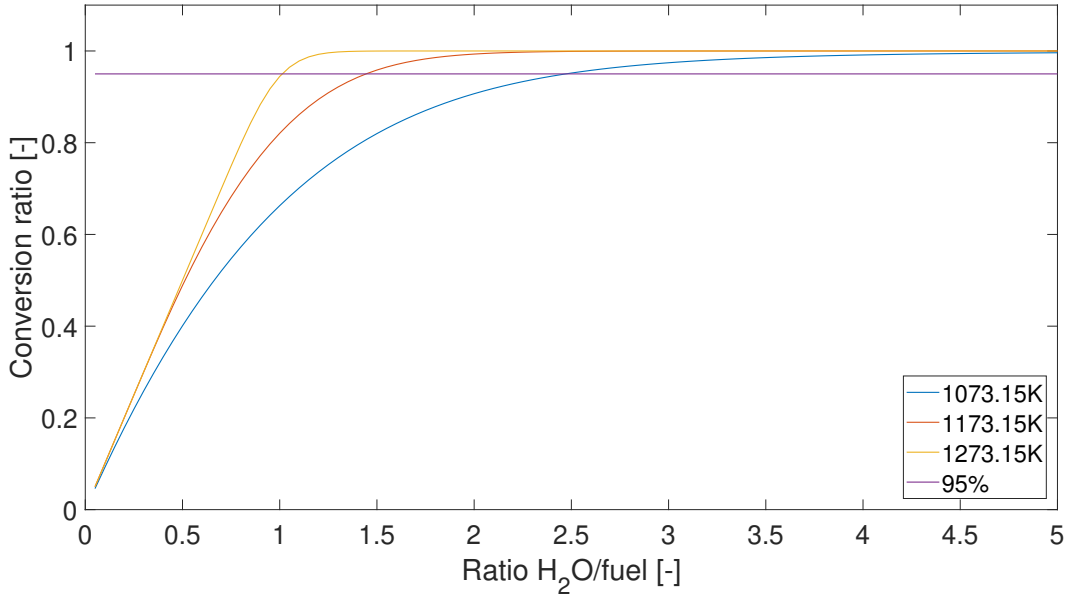

Figure 3.3: Conversion of the methane in hydrogen [-] as a function of the water input [kg/s] for different temperatures [K] (s = 10 [cm], p_t = 200 [kPa], $\dot{m}_{CH_4}$ = 3.2E-4 [kg/s]).

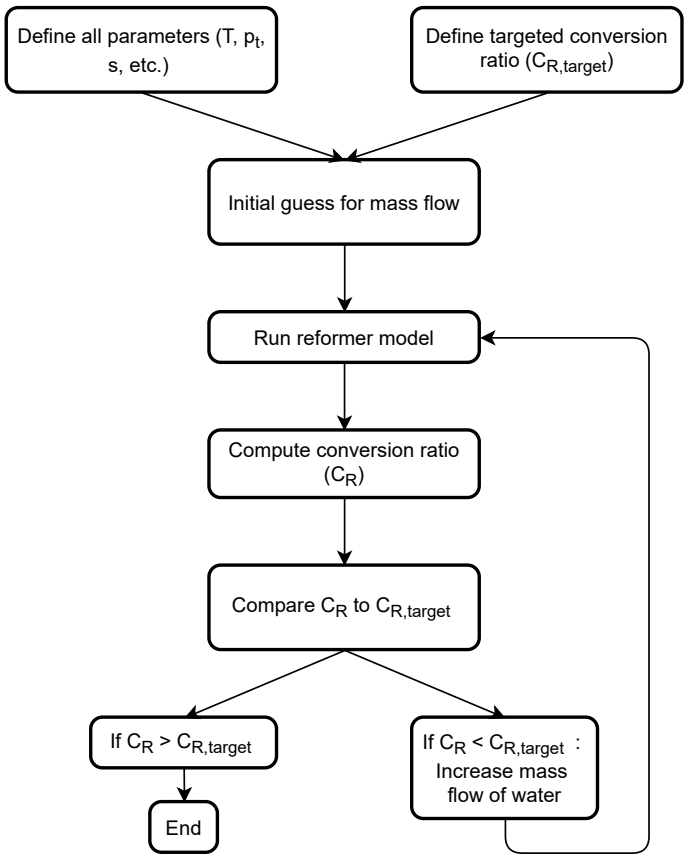

Figure 3.4: Flowchart of the conversion ratio optimization loop.

Span

The span influences the output composition of the reformer as seen in Fig. 3.1. Fig 3.5 shows the evolution of the outlet flow of hydrogen as a function of the span length. It can be seen that the flow can be increased significantly by increasing the span but reaches an asymptote.

SOFC operating Temperature

Fig 3.6 shows the outlet mass flow of hydrogen for different uniform reformer temperatures. The interesting SOFC interval of operating temperature is between 800°C and 1000°C. The reformer is then working close to its optimum.

Pressure

The shape observed in Fig 3.7 is similar to the one of Fig. 3.5. The same conclusions can thus be formulated. A minimum pressure allows to have a good outlet flow but increasing the pressure does not lead to a significant increase in hydrogen conversion.

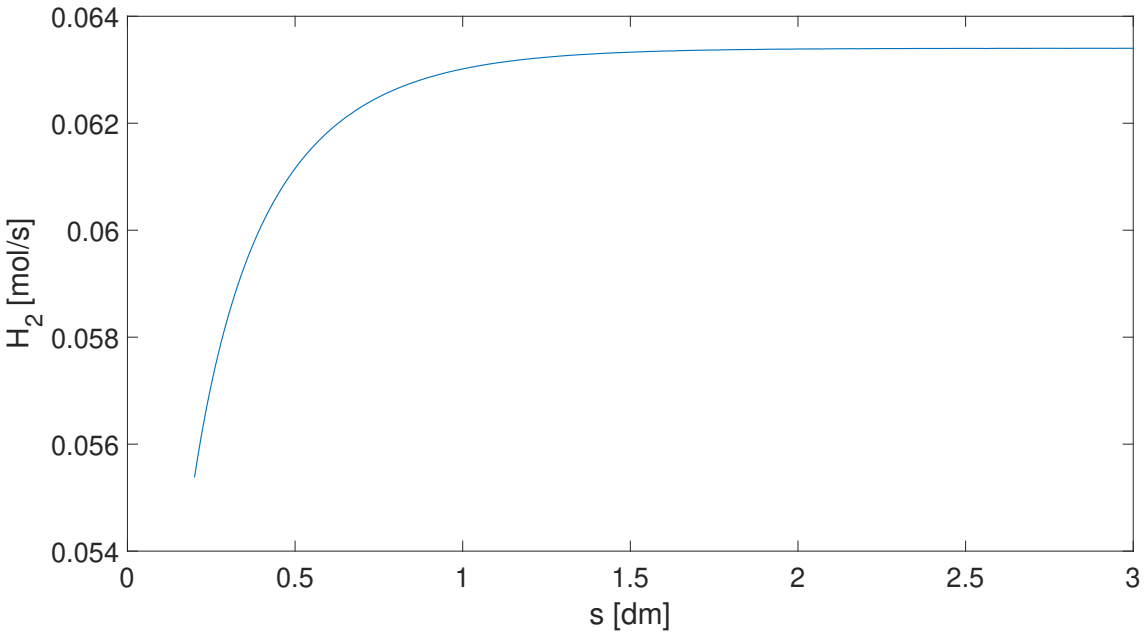

Figure 3.5: Outlet mass flow of hydrogen [mol/s] for different span lengths [dm] (T = 1173.15 [K], p_t = 200 [kPa], $\dot{m}_{CH_4}$ = 3.2E-4 [kg/s], $\dot{m}_{H_2O}$ = 7.2E-4 [kg/s]).

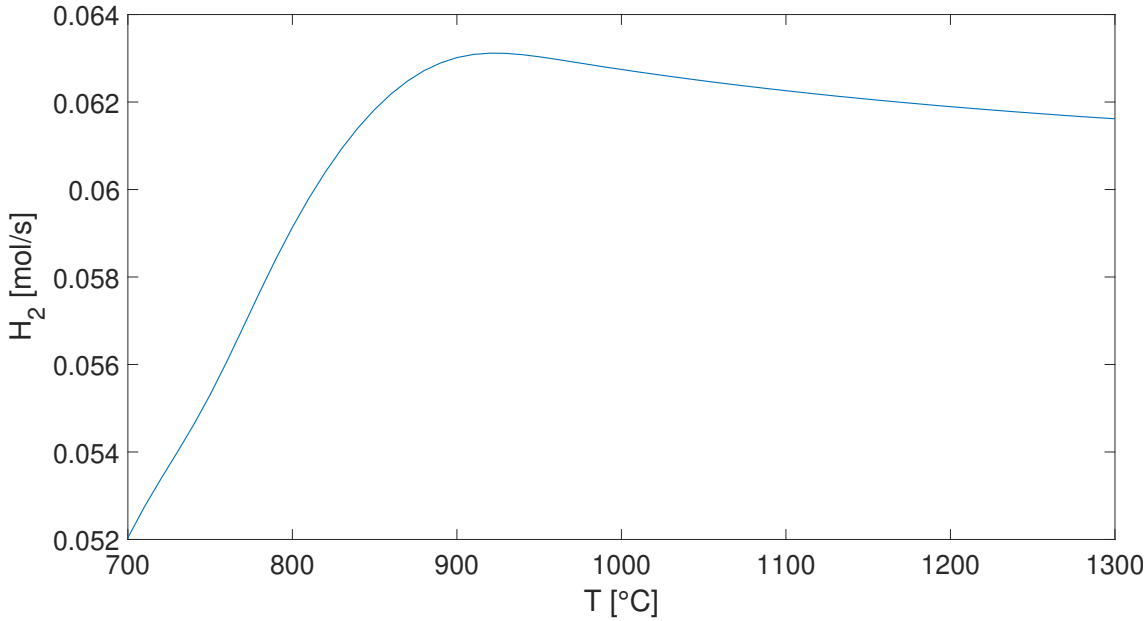

Figure 3.6: Outlet mass flow of hydrogen [mol/s] for different reformer temperatures [°C] ($s = 10$ [cm], $p_t = 200$ [kPa], $\dot{m}_{CH_4} = 3.2\text{E-}4$ [kg/s], $\dot{m}_{H_2O} = 7.2\text{E-}4$ [kg/s]).

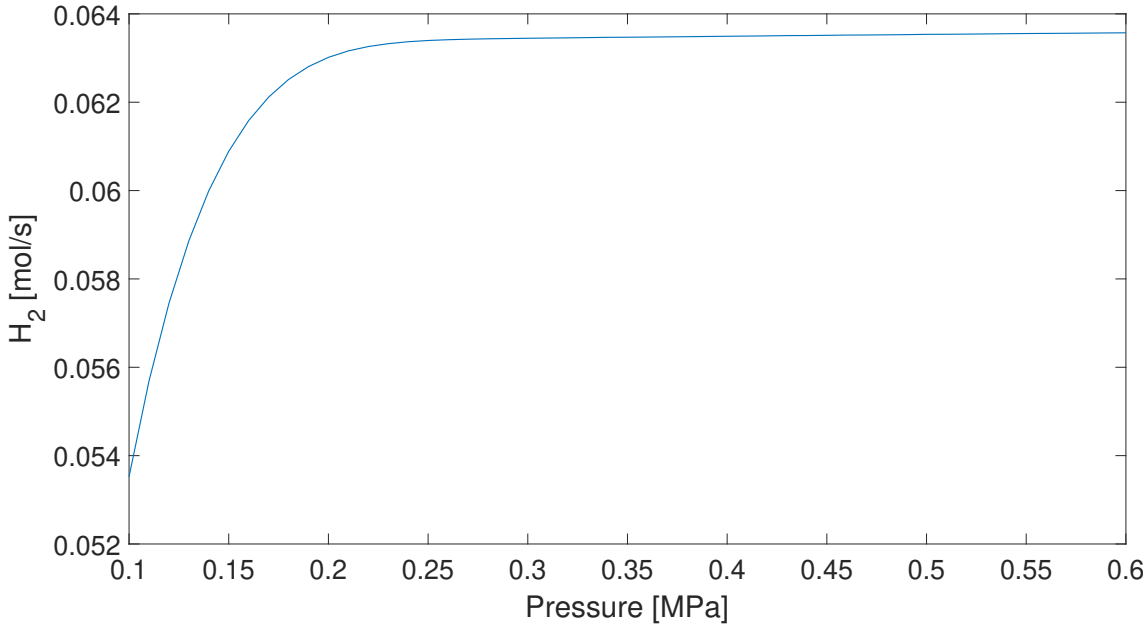

Figure 3.7: Outlet mass flow of hydrogen [mol/s] for different reformer pressures [MPa] ($T = 1173.15$ [K], $s = 10$ [cm], $\dot{m}_{CH_4} = 3.2\text{E-}4$ [kg/s], $\dot{m}_{H_2O} = 7.2\text{E-}4$ [kg/s]).

3.1.3 Concluding remarks

As the temperature and pressure are fixed by the SOFC, no control is possible on these variables. Nevertheless, Fig. 3.6 and Fig. 3.7 have shown that the interval of SOFC operating temperature and pressure allow the reformer to work close to its optimal point. Regarding the span effect, it can be tuned while taking into account the SOFC design and the constraint of the vehicle size. It is fixed to 10 cm in the simulations further performed in this work.

3.2 Water recirculation

Limiting the amount of water to be heated for the steam reforming process reduces the energy input in the system which improves efficiency. The ratio of water to fuel should exceed 1 (Fig. 3.3) to yield a good conversion ratio. Recycling of the water produced by the SOFC at its anode shall be therefore useful which is illustrated in Fig. 3.8. We however account for an extra 10% of the total mass flow of water (see Section 3.1.1) to ensure that there is always water inside the SOFC. That extra water amount has been randomly fixed but can be tuned to reach the desired behavior. Such recirculation has been implemented in our modelling tool (Fig. 3.9) through a convergence loop which allows than to obtain the recirculation ratio to reach the objective.

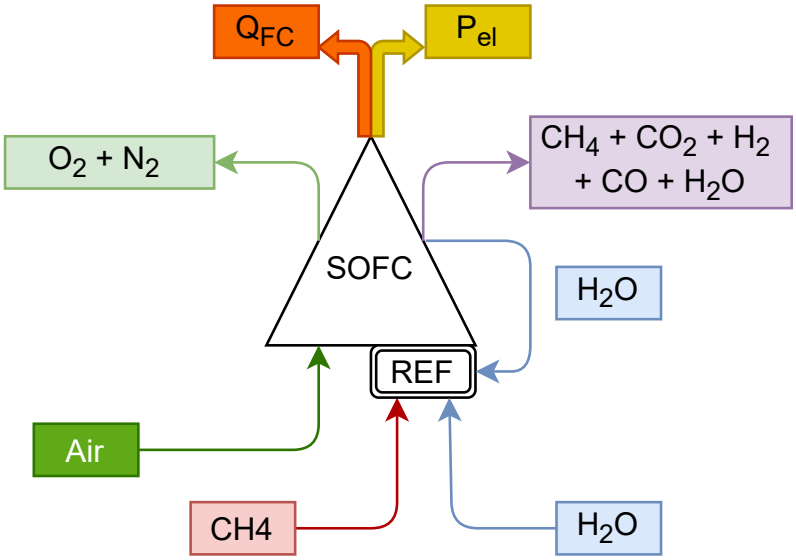

Figure 3.8: Illustration of water recirculation.

The total mass flow of water required, which is an output of the convergence loop of Section 3.1.1, is decomposed into a recycled and a non-recycled part:

$$\dot{m}_{H_2O,i} = \dot{m}_{H_2O,rec} + \dot{m}_{H_2O,non-rec} \tag{3.9}$$

Let us define the water recirculation ratio (R_R) as the percentage of water recycled from the anode outlet:

$$R_R = \frac{\dot{m}_{H_2O,rec}}{\dot{m}_{H_2O,o}} \tag{3.10}$$

The non-recycled mass flow is fixed to 10% of the total mass flow while the recycled mass flow corresponds to the recirculation ratio (R_R) times the flow of water at the outlet of the SOFC.

$$\dot{m}_{H_2O,i} = R_R \cdot \dot{m}_{H_2O,o} + 0.1 \cdot \dot{m}_{H_2O,i} \tag{3.11}$$

The recirculation ratio can then be determined to match the 10%.

$$R_R = \frac{\dot{m}_{H_2O,i} - 0.1 \cdot \dot{m}_{H_2O,i}}{\dot{m}_{H_2O,o}} \tag{3.12}$$

A high recirculation of water will reduce the amount of external water to heat up which will improve efficiency. The following example[1] assumes a 10% of non-recycled water and a required total mass flow of water of 4.95E-4 kg/s to be injected in the reformer. The recirculation ratio is calculated and is equal to 52% of the output mass flow. The mass flow that has to be added is then equal to 4.5752E-5 kg/s. Table 3.1 shows the required power to heat up the water from 298.15 K until 1173.15 K at 200 [kPa] without recirculation ($\dot{m}_{H_2O}$ = 4.95E-4 [kg/s]) and with recirculation ($\dot{m}_{H_2O}$ = 4.5752E-5 [kg/s]). It can be seen that the power required is decreased by about 90%.

	No recirculation	**With recirculation (52%)**
Power [W]	2125	196

Table 3.1: Power required to heat water from 298.15 [K] until 1173.15 [K] at 200 [kPa] with no recirculation and with recirculation (52%).

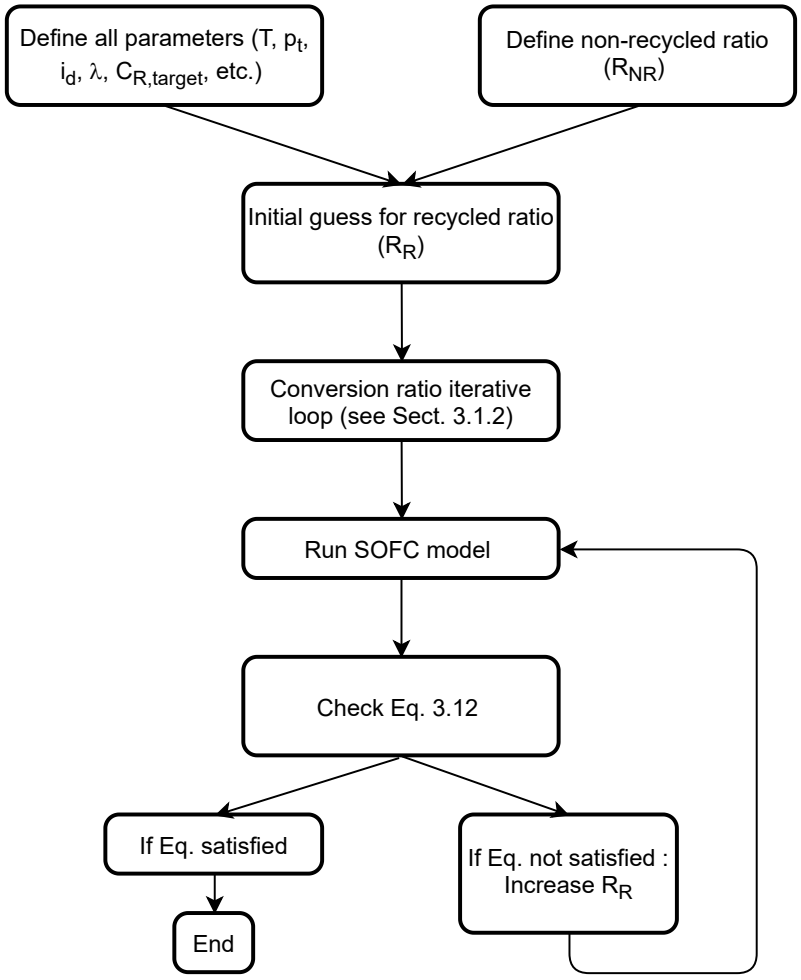

Figure 3.9: Flowchart of water recirculation.

[1]Simulation parameters are : T = 1173.15 [K], p_t = 200 [kPa], U_f = 0.7 [-], λ = 1.5 [-], $\dot{m}_{CH_4}$ = 3.2E-4 [kg/s].

3.3 Anode gas recirculation

Anode gas recirculation is interesting for several reasons [58]. On one hand, it is required for water recycling. Indeed, it would be very difficult to separate the water from the outlet anode gas. On the other hand, since anode exhaust gas still contains fuel, it is useful to reuse it to reduce the amount of fuel injected in the reformer as well as to limit additional post combustion in the after burner. This is especially important in the combination of an SOFC with a gas turbine since the inlet turbine temperature must be limited due to material constraints. More fuel in the combustor means extra air to be compressed which impacts global efficiency. This effect will be further discussed in Chapter 6.

Anode gas recirculation is implemented in a similar way to water recirculation except that the anode gas recirculation ratio is imposed as an input parameter. Details on the simulation model and principles are given in Annex A.

Fig 3.10 illustrates the recirculation happening inside the SOFC. We assume that an ejector is implemented to actually perform the recirculation. An ejector is a device capable of sucking the outlet gas from the anode to redirect part of that flow into the reformer inlet using the venturi effect. Fig 3.11 illustrates the position of the ejector inside a SOFC system. It is represented by a suction chamber, a mixing chamber and a diffuser (Fig. 3.12) and its performance is mainly influenced by operating temperature, pressure and fluids. Its modelling can be found in the literature but was not implemented in this model ([46] [67]).

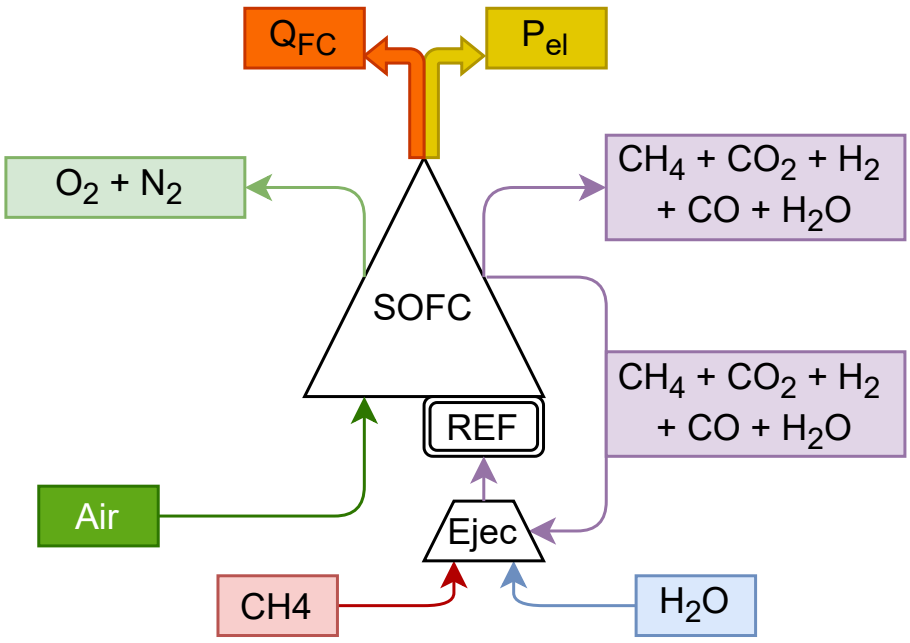

Figure 3.10: Illustration of the recirculation of the anode exhaust gas.

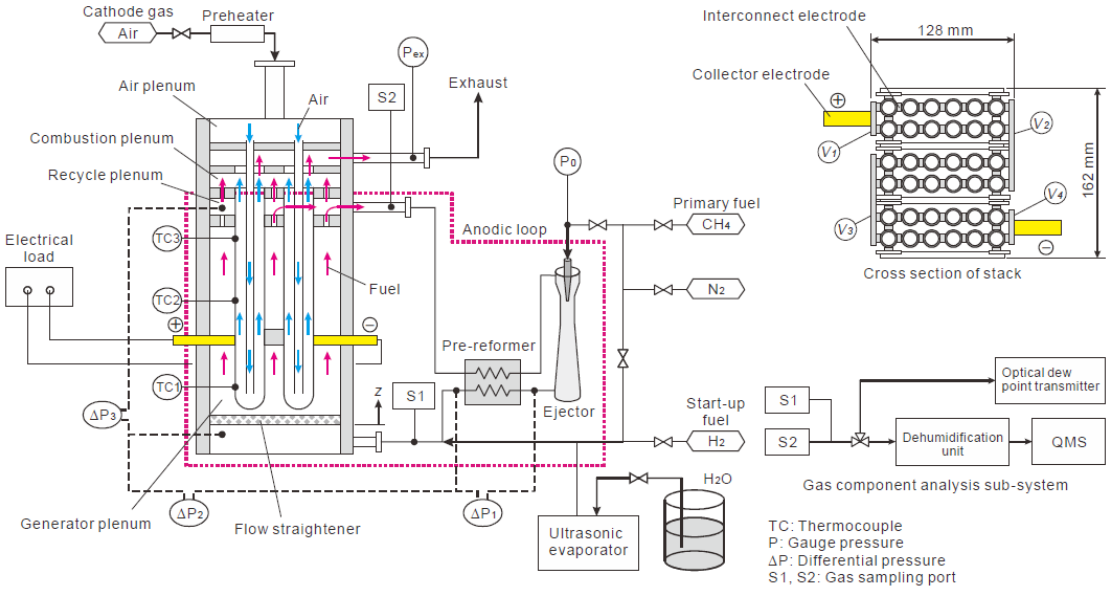

Figure 3.11: Illustration of an SOFC combined with an ejector [4].

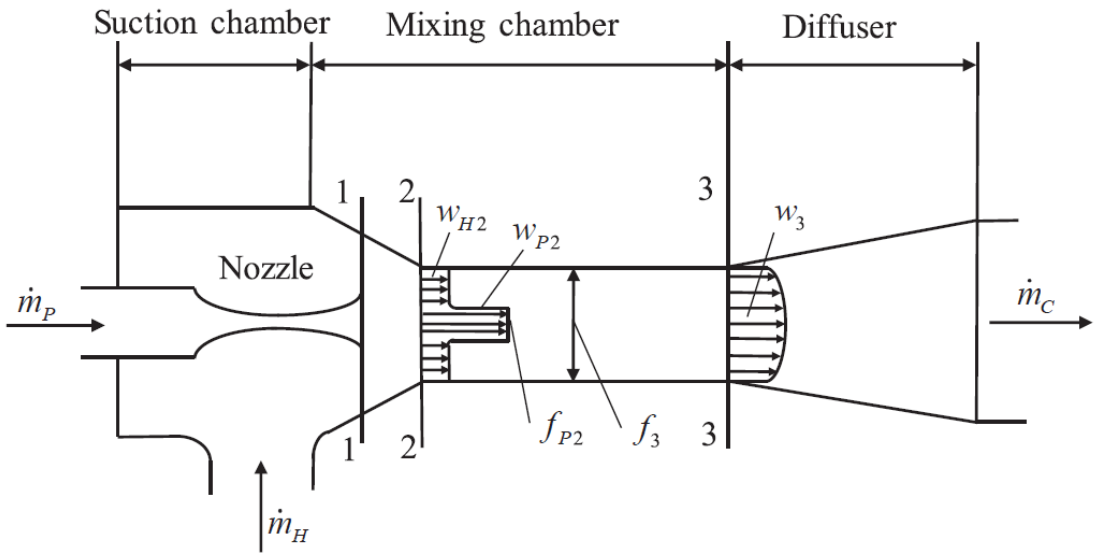

Figure 3.12: Schema of an ejector [67].

3.3.1 Application

In this section, we compare the performance of a SOFC stack with and without anode recirculation as presented in Chapter 2. The recirculation ratio (R_R) is considered equal to 0.7 which is a feasible value according to [55].

Fig. 3.13 and 3.14 clearly show that recirculation has a negative effect on output voltage and electric power density which is more prominent at larger current densities. This is explained by a lower molar concentration of hydrogen in the anode gas inlet in the case of recirculation as presented in Table 3.2. Recirculation also yields a lower limiting current density.

Molar concentration [%]	CH_4	CO_2	H_2	CO	H_2O
No recirculation	1.1031	1.8091	68.5841	20.4492	8.0545
With recirculation	0.8241	3.4136	60.6097	23.4660	11.6866

Table 3.2: Composition of the inlet anode gas [%] with and without recirculation (R_R = 0.7 [-], T = 1173.15 [K], p_t = 200 [kPa], U_f = 0.7 [-], λ = 1.5 [-], $\dot{m}_{CH_4}$ = 3.2E-4 [kg/s], $\dot{m}_{H_2O,NR}$ = 4.95E-4 [kg/s], $\dot{m}_{H_2O,R}$ = 6.68E-4 [kg/s]).

On the contrary, Fig. 3.15 shows an important increase for the efficiency. Indeed, considering its definition as:

$$\eta_{SOFC} = \frac{P_{el}}{\dot{m}_{CH_4} \cdot LHV_{CH_4}} \tag{3.13}$$

The same electrical power output is obtained with a lower input of methane according to Table 3.3 which increases efficiency.

	$\dot{m}_{CH_4}$ [kg/s]
No recirculation	3.2E-4
With recirculation	2.544E-4

Table 3.3: Mass flow of methane [kg/s] to obtain two corresponding electric powers with and without recirculation (R_R = 0.7 [-], T = 1173.15 [K], p_t = 200 [kPa], U_f = 0.7 [-], λ = 1.5 [-]).

For the sake of completion, the evolution of the number of cells and generated heat as a function of the current density are listed in Appendix C.

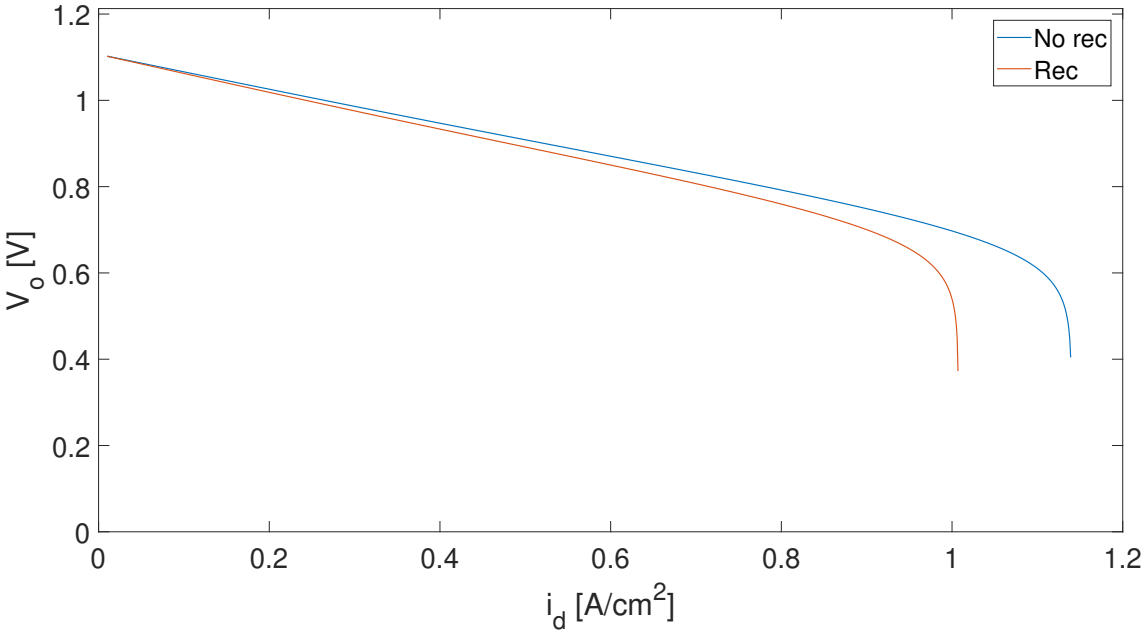

Figure 3.13: Output voltage [V] as a function of the current density [A/cm²] with recirculation and without recirculation at the anode. (R_R = 0.7 [-], T = 1173.15 [K], p_t = 200 [kPa], U_f = 0.7 [-], λ = 1.5 [-], $\dot{m}_{CH_4}$ = 3.2E-4 [kg/s], $\dot{m}_{H_2O,NR}$ = 4.95E-4 [kg/s], $\dot{m}_{H_2O,R}$ = 6.68E-4 [kg/s]).

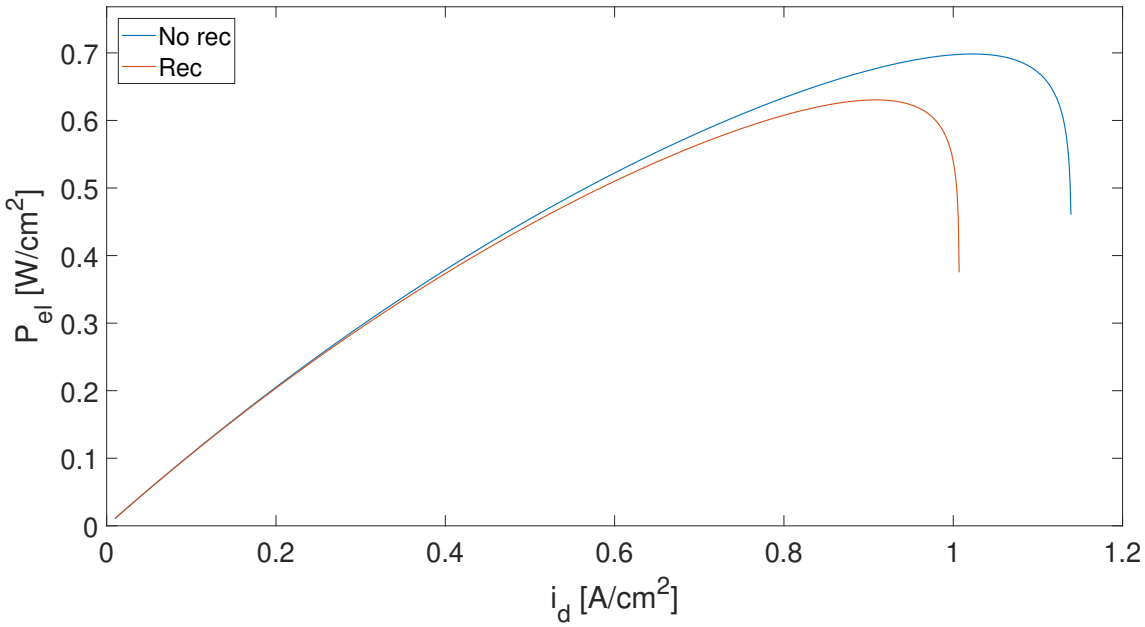

Figure 3.14: Power density [W/cm²] as a function of the current density [A/cm²] with recirculation and without recirculation at the anode. ($R_R = 0.7$ [-], $T = 1173.15$ [K], $p_t = 200$ [kPa], $U_f = 0.7$ [-], $\lambda = 1.5$ [-], $\dot{m}_{CH_4} = 3.2\text{E-}4$ [kg/s], $\dot{m}_{H_2O,NR} = 4.95\text{E-}4$ [kg/s], $\dot{m}_{H_2O,R} = 6.68\text{E-}4$ [kg/s]).

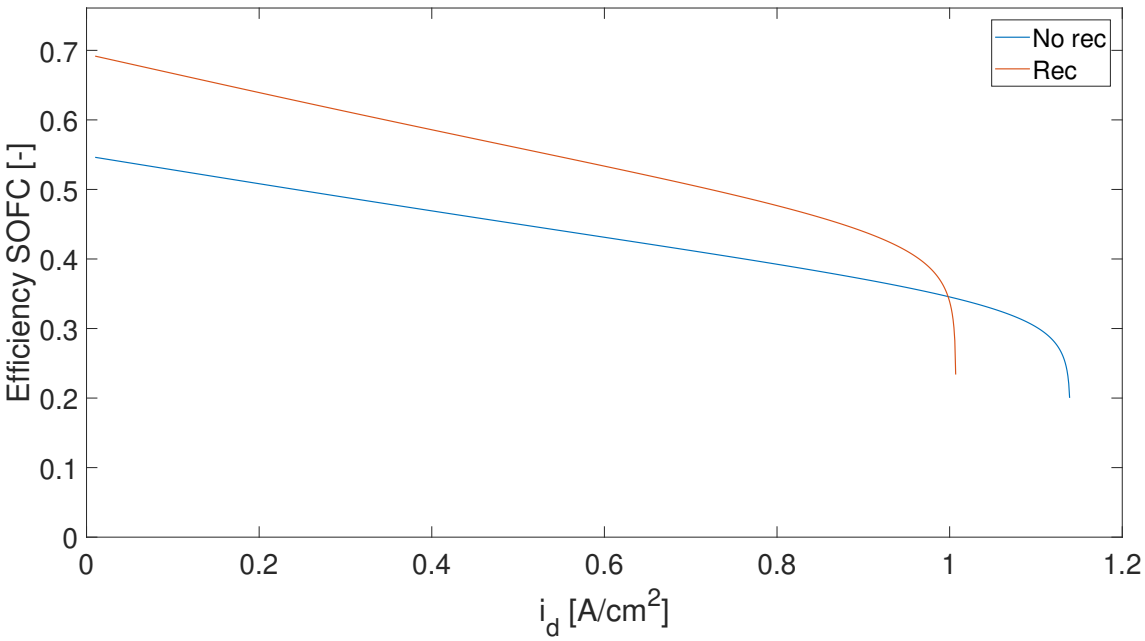

Figure 3.15: Efficiency of the SOFC [-] as a function of the current density [A/cm²] with recirculation and without recirculation at the anode. ($R_R = 0.7$ [-], $T = 1173.15$ [K], $p_t = 200$ [kPa], $U_f = 0.7$ [-], $\lambda = 1.5$ [-], $\dot{m}_{CH_4} = 3.2\text{E-}4$ [kg/s], $\dot{m}_{H_2O,NR} = 4.95\text{E-}4$ [kg/s], $\dot{m}_{H_2O,R} = 6.68\text{E-}4$ [kg/s]).

Chapter 4

Auxiliaries modelling

In addition to the stack and reformer, an SOFC system also involves additional components such as compressors, turbines, heat exchangers, bypasses, filters, etc. In this chapter, we will detail the modelling aspects of these extra components. Since the thermophysical properties are computed using REFPROP, a generic notation, $RP(X, Y)$, is used throughout this chapter to denote a REFPROP function call retrieving a particular thermodynamic property value based on two variables.

4.1 Compressor and pump

A compressor is a device capable of increasing the energy contained in the fluid by compression. We use a basic modelling approach only using isentropic efficiency and fixed compression ratio. In a further development of the model, performance maps relating efficiency and pressure ratio with respect to rotation speed and mass flows could be used [38].

- Inputs :

Inlet temperature	:	T_i	[K]
Inlet pressure	:	p_i	[kPa]
Mass flow	:	$\dot{m}$	[kg/s]
Compression ratio	:	r_p	[-]
Isentropic efficiency	:	η_{is}	[-]
Composition of the fluid	:	C	[-]

- Calculations :

Inlet enthalpy	:	$h_i = RP(T_i, p_i)$	[J/kg]
Inlet entropy	:	$s_i = RP(T_i, p_i)$	[J/kg·K]
Outlet pressure	:	$p_o = r_p \cdot p_i$	[kPa]
Isentropic outlet enthalpy	:	$h_{is,o} = RP(p_o, s_i)$	[J/kg]
Outlet enthalpy	:	$h_o = h_i + \dfrac{h_{is,o} - h_i}{\eta_{is}}$	[J/kg]

- Outputs :

$$\text{Power} \quad : \quad P_{cp} = \dot{m} \cdot (h_o - h_i) \quad [\text{W}]$$

No leakage is assumed through the compressor.

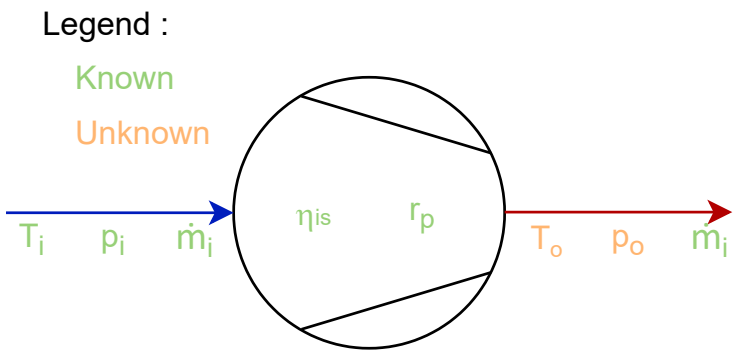

Figure 4.1: Compressor and pump model.

4.2 Turbine

A turbine extracts energy from the fluid by expansion. A basic model is devised similarly to the compressor. Again, the modelling could be improved by using performance maps.

- Inputs :

Inlet temperature	:	T_i	[K]
Inlet pressure	:	p_i	[kPa]
Mass flow	:	$\dot{m}$	[kg/s]
Expansion ratio	:	r_p	[-]
Isentropic efficiency	:	η_{is}	[-]
Composition of the fluid	:	C	[-]

- Calculations :

Inlet enthalpy	:	$h_i = RP(T_i, p_i)$	[J/kg]
Inlet entropy	:	$s_i = RP(T_i, p_i)$	[J/kg·K]
Outlet pressure	:	$p_o = \dfrac{p_i}{r_p}$	[kPa]
Isentropic outlet enthalpy	:	$h_{is,o} = RP(p_o, s_i)$	[J/kg]
Outlet enthalpy	:	$h_o = h_i + (h_{is,o} - h_i) \cdot \eta_{is}$	[J/kg]

- Outputs :

$$\text{Power} \quad : \quad P_{tu} = \dot{m} \cdot (h_i - h_o) \quad [\text{W}]$$

No leakage is assumed through the turbine.

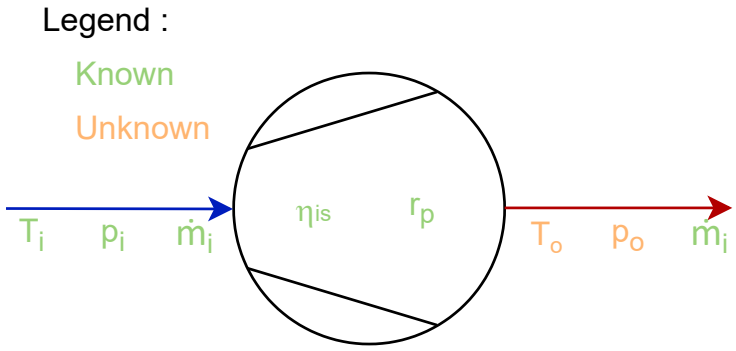

Figure 4.2: Turbine model.

4.3 Heat exchanger

The model of the heat exchanger is based on its pressure losses and its thermal efficiency. The pressure losses are supposed independent of the mass flow and identical for both fluids. The cold fluid at the inlet corresponds to the index 1 while the hot fluid at the inlet corresponds to the index 2.

- Inputs :

Inlet temperature of cold fluid	:	$T_{i,1}$	[K]
Inlet temperature of hot fluid	:	$T_{i,2}$	[K]
Inlet pressure of cold fluid	:	$p_{i,1}$	[kPa]
Inlet pressure of hot fluid	:	$p_{i,2}$	[kPa]
Mass flow of cold fluid	:	$\dot{m}_1$	[kg/s]
Mass flow of hot fluid	:	$\dot{m}_2$	[kg/s]
Efficiency	:	η	[-]
Pressure loss	:	ΔP	[kPa]
Fluid with lowest energy change	:	1 or 2	
Composition of cold fluid	:	C_1	[-]
Composition of hot fluid	:	C_2	[-]

- Calculations :

Inlet enthalpy of cold fluid	:	$h_{i,1} = RP(T_{i,1}, p_{i,1})$	[J/kg]
Inlet enthalpy of hot fluid	:	$h_{i,2} = RP(T_{i,2}, p_{i,2})$	[J/kg]
Outlet pressure of cold fluid	:	$p_{o,1} = p_{i,1} - \Delta P$	[kPa]
Outlet pressure of hot fluid	:	$p_{o,2} = p_{i,2} - \Delta P$	[kPa]
Maximum enthalpy of cold fluid	:	$h_{m,1} = RP(T_{i,2}, p_{i,2})$	[J/kg]
Minimum enthalpy of hot fluid	:	$h_{m,2} = RP(T_{i,1}, p_{i,1})$	[J/kg]
Minimum energy	:	$Q_{min} = \dot{m}_{1/2} \cdot \lVert h_{i,1/2} - h_{m,1/2} \rVert$	[W]
Energy exchanged	:	$Q_{exch} = \eta \cdot Q_{min}$	[W]
Outlet enthalpy of cold fluid	:	$h_{o,1} = h_{i,1} + \dfrac{Q_{exch}}{\dot{m}_1}$	[J/kg]
Outlet enthalpy of hot fluid	:	$h_{o,2} = h_{i,2} - \dfrac{Q_{exch}}{\dot{m}_2}$	[J/kg]

- Outputs :

Outlet temperature of cold fluid	:	$T_{o,1} = RP(p_{o,1}, h_{o,1})$	[K]
Outlet temperature of hot fluid	:	$T_{o,2} = RP(p_{o,2}, h_{o,2})$	[K]

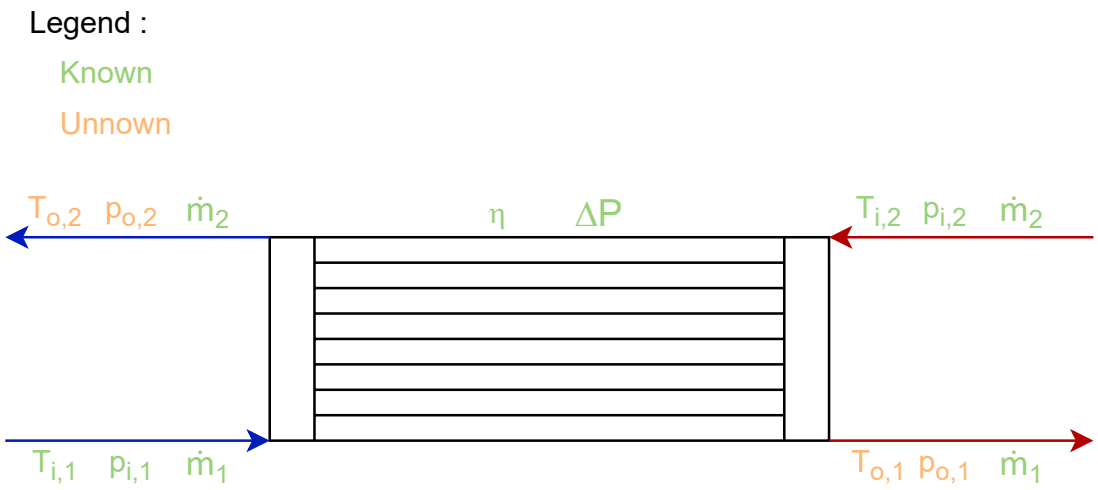

Figure 4.3: Heat exchanger model.

4.3.1 Vaporizer

Vaporization of water is required by the reformer which happens in the vaporizer component. The objective is to predict the outlet temperatures and to compute the required power to vaporize the water. No overheating is implemented.

- Inputs :

Inlet temperature of water	:	$T_{i,1}$	[K]
Inlet temperature of hot fluid	:	$T_{i,2}$	[K]
Inlet pressure of water	:	$p_{i,1}$	[kPa]
Inlet pressure of hot fluid	:	$p_{i,2}$	[kPa]
Quality of water at boiling temperature	:	$w = 1$	[-]
Pressure loss	:	ΔP	[kPa]
Mass flow of water	:	$\dot{m}_1$	[kg/s]
Mass flow of hot fluid	:	$\dot{m}_2$	[kg/s]
Composition of water	:	C_1	[-]
Composition of hot fluid	:	C_2	[-]

- Calculations :

Inlet enthalpy of water	:	$h_{i,1} = RP(T_{i,1}, p_{i,1})$	[J/kg]
Outlet pressure of water	:	$p_{o,1} = p_{i,1} - \Delta P$	[kPa]
Outlet pressure of hot fluid	:	$p_{o,2} = p_{i,2} - \Delta P$	[kPa]
Boiling temperature of water	:	$T_{vap,1} = RP(p_{o,1}, w)$	[K]
Enthalpy at boiling temperature	:	$h_{vap,1} = RP(p_{o,1}, w)$	[J/kg]
Energy required to vaporize the water	:	$Q_{vap} = \dot{m}_1 \cdot (h_{vap,1} - h_{i,1})$	[W]
Outlet enthalpy of hot fluid	:	$h_{o,2} = h_{i,2} - \frac{Q_{vap}}{\dot{m}_2}$	[J/kg]

- Outputs :

Outlet temperature of hot fluid : $T_{o,2} = RP(p_{o,2}, h_{o,2})$ [K]

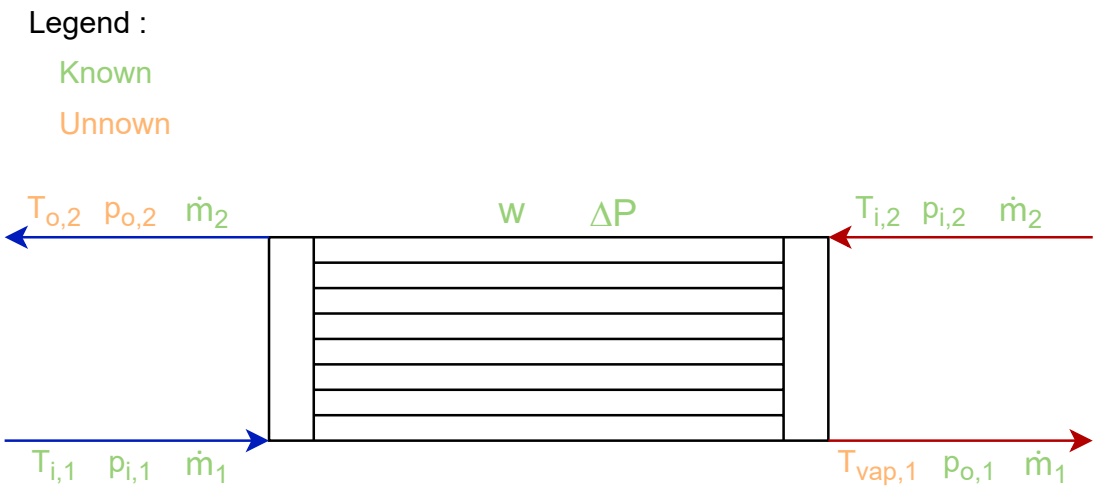

Figure 4.4: Vaporizer model.

4.3.2 Intercooler

An intercooler is required for the IRReGT cycle to cool down compressed air between the two compression stages which decreases the work of the second compressor. The temperature of the fluid entering the second compressor, the ΔT of the cooling water and the efficiency are fixed. The mass flow of the cooling water can then be calculated.

- Inputs :

Inlet temperature of water	:	$T_{i,1}$	[K]
Inlet temperature of hot fluid	:	$T_{i,2}$	[K]
Inlet pressure of water	:	$p_{i,1}$	[kPa]
Inlet pressure of hot fluid	:	$p_{i,2}$	[kPa]
Outlet temperature of water	:	$T_{o,1}$	[K]
Outlet temperature of hot fluid	:	$T_{o,2}$	[K]
Mass flow of hot fluid	:	$\dot{m}_2$	[kg/s]
Efficiency	:	η	[-]
Pressure loss	:	ΔP	[kPa]
Composition of water	:	C_1	[-]
Composition of hot fluid	:	C_2	[-]

- Calculations :

Inlet enthalpy of water	:	$h_{i,1} = RP(T_{i,1}, p_{i,1})$	[J/kg]
Inlet enthalpy of hot fluid	:	$h_{i,2} = RP(T_{i,2}, p_{i,2})$	[J/kg]
Outlet pressure of water	:	$p_{o,1} = p_{i,1} - \Delta P$	[kPa]
Outlet pressure of hot fluid	:	$p_{o,2} = p_{i,2} - \Delta P$	[kPa]
Outlet enthalpy of water	:	$h_{o,1} = RP(T_{o,1}, p_{o,1})$	[J/kg]
Outlet enthalpy of hot fluid	:	$h_{o,2} = RP(T_{o,2}, p_{o,2})$	[J/kg]
Energy needed to cool the hot fluid	:	$Q_{need} = \dot{m}_2 \cdot (h_{i,2} - h_{o,2})$	[W]
Real energy	:	$Q_{real} = \dfrac{Q_{need}}{\eta}$	[W]

- Outputs :

$$\text{Mass flow of water needed} \quad : \quad \dot{m}_1 = \frac{Q_{real}}{h_{o,1} - h_{i,1}} \quad [\text{kg/s}]$$

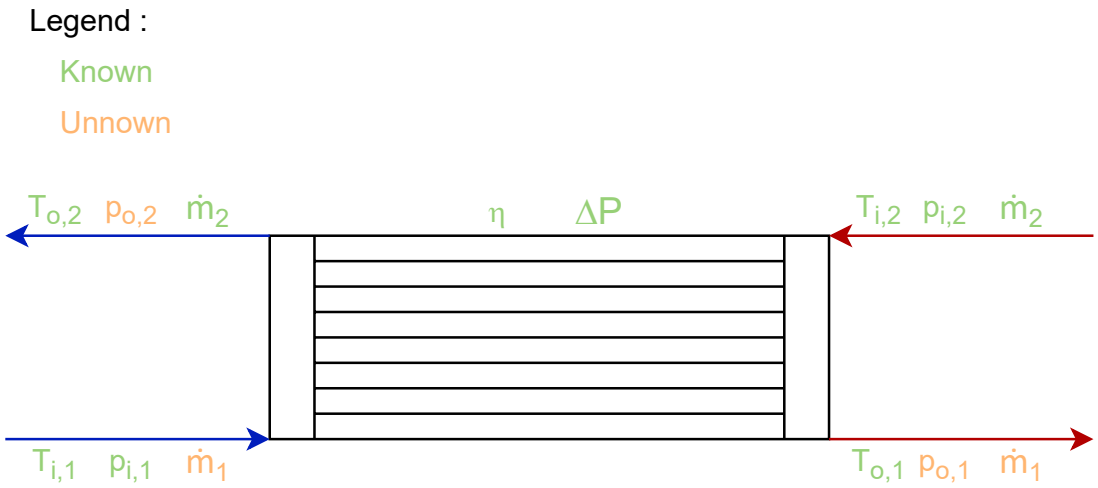

Figure 4.5: Intercooler model.

4.4 Bypass and mixer

A bypass separates the flow in multiple streams. However, we assume no additional pressure loss. Both outlets have the same thermodynamic properties (temperature, pressure, enthalpy, etc) as the inlet. The opening of the bypass determines the mass flows of the outlet streams which is denoted α.

A mixer is considered as a device with two inlets and one outlet. It is assumed that both fluids entering the box are perfectly mixed when exiting. No pressure loss is assumed.

- Inputs :

Inlet temperature of fluid 1	:	T_1	[K]
Inlet temperature of fluid 2	:	T_2	[K]
Inlet pressure of fluid 1	:	p_1	[kPa]
Inlet pressure of fluid 2	:	p_2	[kPa]
Mass flow of fluid 1	:	$\dot{m}_1$	[kg/s]
Mass flow of fluid 2	:	$\dot{m}_2$	[kg/s]
Composition of fluid 1	:	C_1	[-]
Composition of fluid 2	:	C_2	[-]

- Outputs :

Conservation of mass	:	$\dot{m}_3 = \dot{m}_1 + \dot{m}_2$	[kg/s]
Temperature of outlet fluid	:	$T_3 = \dfrac{T_1 \cdot \dot{m}_1 + T_2 \cdot \dot{m}_2}{\dot{m}_3}$	[K]
Pressure of outlet fluid	:	$p_3 = \dfrac{p_1 \cdot \dot{m}_1 + p_2 \cdot \dot{m}_2}{\dot{m}_3}$	[kPa]
Composition of outlet fluid	:	$C_3 = \dfrac{C_1 \cdot \dot{m}_1 + C_2 \cdot \dot{m}_2}{\dot{m}_3}$	[-]

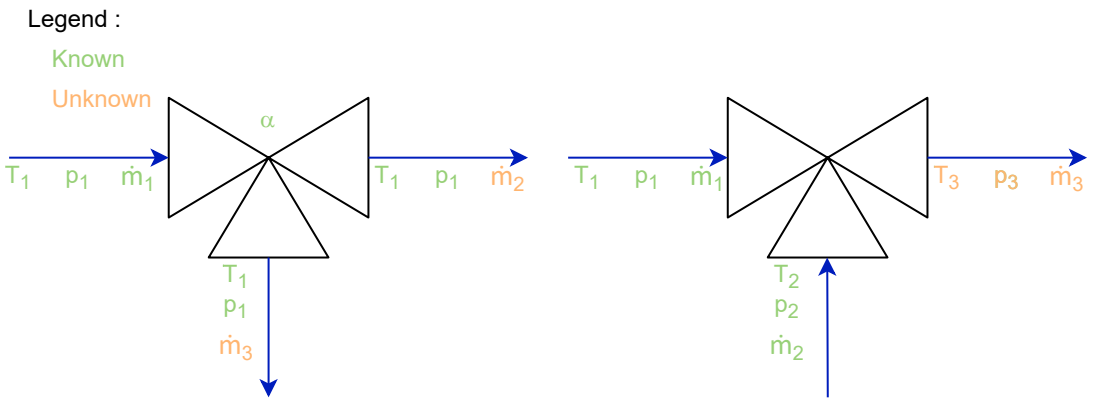

Figure 4.6: Bypass (left) and mixer (right) models.

4.5 Heater

A heater is a device which aims to heat up a specific fluid to a certain target temperature. The required input power is simply obtained by multiplying the mass flow of the fluid with the difference of enthalpies between the inlet and outlet. Again, no pressure loss is assumed.

- Inputs :

Inlet temperature	:	T_i	[K]
Inlet pressure	:	p_i	[kPa]
Mass flow	:	$\dot{m}$	[kg/s]
Wanted temperature	:	T_w	[K]
Composition of the fluid	:	C	[-]

- Calculations :

Inlet enthalpy	:	$h_i = RP(T_i, p_i)$	[J/kg]
Outlet enthalpy	:	$h_o = RP(T_o, p_o)$	[J/kg]

- Outputs :

Power : $P_{heat} = \dot{m} \cdot (h_o - h_i)$ [W]

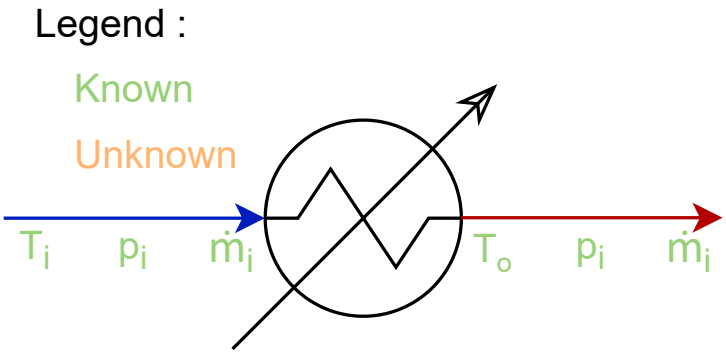

Figure 4.7: Heater model.

4.6 Combustion chamber

A realistic model of a combustion chamber is implemented based on the MATLAB combustion toolbox [49]. This set of functions have been developed by Jan Terpak and Jan Kukurugya from the *Technical University of Kosice* in Slovakia. By specifying the air and fuel compositions as well as the inlet temperatures, pressures and mass flows, the model returns the outlet temperature and the composition of the exhaust gases.

- Inputs :

Inlet temperature of fuel	:	T_1	[K]
Inlet temperature of air	:	T_2	[K]
Inlet pressure of fuel	:	p_1	[kPa]
Inlet pressure of air	:	p_2	[kPa]
Inlet mass flow of fuel	:	$\dot{m}_1$	[kg/s]
Inlet mass flow of air	:	$\dot{m}_2$	[kg/s]
Composition of fuel	:	C_1	[-]
Composition of air	:	C_2	[-]

- Outputs :

Outlet temperature of the waste gas	:	T_3	[K]
Outlet pressure of the waste gas	:	p_3	[kPa]
Outlet composition of the waste gas	:	C_3	[-]

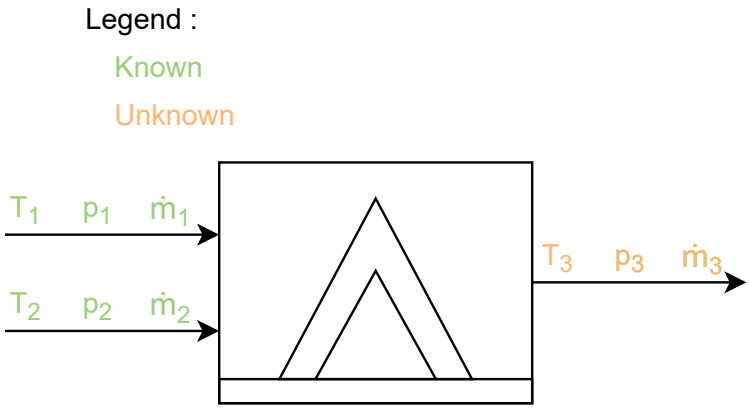

Figure 4.8: Combustion chamber model.

Chapter 5

SOFC system modelling

This chapter is devoted to the analysis of performance of a realistic SOFC system which includes stack, reformer and necessary auxiliaries. The system performance is compared with the performance of a basic stack only coupled with a reformer as presented in Chapter 2.

5.1 Layout

A SOFC system involves a stack, a reformer (internal and/or external), two compressors for the air and fuel, a pump for the water in the case of steam reforming and different heat exchangers/heaters for the input fluids.

Fig. 5.1 shows the layout chosen in this basic SOFC system model. At the cathode side, air flows through a compressor to reach the desired pressure. It is then preheated through a heat exchanger using the exhaust of the SOFC at the cathode side.

At the anode side, the fuel is compressed before being preheated in a heat exchanger. The water is similarly pumped to reach the operating pressure before entering the heat exchanger. The outlet of the SOFC at the anode side is assumed to preheat both fluids.

The SOFC stack should be as close as possible to an isothermal system. In that case, the inlet and outlet temperatures should be equal. This allows to prevent the occurrence of temperature gradients in the electrolyte and consequently the creation and propagation of cracks that could damage the SOFC. In the developed model, the power needed to preheat the fluids is assumed balanced with the heat generated from the reaction (Q_{FC}).

At the outlet of the heaters at the anode side, both fluids cross the ejector and mix in the reformer to reform the fuel.

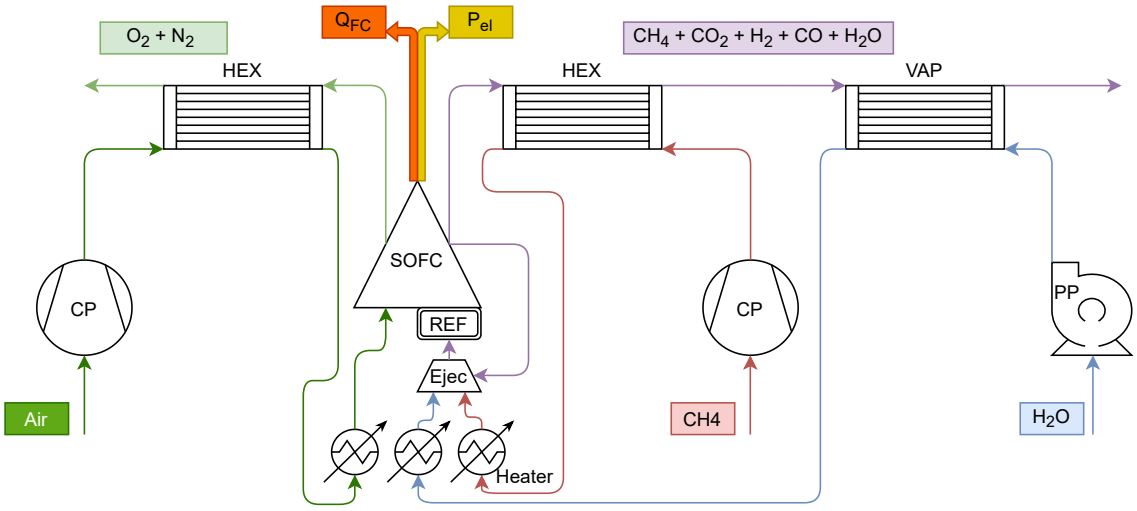

Figure 5.1: SOFC system.

5.2 Results

Efficiency is the sole performance item which is modified in this section while output voltage, electric power density, number of cells and generated heat remain constant. The latter only depends on the stack and reformer in which same parameters have been fixed. Anode gas recirculation is taken into account. The system efficiency shall now account for the auxiliaries consumed power:

$$\eta_{model} = \frac{P_{el} - \sum_{i=1}^{m} \frac{P_{cp,i}}{\eta_{el}}}{\dot{m}_{CH_4} \cdot LHV_{CH_4} + \sum_{j=1}^{n} \frac{P_{heat,j}}{\eta_{el}}} \tag{5.1}$$

A control volume representing the system is shown in Fig. 5.2. The inputs are respectively the fuel power (based on the net heating value of methane (LHV_{CH_4})) and the heating power required by the heaters (P_{heat}). This power is actually increased using an electrical efficiency (η_{el}). The power of the compressors (P_{cp}) is assumed to reduce the electric power delivered by the SOFC (P_{el}) and therefore appears at the numerator of the definition 5.1. An alternative could have been to add the compressor power to the denominator. Again, an electrical efficiency is used for the compressor consumed power. The electrical efficiency is assumed to be 0.9.

Fig 5.3 shows a comparison between the efficiency of the SOFC stack and system. As expected, the efficiency of the system is lower than the efficiency of the stack. The system efficiency curve seems to have a kink at low current densities. This behavior is explained in the next section.

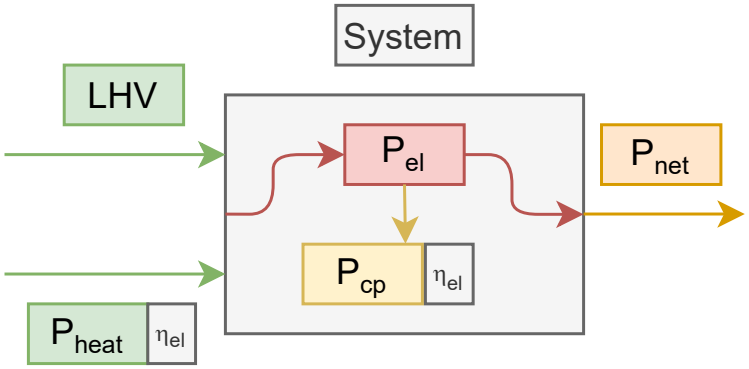

Figure 5.2: Efficiency of the system representation.

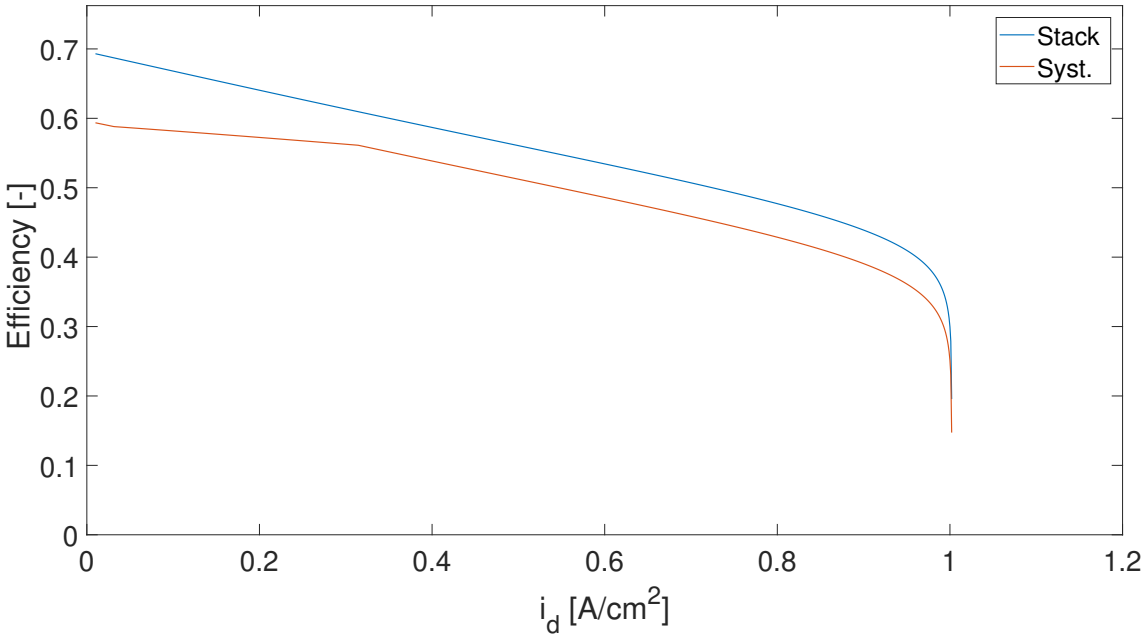

Figure 5.3: Efficiency of the stack and system [-] as a function of the current density [A/cm²]. ($R_R = 0.7$ [-], $T = 1173.15$ [K], $p_t = 200$ [kPa], $U_f = 0.7$ [-], $\lambda = 1.5$ [-], $\dot{m}_{CH_4} = 3.4\text{E-}4$ [kg/s], $\dot{m}_{H_2O,NR} = 8.1\text{E-}5$ [kg/s]).

5.3 Heat management

In order to understand the particular shape of the system efficiency curve in Fig. 5.3, there is a need to return to the fundamentals of the fuel cell. As seen in the energy conservation in the fuel cell, heat is released due to exothermic reaction. This heat must be extracted to ensure an isothermal stack. Several ways are possible to accomplish this. On one hand, a cooling system can be integrated with the stack to evacuate all that heat. However, it increases its complexity further complicated by the high temperature. On the other hand, another solution is to use the released heat in a heat exchanger integrated to the SOFC in order to allow the reactants (air, methane and water) to be heated until they reach the operating temperature. This is the approach assumed in this work [54].

At each current density corresponds a value of the generated heat Q_{FC} (Fig. 2.6). This generated heat shall be compared with the required powers of the three

heaters (air, methane and water). Two cases should be considered as illustrated in Table 5.1.

Let us define the total power required by the heaters:

$$P_{heat,tot} = \sum_{j=1}^{n} \frac{P_{heat,j}}{\eta_{el}} \tag{5.2}$$

Case 1 :	**Case 2 :**
$Q_{FC} < P_{heat,tot}$	$Q_{FC} > P_{heat,tot}$
$P_{heat} = P_{heat,tot} - Q_{FC}$	$P_{heat} = 0$

Table 5.1: Heating distribution.

with P_{heat} the residual powers to be provided to the heaters.

Going back to Fig. 5.3, both cases are represented. Indeed, a current density of 0 [A/cm^2] until around 0.32 [A/cm^2] corresponds to case one, while the rest of the curve corresponds to case 2. In the latter, the only loss is due to the compressors. As it is constant, the shape of the system curve is the same as the stack curve but shifted below.

5.4 SOFC system performance analysis

This section analyzes the influence of three parameters on the SOFC system performance (electric power density, stack and system efficiencies) : temperature, pressure and air excess.

5.4.1 Temperature

Electric power similarly behaves to the stack case depending on temperature (see Section 2.6.1). The higher the temperature, the higher the electric power density. Nevertheless, the maximum value at 1373.15 K appears lower than in the stack case. This is an effect of the recirculation which influences the gas composition at the anode inlet.

As far as the efficiencies are concerned, except at lower current densities, a higher temperature always benefits. This lower current densities exception is due to the number of cells that are higher for lower temperatures as seen in Fig. D.2.

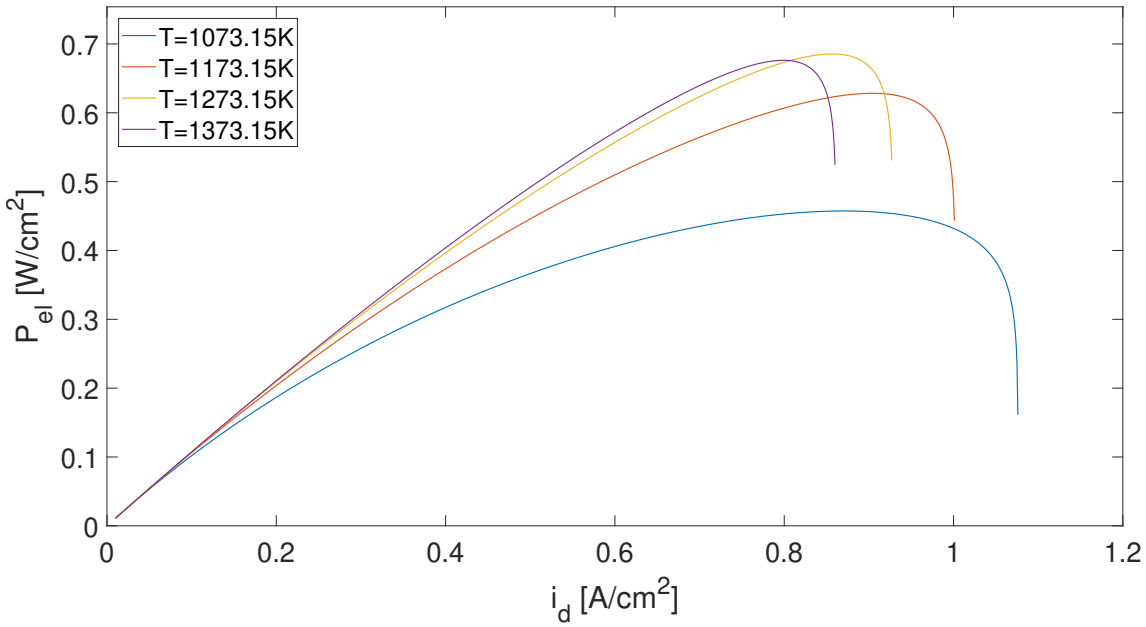

Figure 5.4: Electric power density [W/cm²] as a function of the current density [A/cm²] for different temperatures. ($R_R = 0.7$ [-], $p_t = 200$ [kPa], $U_f = 0.7$ [-], $\lambda = 1.5$ [-], $\dot{m}_{CH_4} = 3.4\text{E-}4$ [kg/s], $\dot{m}_{H_2O,NR} = 8.1\text{E-}5$ [kg/s]).

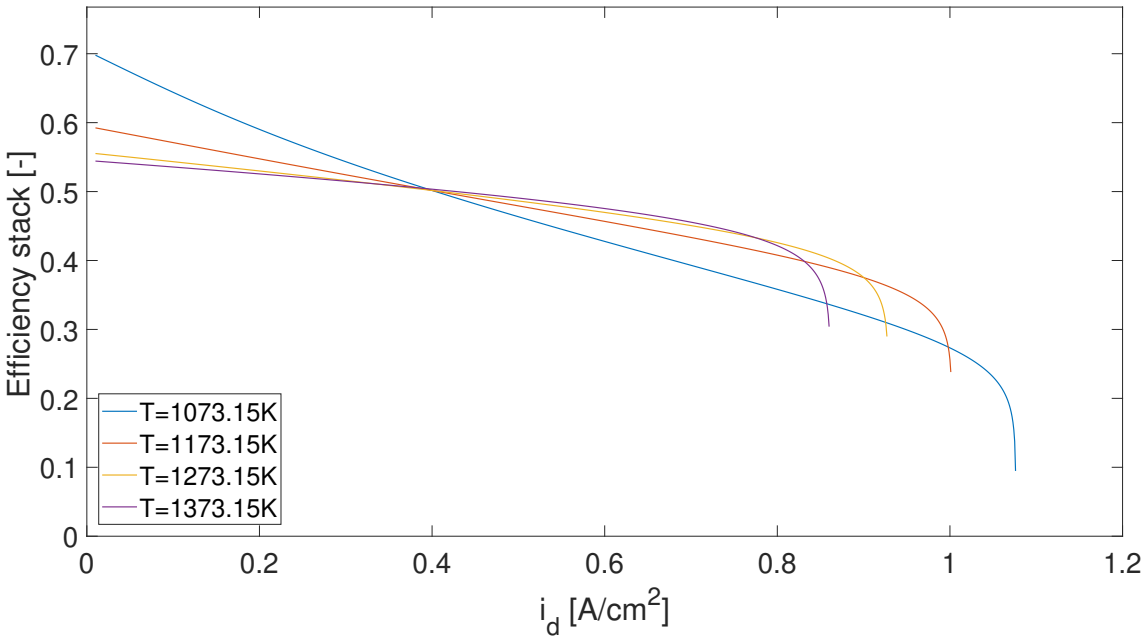

Figure 5.5: Efficiency of the stack [-] as a function of the current density [A/cm²] for different temperatures. ($R_R = 0.7$ [-], $p_t = 200$ [kPa], $U_f = 0.7$ [-], $\lambda = 1.5$ [-], $\dot{m}_{CH_4} = 3.4\text{E-}4$ [kg/s], $\dot{m}_{H_2O,NR} = 8.1\text{E-}5$ [kg/s]).

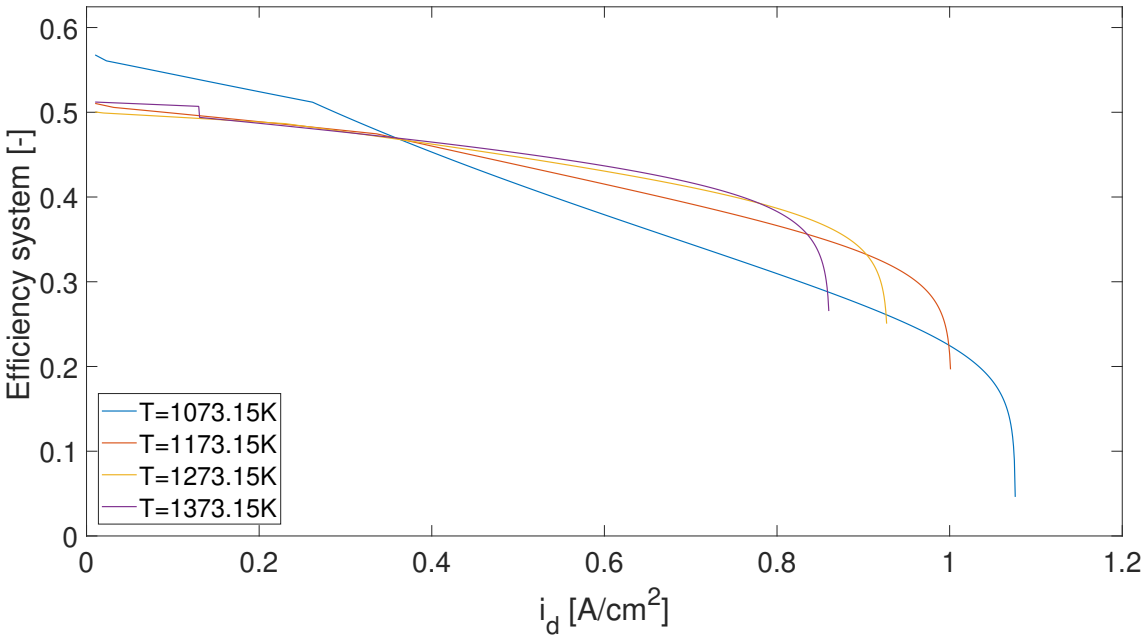

Figure 5.6: Efficiency of the system [-] as a function of the current density [A/cm²] for different temperatures. (R_R = 0.7 [-], p_t = 200 [kPa], U_f = 0.7 [-], λ = 1.5 [-], $\dot{m}_{CH_4}$ = 3.4E-4 [kg/s], $\dot{m}_{H_2O,NR}$ = 8.1E-5 [kg/s]).

5.4.2 Pressure

The pressure is a more critical parameter. For the power density, as expected, it increases with an increasing pressure. For the efficiencies, again, it depends on the current density in the SOFC stack.

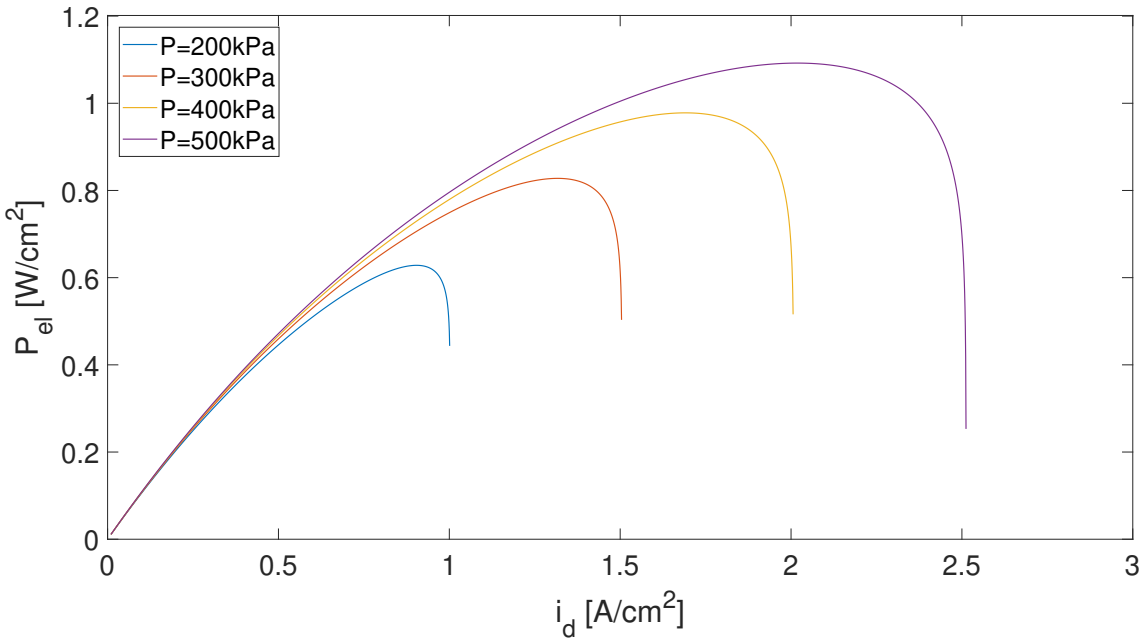

Figure 5.7: Electric power density [W/cm²] as a function of the current density [A/cm²] for different pressures. (R_R = 0.7 [-], T = 1173.15 [K], U_f = 0.7 [-], λ = 1.5 [-], $\dot{m}_{CH_4}$ = 3.4E-4 [kg/s], $\dot{m}_{H_2O,NR}$ = 8.1E-5 [kg/s]).

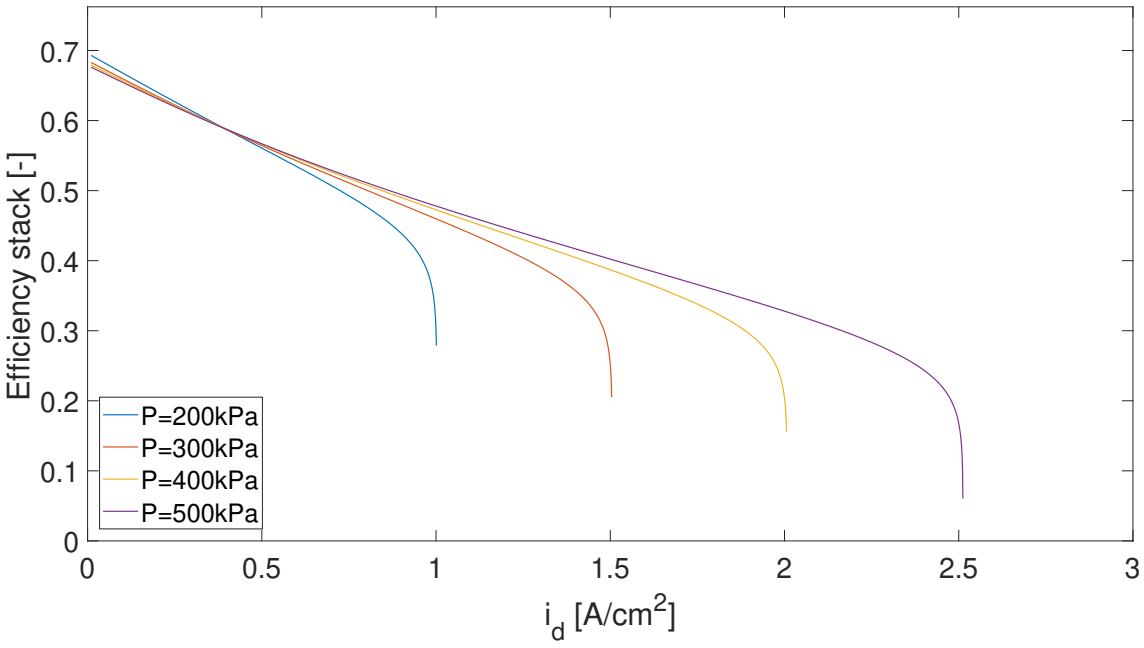

Figure 5.8: Efficiency of the stack [-] as a function of the current density [A/cm²] for different pressures. (R_R = 0.7 [-], T = 1173.15 [K], U_f = 0.7 [-], λ = 1.5 [-], $\dot{m}_{CH_4}$ = 3.4E-4 [kg/s], $\dot{m}_{H_2O,NR}$ = 8.1E-5 [kg/s]).

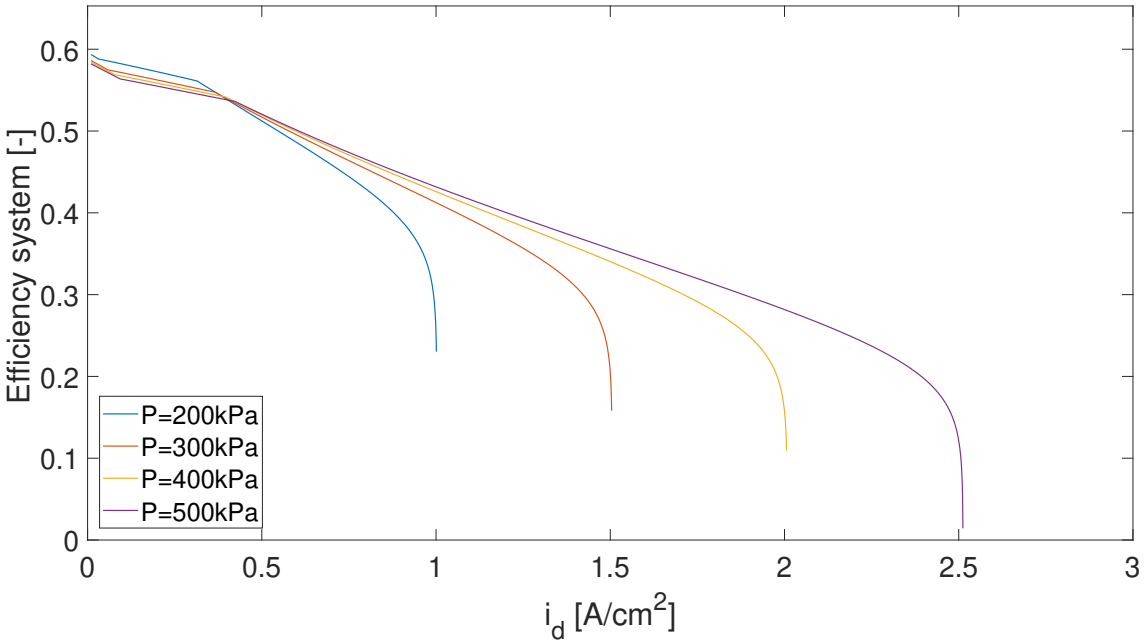

Figure 5.9: Efficiency of the system [-] as a function of the current density [A/cm²] for different pressures. (R_R = 0.7 [-], T = 1173.15 [K], U_f = 0.7 [-], λ = 1.5 [-], $\dot{m}_{CH_4}$ = 3.4E-4 [kg/s], $\dot{m}_{H_2O,NR}$ = 8.1E-5 [kg/s]).

5.4.3 Excess air

The electric power density and the efficiency of the stack are likely sensitive to air excess.

Nevertheless, as shown in Fig. 5.12, increasing the air excess increases the work of the compressor and decreases the system efficiency.

The total compressed air should therefore correspond to the minimum mass flow required by the stack so that the work of the compressor impacts as low as possible the system efficiency.

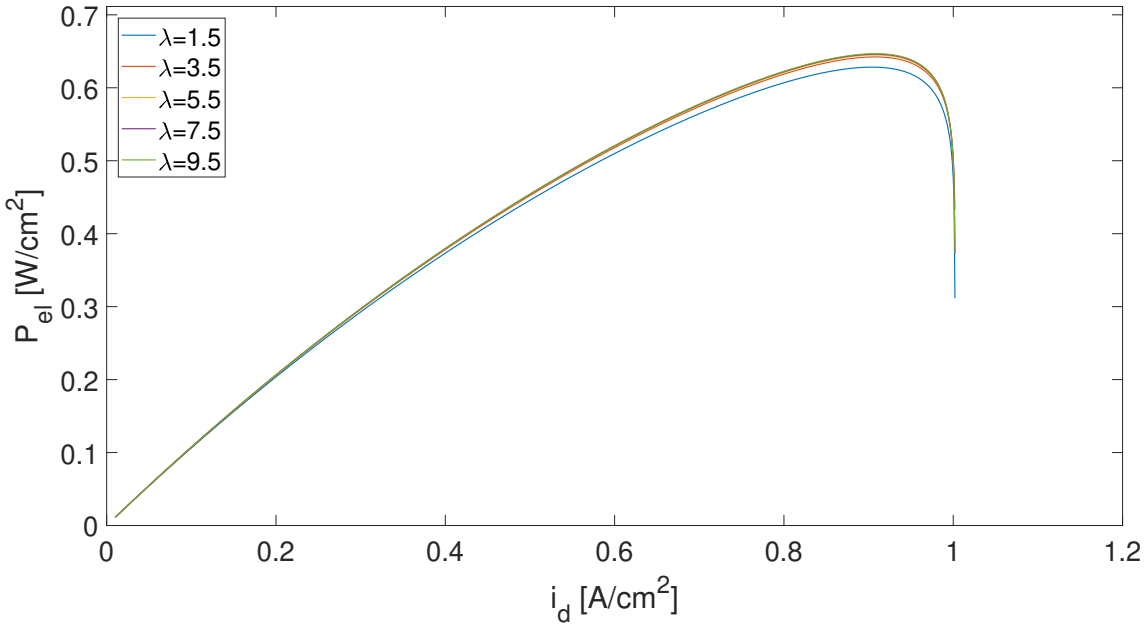

Figure 5.10: Electric power density [W/cm²] as a function of the current density [A/cm²] for different air excesses. (R_R = 0.7 [-], T = 1173.15 [K], p_t = 200 [kPa], U_f = 0.7 [-], $\dot{m}_{CH_4}$ = 3.4E-4 [kg/s], $\dot{m}_{H_2O,NR}$ = 8.1E-5 [kg/s]).

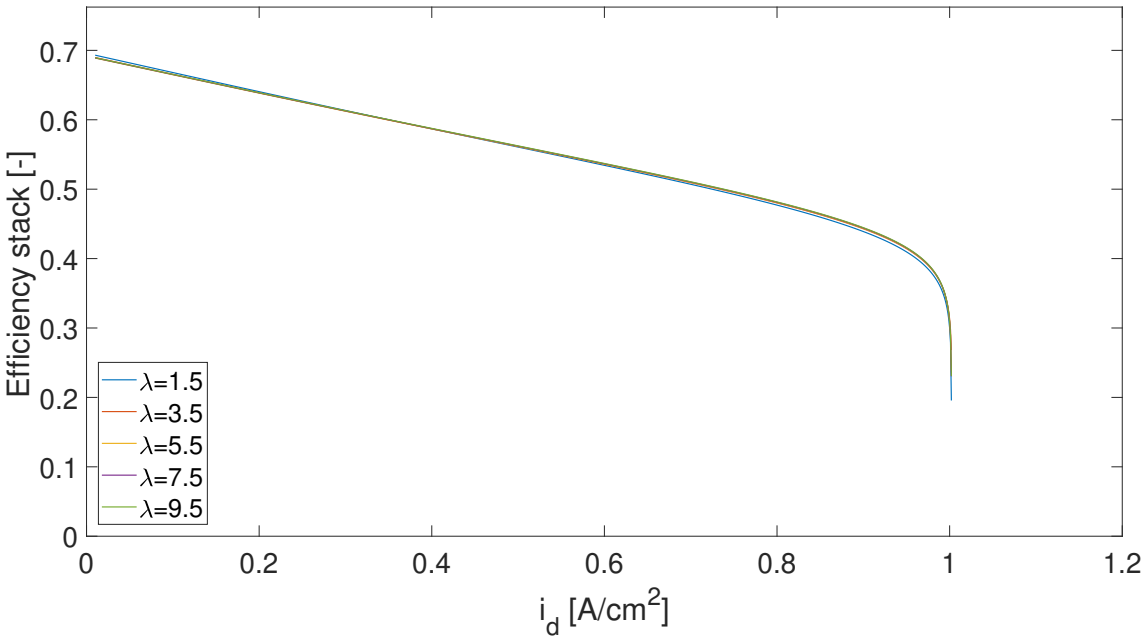

Figure 5.11: Efficiency of the stack [-] as a function of the current density [A/cm²] for different air excesses. (R_R = 0.7 [-], T = 1173.15 [K], p_t = 200 [kPa], U_f = 0.7 [-], $\dot{m}_{CH_4}$ = 3.4E-4 [kg/s], $\dot{m}_{H_2O,NR}$ = 8.1E-5 [kg/s]).

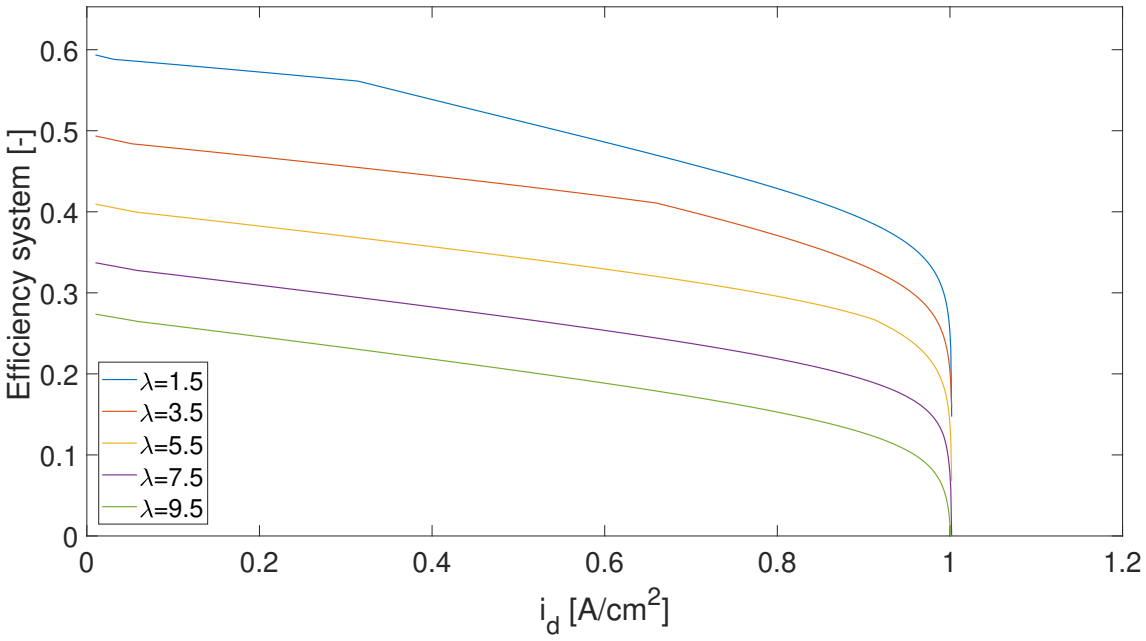

Figure 5.12: Efficiency of the system [-] as a function of the current density [A/cm²] for different air excesses. ($R_R = 0.7$ [-], $T = 1173.15$ [K], $p_t = 200$ [kPa], $U_f = 0.7$ [-], $\dot{m}_{CH_4} = 3.4\text{E-}4$ [kg/s], $\dot{m}_{H_2O,NR} = 8.1\text{E-}5$ [kg/s]).

Chapter 6

SOFC-GT modelling

As seen in Section 5.4.3, the compressor negatively impacts the system efficiency with increasing air excess. A turbine exploiting the hot pressurized exhaust gas of the SOFC is a natural way to produce mechanical power to counterbalance the power required by the compressors, similarly to a turbocharger.

Most gas turbine cycles involve at least a compressor, a turbine, a combustion chamber and possibly a recuperator to preheat the combustion air by recovering turbine exhaust energy. Connecting such a system to the SOFC allows to, on one hand, reduce the power of the compressor with respect to the basic configuration and on the other hand to burn the remaining fuel which did not react in the SOFC since the fuel utilization (U_f) is never equal to 1. This connection is analyzed in details in this chapter.

6.1 Definitions

6.1.1 Efficiency

The system efficiency definition is based on Eq. 5.1 from Section 5.2. The power of the turbine should now be taken into account to counterbalance the power of the compressor(s). A mechanical efficiency (η_m) is introduced to account for the losses in shaft and bearings. The remaining part of the turbine power is converted into electricity through a generator with a given electrical efficiency.

$$\eta_{model} = \frac{P_{el} + \left[\sum_{l=1}^{o} P_{tu,l} - \sum_{i=1}^{m} \frac{P_{cp,i}}{\eta_m}\right] \cdot \eta_{el}}{\dot{m}_{CH_4} \cdot LHV_{CH_4} + \sum_{j=1}^{n} \frac{P_{heat,j}}{\eta_{el}}} \tag{6.1}$$

The electrical and mechanical efficiencies are assumed constant and given in the following table.

Efficiency	Mechanical	Electrical
Value	0.98	0.9

Table 6.1: Assumed constants for the mechanical and electrical efficiencies.

6.1.2 Temperature limit

In a gas turbine cycle, the turbine inlet temperature is usually limited to prevent material damage. This mechanism is achieved by sufficient air excess since increasing the air excess decreases the outlet temperature of the combustion chamber. A large air excess is detrimental to the efficiency while the stack efficiency itself does not vary much with air excess (see Section 5.4.3). A larger mass flow yields larger turbo-machinery components further impacting the mass.

In Section 3.3, one advantage of fuel recirculation is to decrease the outlet temperature of the combustion chamber. Indeed, the recirculation reduces the outlet flow at the anode and therefore the fuel entering the combustion chamber.

Fig. 6.1 shows the evolution of the outlet temperature of the combustion chamber with respect to air excess (λ) and recirculation ratio (R_R) (see Section 3.3). Fixed cycle parameters are the following:

Inlet air temperature	:	1173.15	[K]
Inlet fuel temperature	:	973.15	[K]
Total fuel mass flow	:	4.5242E-4	[kg/s]

Fig. 6.1 shows that a combination of recirculation and air excess reduces significantly the outlet temperature of the combustion chamber.

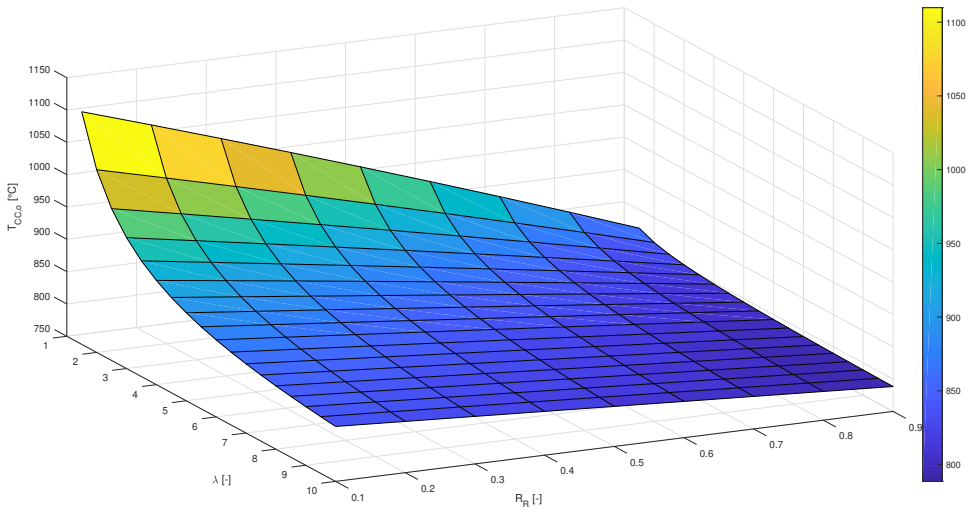

Figure 6.1: Outlet temperature [°C] as a function of the air excess [-] and the recirculation ratio [-].

Two simulations are performed to compare the impact of the recirculation ratio on the system. Table 6.2 shows the required air excess to obtain a temperature lower than 950°C at the inlet of the gas turbine with and without recirculation.

No recirculation		Recirculation	
Temperature [°C]	Air excess [-]	Temperature [°C]	Air excess [-]
949.33	15	947	4.5

Table 6.2: Air excess to obtain a temperature lower than 950°C with and without recirculation (T = 1173.15 [K], p_t = 200 [kPa], U_f = 0.7 [-], $\dot{m}_{CH_4}$ = 3.2E-4 [kg/s], $\dot{m}_{H_2O,NR}$ = 4.95E-4 [kg/s]).

The conclusion is that the recirculation allows to drastically reduce the air excess required to have a suitable turbine inlet temperature. It also allows to decrease the mass flow of reforming fuel. Therefore, the subsequent studied configurations all include recirculation.

6.2 Basic configuration

The basic configuration of the SOFC-GT system involves the SOFC system with a combustion chamber and a turbine (Fig. 6.2). Exhaust gas from the anode and cathode are injected in the combustion chamber and combustion exhaust goes into the turbine.

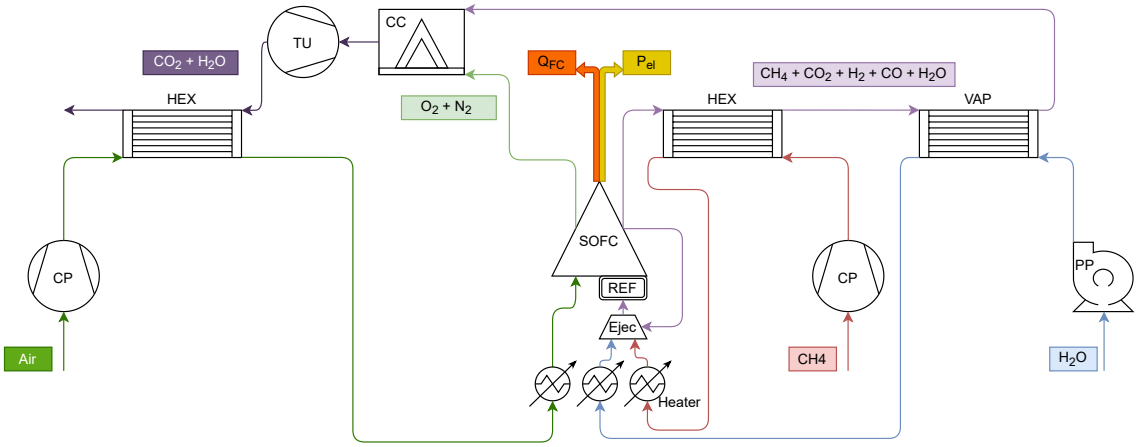

Figure 6.2: Basic configuration of the SOFC-GT system.

Table 6.3 shows the power required to compress the air, the fuel and the water and the power delivered by the turbine. It can be seen that the turbine allows to compensate the power of the compressor with a positive impact on efficiency. The remaining part of the power is connected to a generator converting the mechanical power into electrical power.

Compressors			Turbine
Air	Fuel	Water	Gas
2.311E3	24.0445	0.012	2.6826E3

Table 6.3: Power [W] required by the air, fuel and water compressors and power delivered by the turbine (R_R = 0.7 [-], T = 1173.15 [K], p_t = 200 [kPa], λ = 4.5 [-], U_f = 0.7 [-], $\dot{m}_{CH_4}$ = 3.3712E-4 [kg/s], $\dot{m}_{H_2O,NR}$ = 8.1E-5 [kg/s])

Fig. 6.3 shows the efficiency of the stack and the SOFC system as a function of the current density. A large air ratio of 4.5 is required to limit the turbine inlet temperature to 950°C. The efficiency of the system mostly remains lower than the efficiency of the stack except at high current density where some electric power is recovered by the generator.

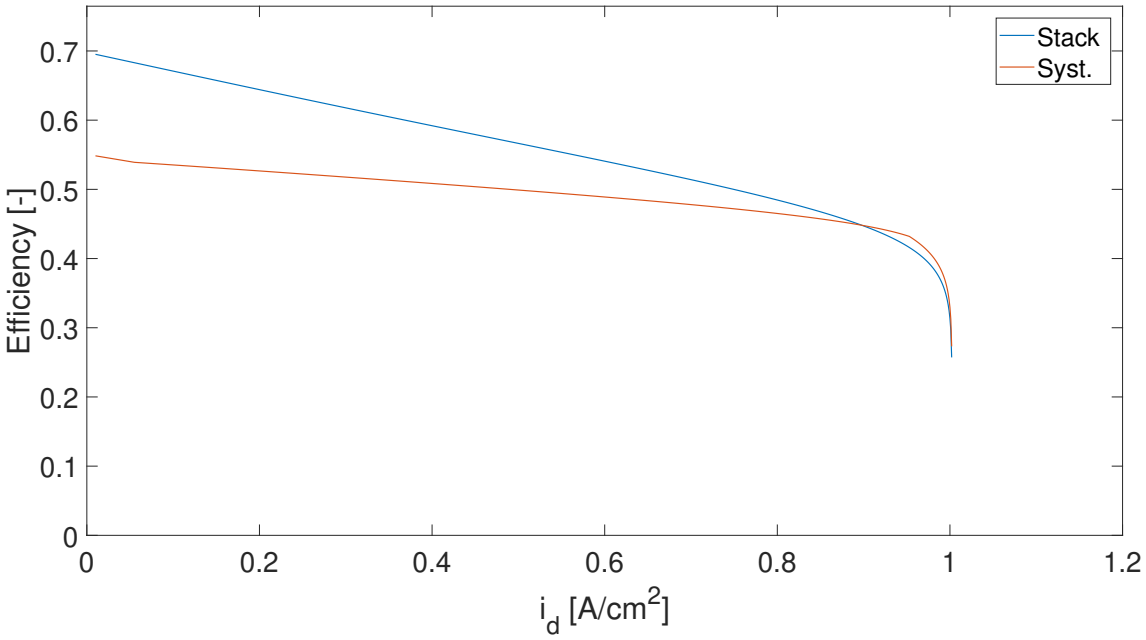

Figure 6.3: Efficiency of the stack and the SOFC system as a function of the current density ($R_R = 0.7$ [-], $T = 1173.15$ [K], $p_t = 200$ [kPa], $\lambda = 4.5$ [-], $U_f = 0.7$ [-], $\dot{m}_{CH_4} = 3.3712\text{E-}4$ [kg/s], $\dot{m}_{H_2O,NR} = 8.1\text{E-}5$ [kg/s]).

6.3 Bypass configuration

In the second configuration, we introduce a bypass to limit the amount of air entering the SOFC to the minimum required. It is beneficial in two ways. On one hand, it reduces the mass flow of air entering the cathode and on the other hand, the temperature of the air entering the combustion chamber is reduced since it is not further heated by the SOFC.

Two possible locations exist for the bypass. The first one is to locate it after the air heat exchanger as shown in Fig. 6.4.

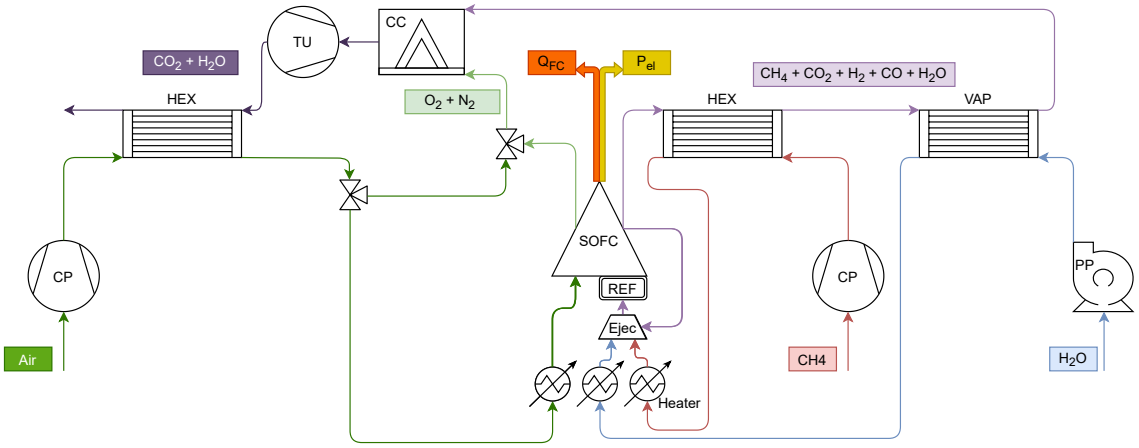

Figure 6.4: First possibility of the bypass configuration.

The second one is to location the bypass before the heat exchanger as shown in Fig. 6.5.

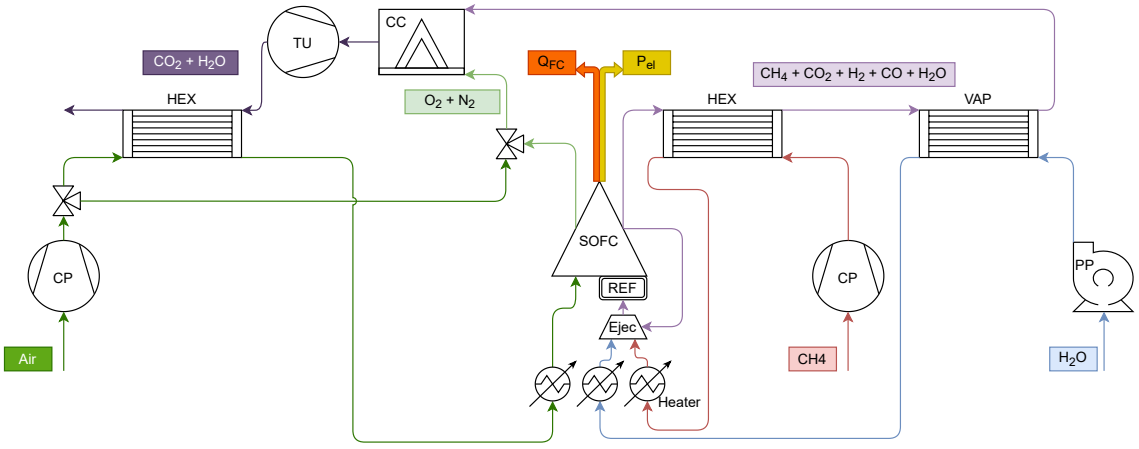

Figure 6.5: Second possibility of the bypass configuration.

The first option does not yield satisfactory results. Indeed, the difference in temperature between the outlet of the heat exchanger and the outlet of the cathode (in the mixer) is too small to have a significant impact on the reduction of the outlet combustor air temperature. Air excess is therefore not reduced with respect to the basic configuration.

The second option is more promising because the mixing happens between both fluids with a larger temperature difference. Fig. 6.6 shows all the intermediate temperatures between the components of the system, obtained with a total air excess of 1.8 of which 83.33% enters the cathode.

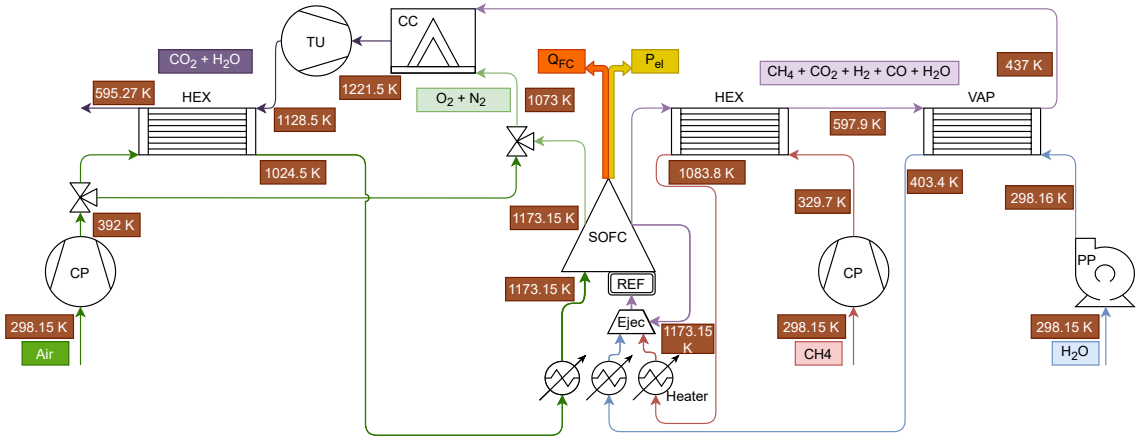

Figure 6.6: Second possibility of the bypass configuration with the intermediate temperatures ($R_R = 0.7$ [-], $T = 1173.15$ [K], $p_t = 200$ [kPa], $\lambda = 1.8$ [-], $U_f = 0.7$ [-], $\dot{m}_{CH_4} = 3.4\text{E-}4$ [kg/s], $\dot{m}_{H_2O,NR} = 8.1\text{E-}5$ [kg/s]).

Fig. 6.7 shows the efficiency of the stack and the system as a function of the current density. Around a current density of 0.4 [A/cm²], the generated heat by the exothermic reaction compensates the power of the heaters. By adding the electric power recovered from the turbine, the efficiency of the system becomes higher than that of the stack.

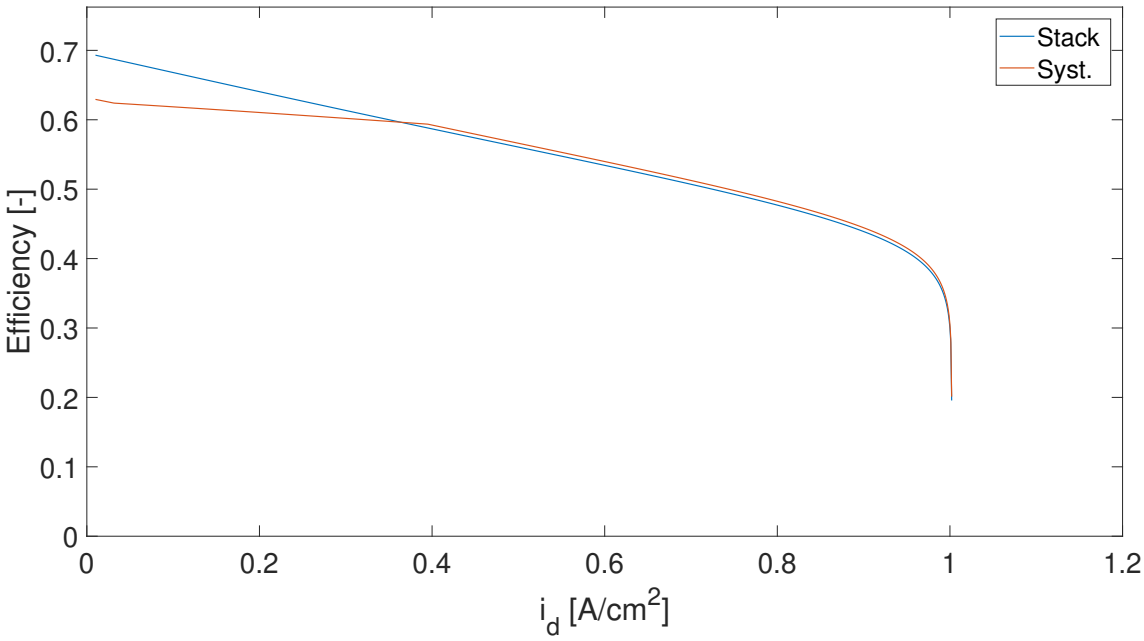

Figure 6.7: Efficiency of the stack and the system as a function of the current density ($R_R = 0.7$ [-], $T = 1173.15$ [K], $p_t = 200$ [kPa], $\lambda = 1.8$ [-], $U_f = 0.7$ [-], $\dot{m}_{CH_4} = 3.4\text{E-}4$ [kg/s], $\dot{m}_{H_2O,NR} = 8.1\text{E-}5$ [kg/s]).

6.4 Combustion chamber coupled heat exchanger configuration

To further reduce the air excess entering the SOFC, this new configuration includes a heat exchanger directly embedded in the combustion chamber, following a suggestion by Delanaye [27].

This configuration is beneficial in two ways. On one hand, the air is assumed preheated at the temperature of the stack. The generated heat by the anodic reaction then only heats up water and methane. On the other hand, the temperature at the outlet of the combustion chamber is reduced because of the heat extracted from the waste gases. This allows to obtain a suitable inlet turbine temperature (less than 950°C) with a lower air excess.

Fig. 6.8 shows the schema of the configuration.

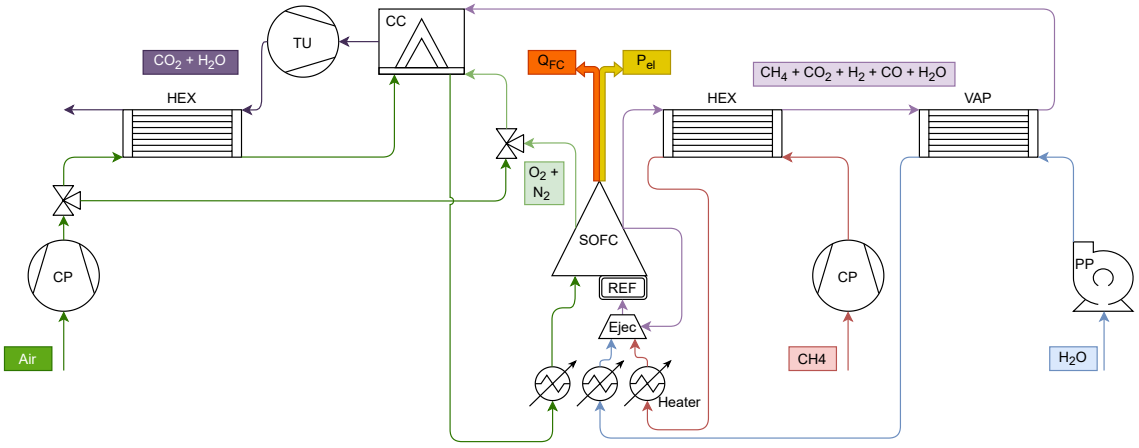

Figure 6.8: Third configuration of the SOFC-GT system.

Fig. 6.9 shows the efficiency of the stack and the system as a function of the current density. With this configuration, the required total air excess is reduced to 1.6. The system efficiency curve jumps above the stack efficiency curve at lower current densities.

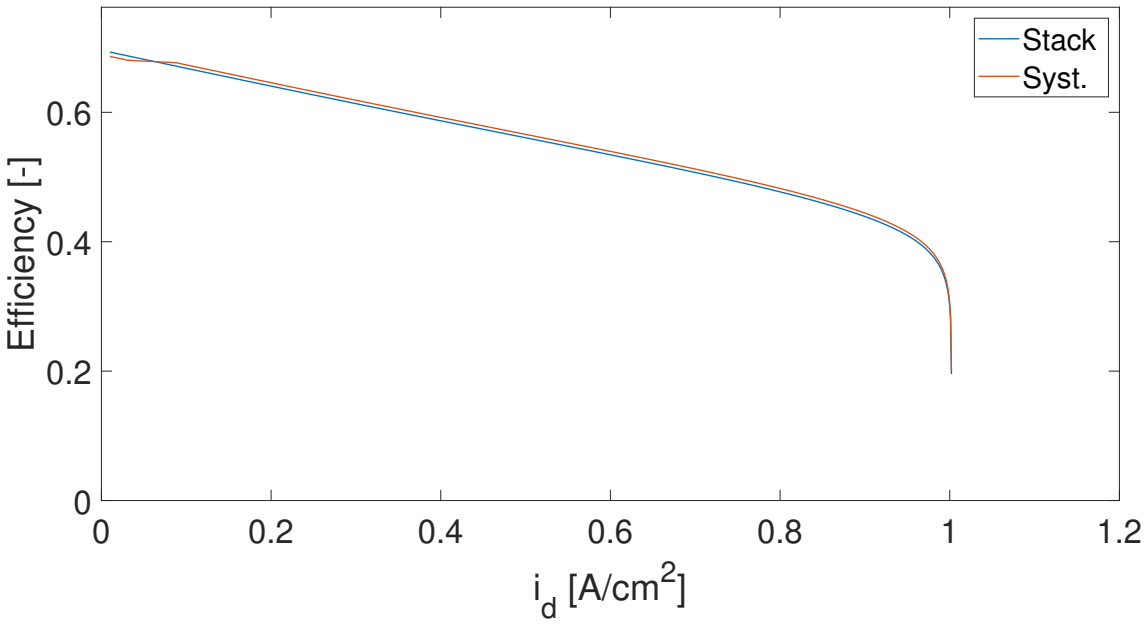

Figure 6.9: Efficiency of the stack and the system as a function of the current density (R_R = 0.7 [-], T = 1173.15 [K], p_t = 200 [kPa], λ = 1.6 [-], U_f = 0.7 [-], $\dot{m}_{CH_4}$ = 3.4E-4 [kg/s], $\dot{m}_{H_2O,NR}$ = 8.1E-5 [kg/s]).

6.5 Intercooled compressor stages configuration

The last investigated system improvement concerns the reduction of compressor input power to increase the efficiency, through a two stage intercooled compressor system for the air supply (Fig. 6.10). In this configuration, a bypass is also added.

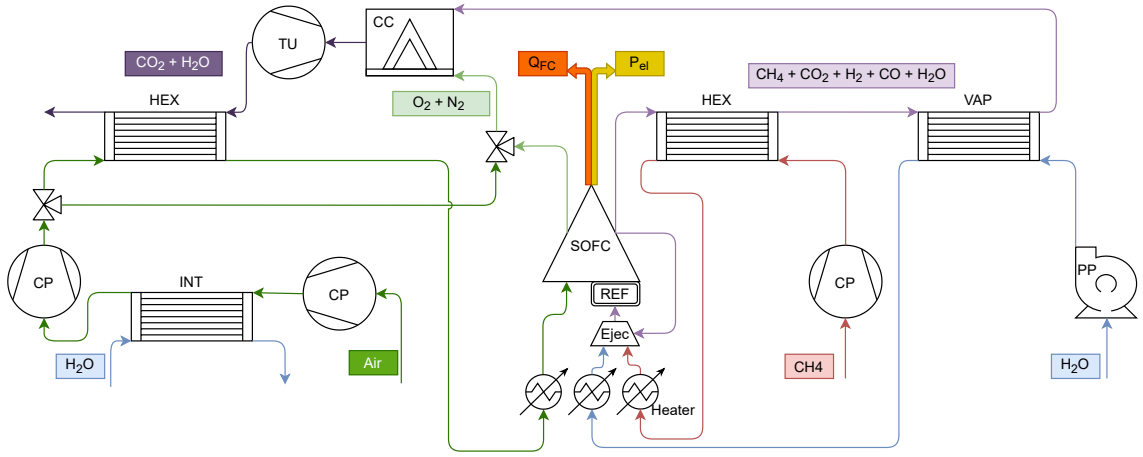

Figure 6.10: Fourth configuration of the SOFC-GT system.

The intercooler is a heat exchanger in which compressed air is cooled by another fluid. Different fluids are tested to validate this model. The first idea is to recover the energy from the compressed air by heating the reforming water or methane fuel. Both cases do not yield useful results because of the low mass flow of methane (3.4E-4 kg/s) and especially of water (8.1E-5 kg/s). The second idea is to have an external water circuit whose temperature increases from 40°C until 90°C from the

inlet until the outlet of the intercooler. This water circuit is then redirected in other systems such as a heat pump for example. This is the case considered here in Fig. 6.10.

One may ask if it is worth the cost to further increase the complexity of an already complex system. Fig. 6.11 shows the power of the compressor system (one compressor or two) as a function of the operating pressure in the stack. As expected, the power of the intercooled system is lower than the power with a single compressor. At low pressures, it is not the case because of the additional pressure losses in the intercooler.

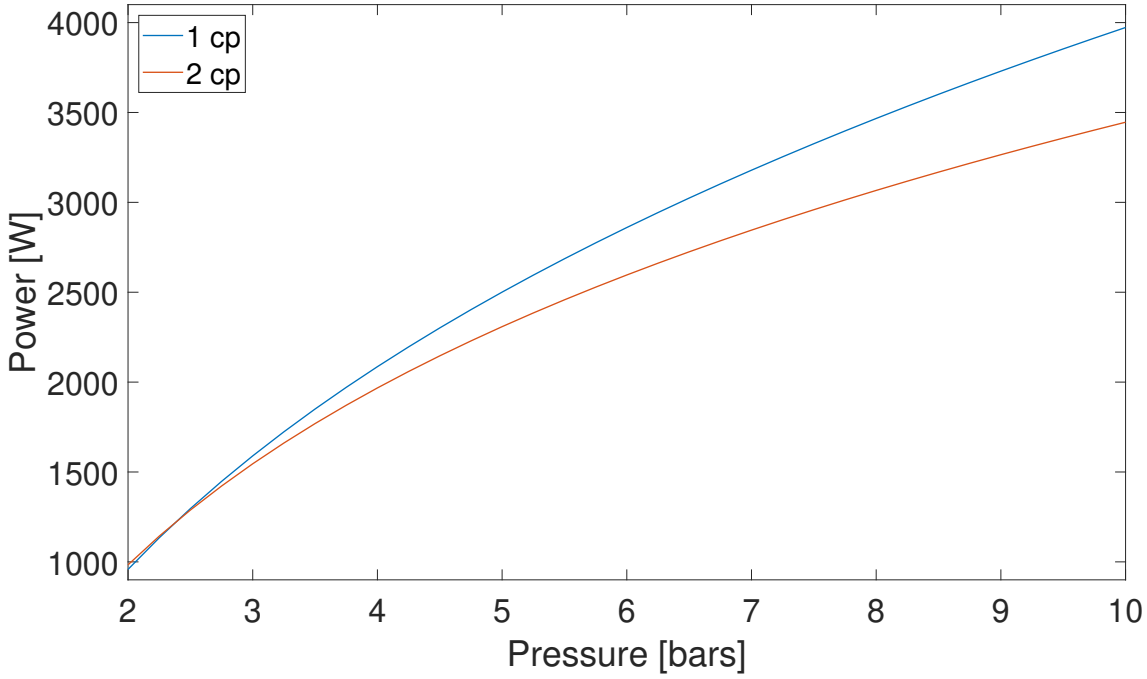

Figure 6.11: Power of the compressor(s) in the case of one compressor and two compressors as a function of the pressure in the SOFC. ($\dot{m}_{air}$ = 1E-2 [kg/s])

Increasing the pressure increases the complexity of the system because of sealings, materials, etc. Adding a second compressor, a heat exchanger and a water circuit increases weight and space. However, as presented in Section 2.6.2, increasing pressure can be interesting to reduce the size of the stack for a given power and efficiency. The decision of commercializing this configuration results of a trade off between the benefit of reducing the compressor powers on the one hand and the complexity and space limitation on the other hand.

Chapter 7

Technological study

This chapter introduces a technological study focused on mass analysis of the SOFC-GT system. The mass of all configurations described in Chapter 6 are quantified for an electric power output of 1, 10 and 20 [kW] at a current density of 0.4 [A/cm^2].

7.1 Component mass relations

7.1.1 SOFC stack mass

A SOFC system involves one or more stacks each of them made of a number of cells and a casing. The mass of the SOFC is affected by the arrangement of the cells and the stacks. Assabumrungrat et al. [3] analyze various configurations of stack arrangements (Fig. 7.1) and conclude that the basic configuration (one stack) gives the best efficiency for a given power. Therefore, in this study, we limit ourselves to a single stack SOFC system.

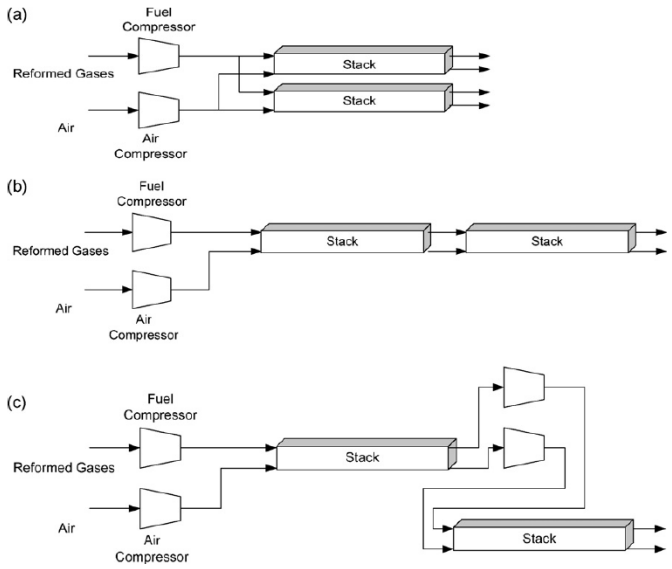

Figure 7.1: Different configurations of stack arrangement. [3]

In order to estimate the SOFC mass, we adopt a basic approach which consists in a linear relation between the mass and the number of cells. This assumes that cells have the same area for each configuration. Hence, the datasheets ([33] [53]

[62]) of three commercialized products with similar cell area have been analyzed. It follows a linear relationship between the mass and the number of cells as:

$$M_{SOFC} = M_{SOFC,0} \cdot \frac{N_{cells}}{N_{cells,0}} + M_{casing} \tag{7.1}$$

with,

$$\begin{array}{lcll} M_{SOFC,0} & = & 4 & [\text{kg}] \\ M_{casing} & = & 5 & [\text{kg}] \\ N_{cells,0} & = & 30 & [\text{-}] \end{array}$$

7.1.2 Turbocharger

The turbocharger mass quantification is based on the analysis performed by Bou Nader et al. [10], who relate the mass flow of fluid (kg/h) with the power to weight ratio (kW/kg) by the following relation:

$$\dot{m}_{TC} = -275 \cdot \left(\frac{P_{TC}}{M_{TC}}\right)^2 + 645 \cdot \left(\frac{P_{TC}}{M_{TC}}\right) + 122 \tag{7.2}$$

where the power (P_{TC}) corresponds to the fraction of the turbine power that compensates the power of the compressor(s).

The generator mass connected to the turbine can be quantified as a function of the mechanical power to convert. The reference power to weight ratio (PM_{gen}) is equal to 3000 W/kg. The generated power (P_{gen}) corresponds to the difference between the turbine power and the compressor(s) power.

$$M_{gen} = \frac{P_{gen}}{PM_{gen}} \tag{7.3}$$

7.1.3 Combustion chamber

Following again the description in Bou Nader et al. [10], the mass of the combustion chamber depends on the mass flow at the inlet as well as the fuel power (Q_{CC}) by:

$$Q_{CC} = \dot{m}_{fuel} \cdot LHV_{fuel} \tag{7.4}$$

The reference taken here is the combustion chamber of MITIS [51]. The mass flow of air ($\dot{m}_{air,0}$) is equal to 0.140 kg/s, the mass flow of fuel ($\dot{m}_{fuel,0}$) is equal to 9.5E-4 kg/s and the mass ($M_{CC,0}$) is equal to 17 kg.

$$M_{CC} = M_{CC,0} \cdot \frac{\dot{m}_{air} + \dot{m}_{fuel}}{\dot{m}_{air,0} + \dot{m}_{fuel,0}} \cdot \frac{Q_{CC}}{Q_{CC,0}} \tag{7.5}$$

with,

$$Q_{CC,0} = \dot{m}_{fuel,0} \cdot LHV_{fuel} \tag{7.6}$$

7.1.4 Heat exchanger

The heat exhanger mass is based on the largest mass flow stream and its efficiency. The reference is the heat exchanger of MITIS [51]. Its mass is around 80 kg ($M_{HEX,0}$) with a mass flow of air ($\dot{m}_{HEX,0}$) of 0.140 kg/s and an efficiency ($\eta_{HEX,0}$) of 0.87.

$$M_{HEX} = M_{HEX,0} \cdot \frac{\dot{m}_{HEX}}{\dot{m}_{HEX,0}} \cdot \frac{\eta_{HEX,0}}{\eta_{HEX}}$$

7.1.5 Piping and power electronics

A 10 kg of mass is added to the total mass to take into account the piping and power electronics as well as other subsystems such as filters, valves, etc.

7.2 Comparison

The mass of different SOFC-GT configurations is compared for three powers (1 kw, 10 kw and 20 kW) in Fig. 7.2.

In all configurations, the SOFC stack accounts for most of the total mass of the system. Reducing the air excess with respect to the basic configuration (a) in configurations (b), (c) and (d) decreases the power of the heat exchanger and the turbocharger and therefore decreases the mass of the system.

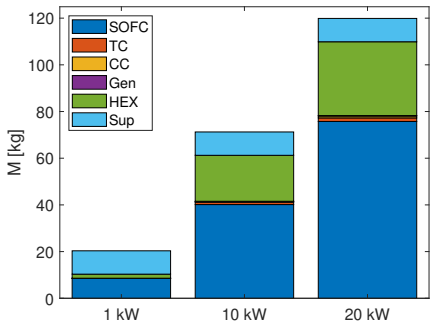

(a) Basic configuration.

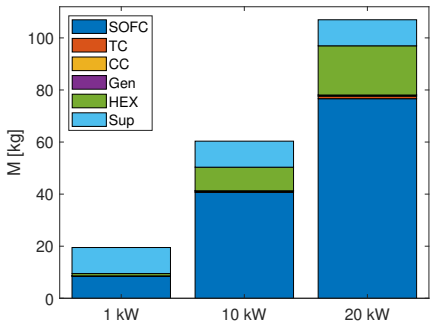

(b) Bypass configuration.

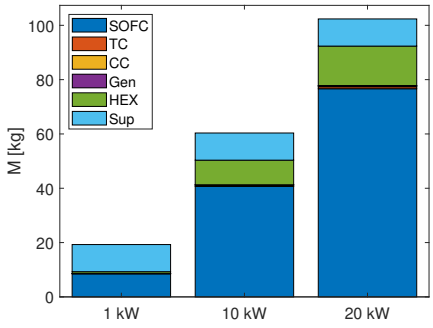

(c) CC heat exchanger configuration.

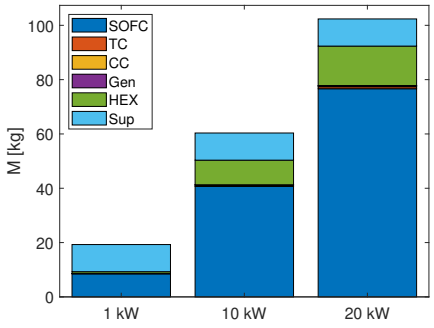

(d) Intercooled compressing system.

Figure 7.2: Mass for 1 kW, 10 kW and 20 kW for the configurations seen (Chapter 6).

Chapter 8

Conclusion and perspectives

In this thesis, we have described several layouts of solid oxide fuel cell and gas turbine system combinations. A detailed thermodynamic cycle analysis tool has been developed to evaluate and compare the performance of these configurations. The development of this modelling tool was approached in four steps.

First, the thermodynamic and electrochemistry of a SOFC stack have been studied in details and a modelling approach devised. This tool was used to evaluate the impact of operating conditions such as operating temperature, pressure and air excess on the performance of the stack. Increasing operating temperature and pressure enhances efficiency. In addition, a higher pressure improves the electric power density while the air excess has a mild influence on the performance.

In a second step, the fuel processing aspects were considered in the modelling tool. Steam reforming and recirculation of water and fuel from the anode outlet prove to be very efficient with respect to increasing performance. The reformer analysis has shown that increasing its operating temperature, pressure and span has a beneficial impact on the amount of water required to perform an efficient methane conversion. Anode exhaust gas recirculation is a very important mean to improve performance of the stack-reformer system. On one hand, water recirculation at anode outlet allows to reduce the power required to heat up the input water to the operating temperature. On the other hand, recirculation of fuel contained in the anode gas reduces the amount of fuel to be injected in the reformer and allows to limit the air excess in the cycle required for ensuring a bounded inlet turbine temperature.

In a third stage, the modelling tool was enriched by auxiliaries models to analyze different layouts of full SOFC systems. It was demonstrated that a higher air excess negatively impacts the system efficiency mainly due to the power of the compressors while the stack performance is not improved by air excess.

Eventually, the modelling tool was used to analyze four different connections of SOFC with gas turbine. Essentially, the objective is to minimize the impact of the power of the compressors and heaters on the efficiency. Adding a turbine has proved to reduce the negative effect of the required compression power while introducing a bypass has allowed to limit the mass flow of air entering the cathode and therefore limit the power of the heaters. We concluded that an intercooled compressor stages configuration is interesting for high operating pressures.

This thesis is concluded by a short comparison of the mass of the various SOFC gas turbine configurations showing again that air excess should be limited as much

as possible.

As a general conclusion of this modelling exercise, the efficiency of a combined SOFC gas turbine combination can be as high as the theoretical stack efficiency provided that the gas turbine is essentially a turbocharger system and air excess is minimized.

The modelling tool developed in this master thesis is essentially steady state. It is known that the dynamics of such combined SOFC gas turbine systems is very complex and it would therefore be necessary to extend it to transient analysis and part load operations. Furthermore, more complex SOFC gas turbine combinations exist and could be worth analyzed.

Bibliography

[1] Hydrogen roadmap europe. Technical report, Fuel Cells and Hydrogen Joint Undertaking, 2019.

[2] A. Adnan Rashad, E. A. Rashad, A. A. Ali, E. Akram, M. M. Al-Rubaye, E. Yousif, and N. Hairunisa. Hydrogen in fuel cells: An overview of promotions and demotions. *Interdisciplinary Journal of Chemistry*, 2(2), 2017. ISSN 2398-7537.

[3] S. Assabumrungrat, N. Ruangrassamee, S. Vivanpatarakij, N. Laosiripojana, and A. Arpornwichanop. Influence of stack arrangement on performance of multiple-stack solid oxide fuel cells with non-uniform potential operation. *Journal of power sources*, 187(1):1–7, 2009. ISSN 0378-7753.

[4] S. Baba, S. Takahashi, N. Kobayashi, and S. Hirano. Evaluation of solid oxide fuel cell performance with anode recirculation using variable flow ejector at rated conditions. *Mechanical Engineering Journal*, 2(4):15–00087–15–00087, 2015. doi: 10.1299/mej.15-00087.

[5] L. Barelli, G. Bidini, and G. Cinti. Steam vs. dry reformer: Experimental study on a solid oxide fuel cell short stack. *Catalysts*, 8(12):599–, 2018. ISSN 2073-4344.

[6] S. Baudoin, I. Vechiu, H. Camblong, J.-M. Vinassa, and L. Barelli. Sizing and control of a solid oxide fuel cell/gas microturbine hybrid power system using a unique inverter for rural microgrid integration. *Applied energy*, 176:272–281, 2016. ISSN 0306-2619.

[7] M. Bianco, M. Linder, Y. Larring, F. Greco, and J. Van herle. Chapter 7 - lifetime issues for solid oxide fuel cell interconnects. In *Solid Oxide Fuel Cell Lifetime and Reliability*, pages 121–144. 2017. ISBN 0081011024.

[8] U. Bossel. Rapid startup sofc modules. *Energy procedia*, 28:48–56, 2012. ISSN 1876-6102.

[9] W. Bou Nader, F. Breque, Y. Mazloum, C. Dumand, and M. Nemer. Dynamic modelling and fuel consumption potential of an intercooled regenerative reheat gas turbine auxiliary power unit on series hybrid electric vehicle. *Journal of Energy Resources Technology*, 142, 2019. doi: 10.1115/1.4044366.

[10] W. Bou Nader, Y. Cheng, E. Nault, A. Reine, S. Wakim, B. Kabalan, and M. Nemer. Technological analysis and fuel consumption saving potential of different gas turbine thermodynamic configurations for series hybrid electric

vehicles. *Journal of Automobile Engineering*, 234(6):1544–1562, 2019. doi: 10.1177/0954407019890160.

[11] R. Bove, P. Lunghi, and N. M. Sammes. Sofc mathematic model for systems simulations. part one: from a micro-detailed to macro-black-box model. *International journal of hydrogen energy*, 30(2):181–187, 2005. doi: 10.1016/j.ijhydene.2004.04.008.

[12] R. Bove, P. Lunghi, and N. M. Sammes. Sofc mathematic model for systems simulations—part 2: definition of an analytical model. *International journal of hydrogen energy*, 30(2):189–200, 2005. doi: 10.1016/j.ijhydene.2004.04.018.

[13] A. Buonomano, F. Calise, M. D. d'Accadia, A. Palombo, and M. Vicidomini. Hybrid solid oxide fuel cells–gas turbine systems for combined heat and power: A review. *Applied energy*, 156:32–85, 2015. ISSN 0306-2619.

[14] F. Calise, M. Dentice d' Accadia, L. Vanoli, and M. von Spakovsky. Single-level optimization of a hybrid sofc–gt power plant. *Journal of power sources*, 159(2): 1169–1185, 2006. ISSN 0378-7753.

[15] M. S. Challiwala, M. M. Ghouri, D. Sengupta, M. M. El-Halwagi, and N. O. Elbashir. A process integration approach to the optimization of co2 utilization via tri-reforming of methane. In *Computer Aided Chemical Engineering*, volume 40, pages 1993–1998. 2017. ISBN 9780444639653.

[16] S. Chan, H. Ho, and Y. Tian. Modelling of simple hybrid solid oxide fuel cell and gas turbine power plant. *Journal of power sources*, 109(1):111–120, 2002. ISSN 0378-7753.

[17] J. Chen, J. Li, D. Zhou, H. Zhang, and S. Weng. Control strategy design for a sofc-gt hybrid system equipped with anode and cathode recirculation ejectors. *Applied thermal engineering*, 132:67–79, 2018. ISSN 1359-4311.

[18] P. Chinda and P. Brault. The hybrid solid oxide fuel cell (sofc) and gas turbine (gt) systems steady state modelling. *International journal of hydrogen energy*, 37(11):9237–9248, 2012. doi: 10.1016/j.ijhydene.2012.03.005.

[19] P. Chinda, S. Chanchaona, P. Brault, and W. Wechsatol. Mathematical modeling of a solid oxide fuel cell with nearly spherical-shaped electrode particles. *Journal of Sustainable Energy and Environment*, 1:185–196, 2010.

[20] P. Chinda, P. Brault, S. Chanchaona, and W. Wechsatol. A solid oxide fuel cell micro-scale modeling with spherical particle shaped electrodes. *The European Physical Journal Applied Physics*, 54(2), 2011. doi: 10.1051/epjap/2011100171.

[21] P. Chinda, W. Wechsatol, S. Chanchaona, and P. Brault. Microscale modeling of an anode-supported planar solid oxide fuel cell. *Fuel cells (Weinheim an der Bergstrasse, Germany)*, 11(2):184–199, 2011. doi: 10.1002/fuce.201000121.

[22] M. Cimenti and J. M. Hill. Direct utilization of liquid fuels in sofc for portable applications: Challenges for the selection of alternative anodes. *Energies (Basel)*, 2(2):377–410, 2009. ISSN 1996-1073.

[23] C. O. Colpan, I. Dincer, and F. Hamdullahpur. Thermodynamic modeling of direct internal reforming solid oxide fuel cells operating with syngas. *International journal of hydrogen energy*, 32(7):787–795, 2007. ISSN 0360-3199.

[24] C. O. Colpan, I. Dincer, and F. Hamdullahpur. A review on macro-level modeling of planar solid oxide fuel cells. *International journal of energy research*, 32(4):336–355, 2008. doi: 10.1002/er.1363.

[25] P. Costamagna, F. Pugliese, T. Cavattoni, G. Busca, and G. Garbarino. Modeling of laboratory steam methane reforming and co2 methanation reactors. *Energies (Basel)*, 13(10):2624–, 2020. ISSN 1996-1073.

[26] J. P. F. de Medeiros, V. da Fonseca Dias, J. M. da Silva, and J. D. da Silva. Thermochemical performance analysis of the steam reforming of methane in a fixed bed membrane reformer: A modelling and simulation study. *Membranes (Basel)*, 11(1):6–, 2020. ISSN 2077-0375.

[27] M. Delanaye, 2021. Private communication.

[28] M. Dillig and J. Karl. Thermal management of high temperature solid oxide electrolyser cell/fuel cell systems. *Energy procedia*, 28:37–47, 2012. ISSN 1876-6102.

[29] H. Ding, Y. Xie, and X. Xue. Electrochemical performance of bazr0.1ce0.7y0.1yb0.1o3 electrolyte based proton-conducting sofc solid oxide fuel cell with layered perovskite prbaco2o5+ cathode. *Journal of power sources*, 196(5):2602–2607, 2011. ISSN 0378-7753.

[30] N. Duc Tuyen. Modelling a sofc power unit using natural gas fed directly. 2012. doi: 10.5772/36376.

[31] P. Duysinx. *Electric, hybrid and fuel cell vehicles (MECA0527)*. University of Liege, 2020-2021.

[32] S. Dyzak. *Brennstoffzellen–Heizungen : Technologie, Marktüberblick, Forderüng*. SOLIDpower, 2016.

[33] Elcogen. Solid oxide cell stack. URL `https://elcogen.com/products/solid-oxide-cell-stacks/`. (accessed: 03/06/21).

[34] Q. Fu, P. Freundt, J. Bomhard, and F. Hauler. Sofc stacks operating under direct internal steam reforming of methane. 17(2):151–156, 2017. ISSN 1615-6846.

[35] M. Hanasaki, C. Uryu, T. Daio, T. Kawabata, Y. Tachikawa, S. M. Lyth, Y. Shiratori, S. Taniguchi, and K. Sasaki. Sofc durability against standby and shutdown cycling. *Journal of the Electrochemical Society*, 161(9):F850–F860, 2014. ISSN 0013-4651.

[36] W. He, K. J. Yoon, R. S. Eriksen, S. Gopalan, S. N. Basu, and U. B. Pal. Out-of-cell measurements of h2-h2o effective binary diffusivity in the porous anode of solid oxide fuel cells (sofcs). *Journal of power sources*, 195(2):532–535, 2010. ISSN 0378-7753.

[37] C. Hester. Reformer model. URL https://www.youtube.com/watch?v=WFCC79Ytuj4&t=202s&ab_channel=CodyHester.

[38] M. Heylen. Interpolation of component characteristic maps for thermodynamic cycle assessment. Technical report, University of Liège, 2020.

[39] Y. Hiei, T. Ishihara, and Y. Takita. Partial oxidation of methane for internally reformed solid oxide fuel cell. *Solid state ionics*, 86(2):1267–1272, 1996. ISSN 0167-2738.

[40] M. Hohloch, M. Herbst, A. Marcellan, T. Lingstädt, T. Krummrein, M. Aigner, and M. Henke. Control strategy for a sofc micro gas turbine hybrid power plant emulator test rig. *E3S web of conferences*, 2019. doi: 10.2514/6.2019-1676.

[41] N. Job. *Electrochemical energy conversion and storage (CHIM0664)*. University of Liege, 2020-2021.

[42] D. Kanno, N. Shikazono, N. Takagi, K. Matsuzaki, and N. Kasagi. Evaluation of sofc anode polarization simulation using three-dimensional microstructures reconstructed by fib tomography. *Electrochimica acta*, 56(11):4015–4021, 2011. ISSN 0013-4686.

[43] Y. Lin and S. Beale. Performance predictions in solid oxide fuel cells. *Applied mathematical modelling*, 30(11):1485–1496, 2006. doi: 10.1016/j.apm.2006.03.009.

[44] B. Lindström, J. Karlsson, P. Ekdunge, L. De Verdier, B. Häggendal, J. Dawody, M. Nilsson, and L. Pettersson. Diesel fuel reformer for automotive fuel cell applications. *International journal of hydrogen energy*, 34(8):3367–3381, 2009. ISSN 0360-3199.

[45] V. Liso, A. C. Olesen, M. P. Nielsen, and S. K. Kær. Performance comparison between partial oxidation and methane steam reforming processes for solid oxide fuel cell (sofc) micro combined heat and power (chp) system. *Energy (Oxford)*, 36(7):4216–4226, 2011. ISSN 0360-5442.

[46] M. Liu, A. Lanzini, W. Halliop, V. Cobas, A. Verkooijen, and P. Aravind. Anode recirculation behavior of a solid oxide fuel cell system: A safety analysis and a performance optimization. *International journal of hydrogen energy*, 38 (6):2868–2883, 2013. ISSN 0360-3199.

[47] F. Manenti, R. Pelosato, P. Vallevi, A. R. Leon-Garzon, G. Dotelli, A. Vita, M. Lo Faro, G. Maggio, L. Pino, and A. S. Aricò. Biogas-fed solid oxide fuel cell (sofc) coupled to tri-reforming process: Modelling and simulation. *International journal of hydrogen energy*, 40(42):14640–14650, 2015. ISSN 0360-3199.

[48] X. Mao, T. Yu, and G. Ma. Performance of cobalt-free double-perovskite ndbafe2xmnxo5+ cathode materials for proton-conducting it-sofc. *Journal of alloys and compounds*, 637:286–290, 2015. ISSN 0925-8388.

[49] Matlab. URL https://nl.mathworks.com/matlabcentral/fileexchange/26492-combustion-toolbox. (accessed: 06/06/21).

[50] S. J. McPhail, J. Kiviaho, and B. Conti. The yellow pages of sofc technology. Technical report, International Energy Agency, 2017.

[51] MITIS. URL https://www.mitis.be/. (accessed: 03/06/21).

[52] S. Mohammed, A. Hussin, A. Alameen, R. Mohammed, and K. Wagialla. Production of hydrogen through methane steam reforming in a fixed bed reactor using matlab simulation. 4:7–12, 2014.

[53] mPower GmbH. Product specification. URL http://mpowergmbh.de/productandtechnology.html#sofc. (accessed: 03/06/21).

[54] NEXCERIS. URL https://nexceris.com/solutions/solid-oxide-fuel-cells/. (accessed: 06/06/21).

[55] M. Noponen. Elcogen sofc technology. Technical report, Elcogen, 2019.

[56] J. Pan, J. Yang, D. Yan, J. Pu, B. Chi, and J. Li. Effect of thermal cycling on durability of a solid oxide fuel cell stack with external manifold structure. *International journal of hydrogen energy*, 45(35):17927–17934, 2020. ISSN 0360-3199.

[57] D. Papurello, A. Lanzini, F. Smeacetto, L. Tognana, S. Silvestri, F. Biasioli, and M. Santarelli. Effect of sulfur and carbon contaminants on a solid oxide fuel cell (sofc) fed with anaerobic digestion biogas. 2013.

[58] R. Peters, R. Deja, M. Engelbracht, M. Frank, V. N. Nguyen, L. Blum, and D. Stolten. Efficiency analysis of a hydrogen-fueled solid oxide fuel cell system with anode off-gas recirculation. *Journal of power sources*, 328:105–113, 2016. ISSN 0378-7753.

[59] V. Ramireddy. Getting electricity from solid oxide fuel cell. URL https://electrical-engineering-portal.com/getting-electricity-from-solid-oxide-fuel-cell.

[60] M. Schwaab, A. L. Alberton, C. E. Fontes, R. C. Bittencourt, and J. C. Pinto. Hybrid modeling of methane reformers. 2. modeling of the industrial reactors. *Industrial engineering chemistry research*, 48(21):9376–9382, 2009. ISSN 0888-5885.

[61] J. L. Silveira. *Sustainable Hydrogen Production Processes: Energy, Economic and Ecological Issues*. Green Energy and Technology. ISBN 3319416146.

[62] SOFCMAN. Sofcman-asc 30-cell stack module-700w. URL http://www.sofcman.com/700w.asp. (accessed: 03/06/21).

[63] S. Souentie, M. Athanasiou, D. Niakolas, A. Katsaounis, S. Neophytides, and C. Vayenas. Mathematical modeling of ni/gdc and au–ni/gdc sofc anodes performance under internal methane steam reforming conditions. *Journal of catalysis*, 306:116–128, 2013. ISSN 0021-9517.

[64] S. Su, X. Gao, Q. Zhang, W. Kong, and D. Chen. Anode-versus cathode-supported solid oxide fuel cell: Effect of cell design on the stack performance. *International journal of electrochemical science*, 10(3):2487–2503, 2015. ISSN 1452-3981.

[65] K. Takino, Y. Tachikawa, K. Mori, S. Lyth, Y. Shiratori, S. Taniguchi, and K. Sasaki. Simulation of sofc performance using a modified exchange current density for pre-reformed methane-based fuels. *International journal of hydrogen energy*, 45(11):6912–6925, 2020. ISSN 0360-3199.

[66] Y. Tanaka, T. Terayama, A. Momma, and T. Kato. Numerical simulation of sofc system performance at 90% fuel utilization with or without anode off-gas recycle for enhancing efficiency. *Meeting abstracts (Electrochemical Society)*, 68 (1):293–300, 2015. ISSN 2151-2043.

[67] X. Wang, X. Lv, and Y. Weng. Performance analysis of a biogas-fueled sofc/gt hybrid system integrated with anode-combustor exhaust gas recirculation loops. *Energy (Oxford)*, 197:117213–, 2020. ISSN 0360-5442.

[68] W. Winkler. 3 - thermodynamics. In *High-temperature Solid Oxide Fuel Cells for the 21st Century*, pages 51–83. Second edition edition, 2015. ISBN 9780124104839.

[69] C.-C. Wu and T.-L. Chen. Dynamic modeling of a parallel-connected solid oxide fuel cell stack system. *Energies (Basel)*, 13(2):501–, 2020. ISSN 1996-1073.

[70] T. Yonekura, Y. Tachikawa, T. Yoshizumi, Y. Shiratori, K. Ito, and K. Sasaki. Exchange current density of solid oxide fuel cell electrodes. *ECS Transactions*, 35(1):1007–1014, 2019. doi: 10.1149/1.3570081.

[71] F. Zabihian and A. S. Fung. Macro-level modeling of solid oxide fuel cells, approaches, and assumptions revisited. *Journal of renewable and sustainable energy*, 9(5):54301–, 2017. ISSN 1941-7012.

[72] L. Zhang, Y. Xing, H. Xu, H. Wang, J. Zhong, and J. Xuan. Comparative study of solid oxide fuel cell combined heat and power system with multi-stage exhaust chemical energy recycling: Modeling, experiment and optimization. *Energy conversion and management*, 139:79–88, 2017. ISSN 0196-8904.

[73] F. Zink, Y. Lu, and L. Schaefer. A solid oxide fuel cell system for buildings. *Energy conversion and management*, 48(3):809–818, 2007. ISSN 0196-8904.

Appendix A

Simulation tool details

A.1 Code principle

This section describes the implementation of the code which is composed of four nested loops (Fig. A.1):

- Loop 1 iterates on the air excess to limit the inlet turbine temperature.
- Loop 2 increases gradually the mass flow of fuel to reach the targeted power at a fixed current density which avoids specifying the mass flow of fuel as input.
- Loop 3 concerns the anode gas recirculation and converges on the reformer output.
- Loop 4 increases the mass flow of water in the reformer to target a 95% conversion ratio.

The parameters, inputs and outputs are specified as follows:

Parameters	Internal SOFC	/
	Auxiliaries	/
	...	/
Inputs	Targeted power	$P_{el,target}$
	Specified current density	i
	Operating temperature	T
	Operating pressure	p_t
	Fuel utilization	U_f
	Recirculation ratio	R_R
	Inlet temperatures of air/fuel/water	$T_{air,i}/T_{fuel,i}/T_{water,i}$
	Inlet pressures of air/fuel/water	$p_{air,i}/p_{fuel,i}/p_{water,i}$
Outputs	Output voltage	V_o
	Electric power density	p_{el}
	Electric power	P_{el}
	Number of cells	N_{cells}
	SOFC stack efficiency	η_{Stack}
	System efficiency	η_{Syst}
	Generated heat	Q_{FC}

Table A.1: Parameters, inputs and outputs of the modelling.

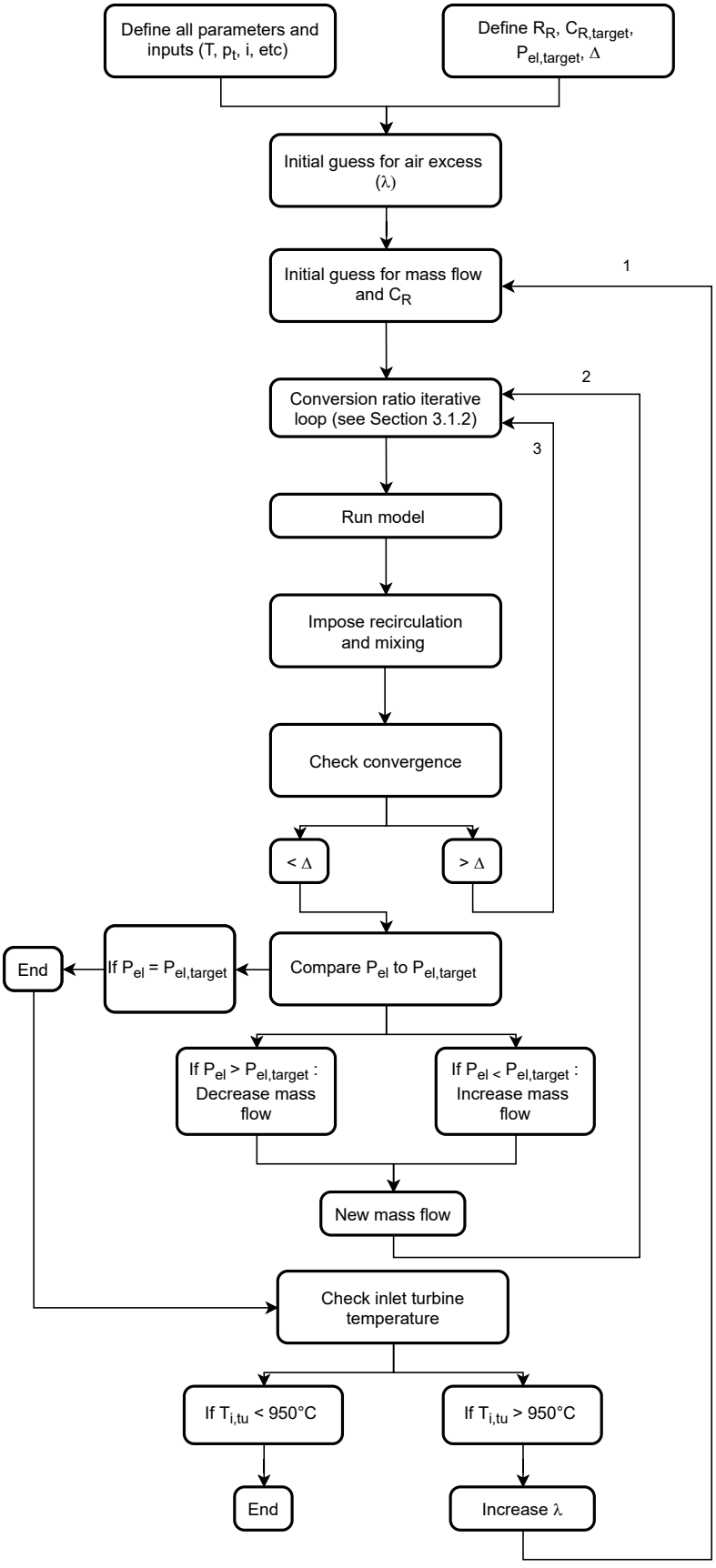

Figure A.1: Flowchart of the code implementation.

A.2 REFPROP

The thermodynamic properties required in the MATLAB implementation of the modelling tool are calculated by the REFPROP 9.1 package linked to MATLAB. In REFPROP 9.1, we found out that thermodynamic tables have temperature limits which prevents to calculate these properties above the limit. Hence, for a temperature above the limit, a linear extrapolation is performed to obtain the thermodynamic property of interest.

Appendix B

SOFC analysis

B.1 Temperature

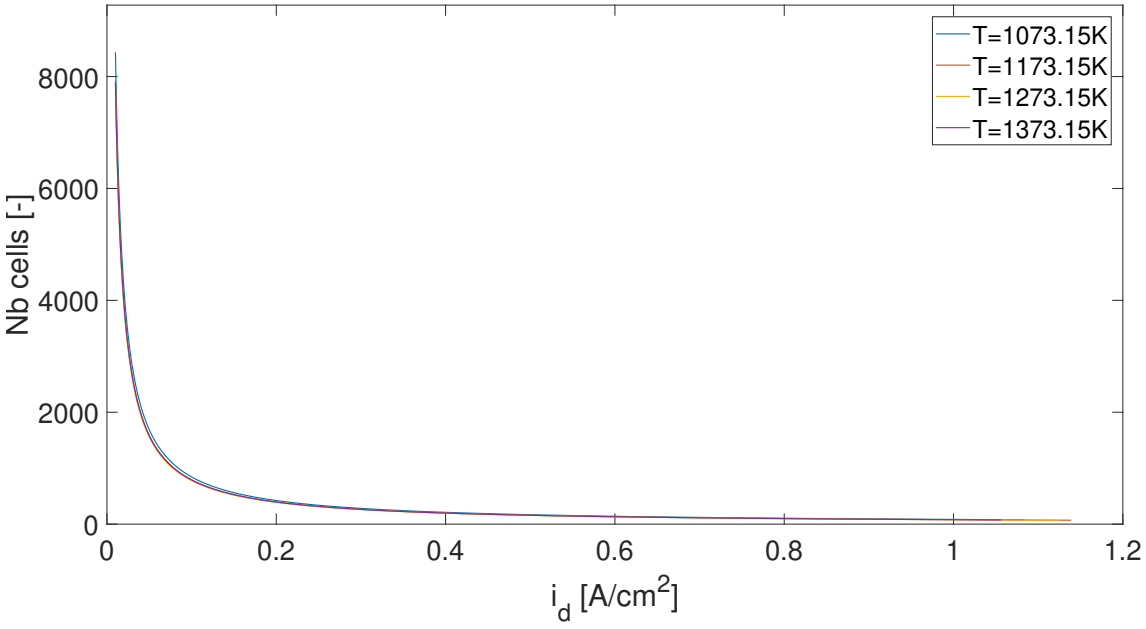

Figure B.1: Number of cells [-] as a function of the current density [A/cm²] for different temperatures (p_t = 200 [kPa], U_f = 0.7 [-], λ = 1.5 [-], $\dot{m}_{CH_4}$ = 3.2E-4 [kg/s], $\dot{m}_{H_2O}$ = 4.95E-4 [kg/s]).

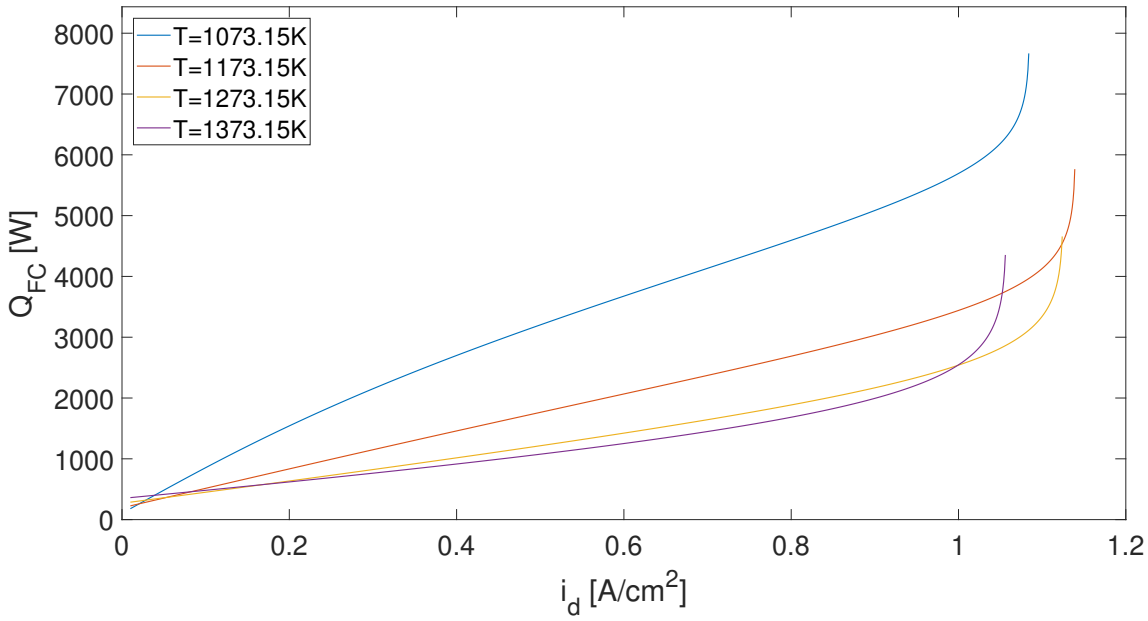

Figure B.2: Generated heat [W] as a function of the current density [A/cm²] for different temperatures (p_t = 200 [kPa], U_f = 0.7 [-], λ = 1.5 [-], $\dot{m}_{CH_4}$ = 3.2E-4 [kg/s], $\dot{m}_{H_2O}$ = 4.95E-4 [kg/s]).

B.2 Pressure

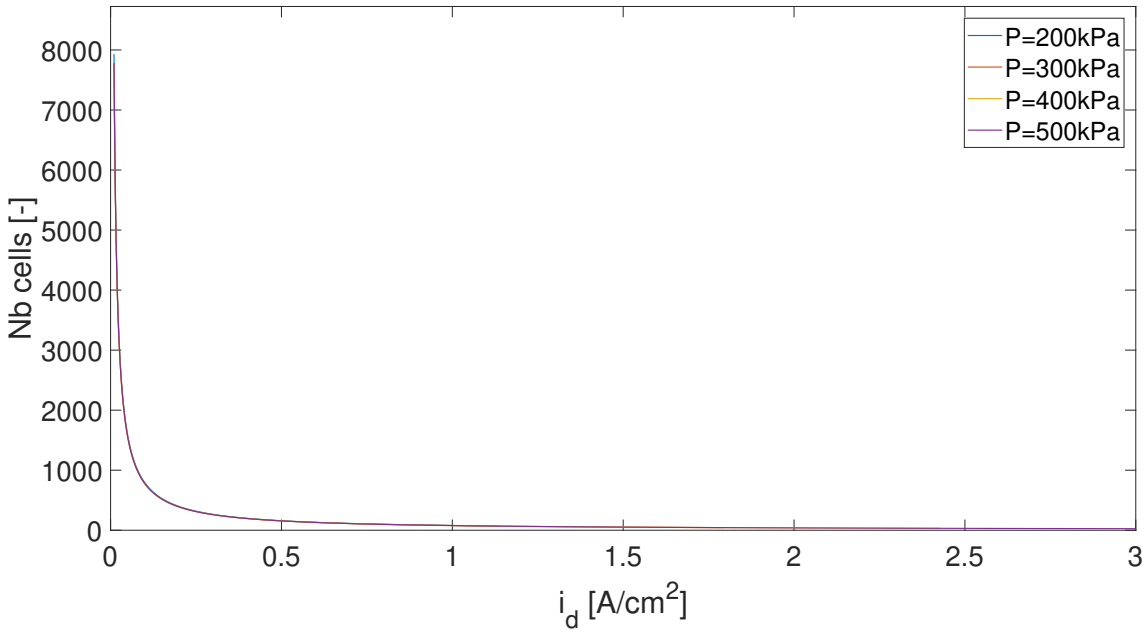

Figure B.3: Number of cells [-] as a function of the current density [A/cm²] for different pressures (T = 1173.15 [K], U_f = 0.7 [-], λ = 1.5 [-], $\dot{m}_{CH_4}$ = 3.2E-4 [kg/s], $\dot{m}_{H_2O}$ = 4.95E-4 [kg/s]).

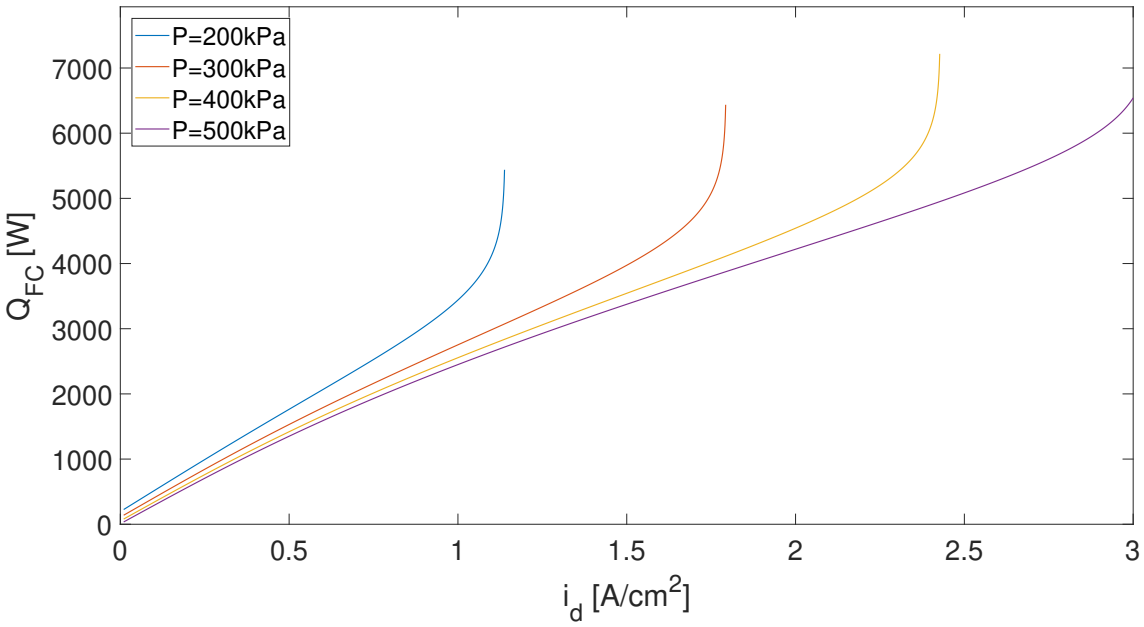

Figure B.4: Generated heat [W] as a function of the current density [A/cm^2] for different pressures ($T = 1173.15$ [K], $U_f = 0.7$ [-], $\lambda = 1.5$ [-], $\dot{m}_{CH_4} = 3.2\text{E-}4$ [kg/s], $\dot{m}_{H_2O} = 4.95\text{E-}4$ [kg/s]).

B.3 Air excess

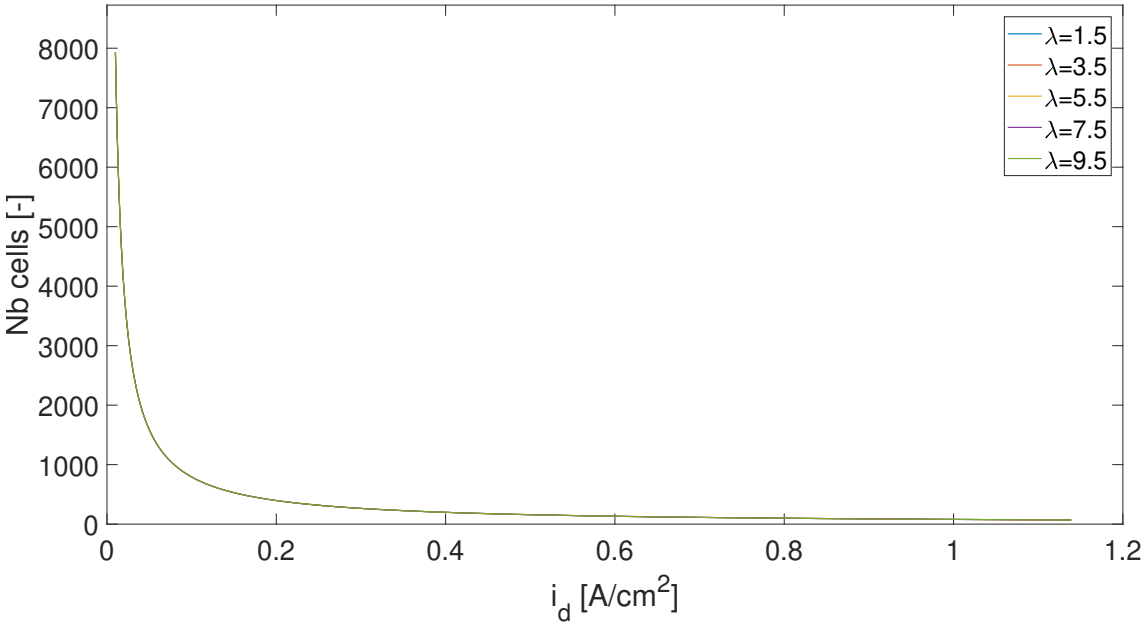

Figure B.5: Number of cells [-] as a function of the current density [A/cm^2] for different air excesses ($T = 1173.15$ [K], $p_t = 200$ [kPa], $U_f = 0.7$, $\dot{m}_{CH_4} = 3.2\text{E-}4$ [kg/s], $\dot{m}_{H_2O} = 4.95\text{E-}4$ [kg/s]).

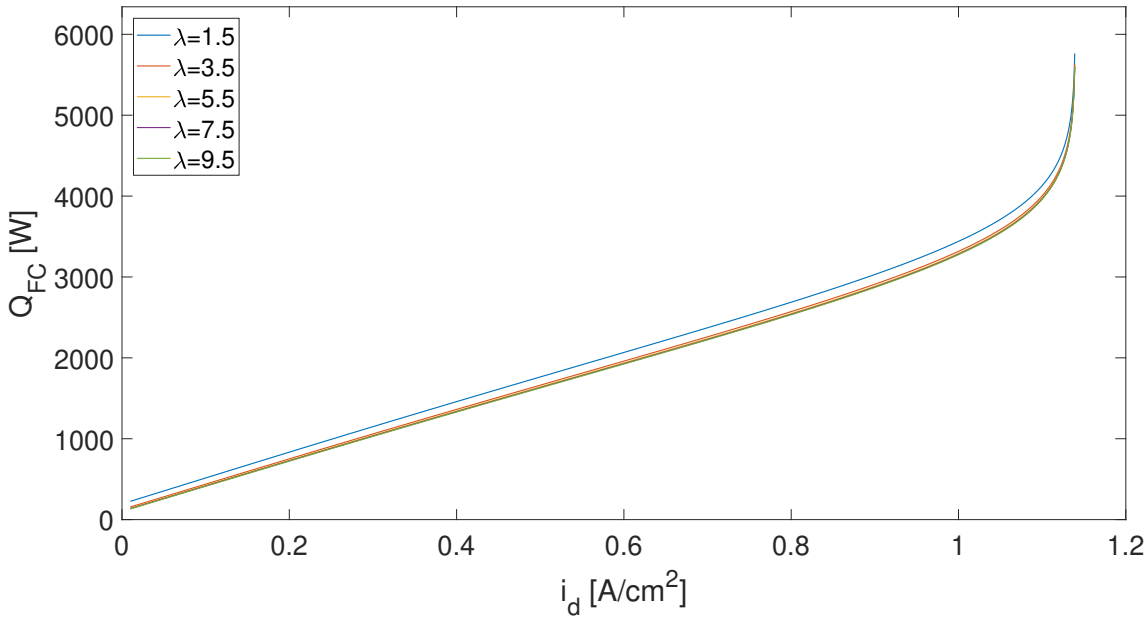

Figure B.6: Generated heat [W] as a function of the current density [A/cm^2] for different air excesses (T = 1173.15 [K], p_t = 200 [kPa], U_f = 0.7, $\dot{m}_{CH_4}$ = 3.2E-4 [kg/s], $\dot{m}_{H_2O}$ = 4.95E-4 [kg/s]).

Appendix C

Anode recirculation

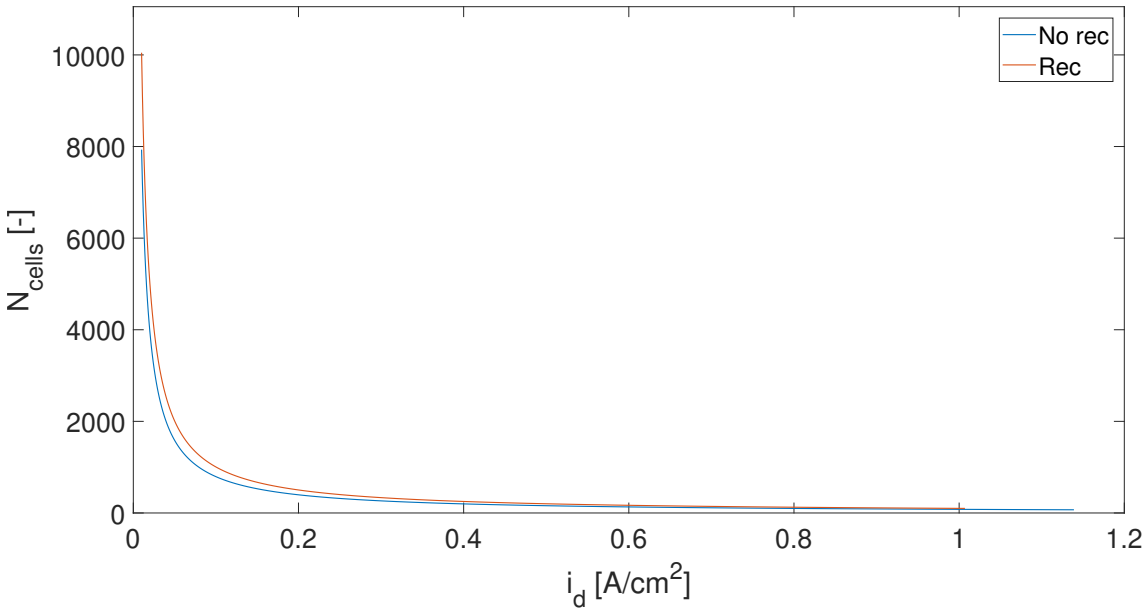

Figure C.1: Number of cells [-] as a function of the current density [A/cm²] with recirculation and without recirculation at the anode. ($R_R = 0.7$ [-], $T = 1173.15$ [K], $p_t = 200$ [kPa], $U_f = 0.7$ [-], $\lambda = 1.5$ [-], $\dot{m}_{CH_4} = 3.2\text{E-}4$ [kg/s], $\dot{m}_{H_2O,NR} = 4.95\text{E-}4$ [kg/s], $\dot{m}_{H_2O,R} = 6.68\text{E-}4$ [kg/s]).

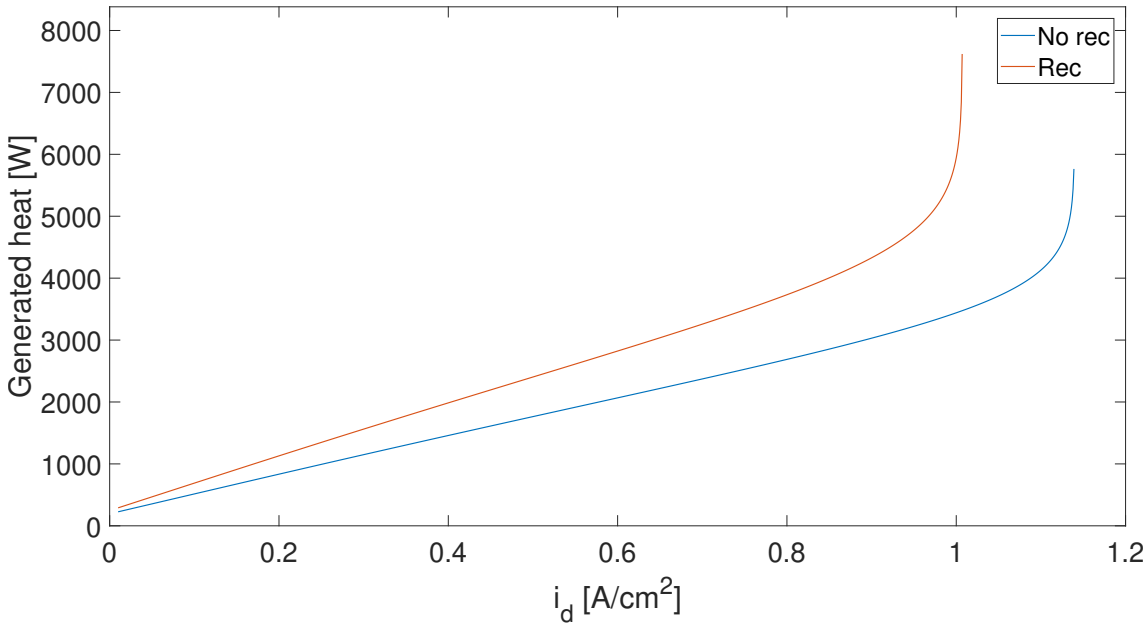

Figure C.2: Generated heat [-] as a function of the current density [A/cm²] with recirculation and without recirculation at the anode. ($R_R = 0.7$ [-], $T = 1173.15$ [K], $p_t = 200$ [kPa], $U_f = 0.7$ [-], $\lambda = 1.5$ [-], $\dot{m}_{CH_4} = 3.2\text{E-}4$ [kg/s], $\dot{m}_{H_2O,NR} = 4.95\text{E-}4$ [kg/s], $\dot{m}_{H_2O,R} = 6.68\text{E-}4$ [kg/s]).

Appendix D

SOFC system analysis

D.1 Temperature

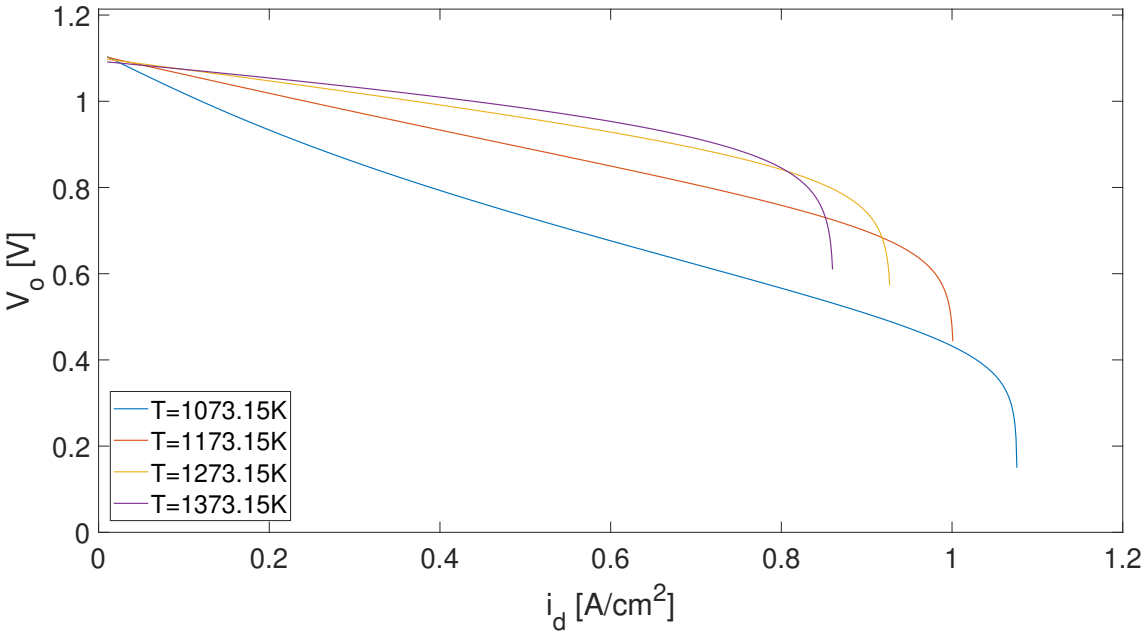

Figure D.1: Output voltage [V] as a function of the current density [A/cm^2] for different temperatures. (R_R = 0.7 [-], p_t = 200 [kPa], U_f = 0.7 [-], λ = 1.5 [-], $\dot{m}_{CH_4}$ = 3.4E-4 [kg/s], $\dot{m}_{H_2O,NR}$ = 8.1E-5 [kg/s]).

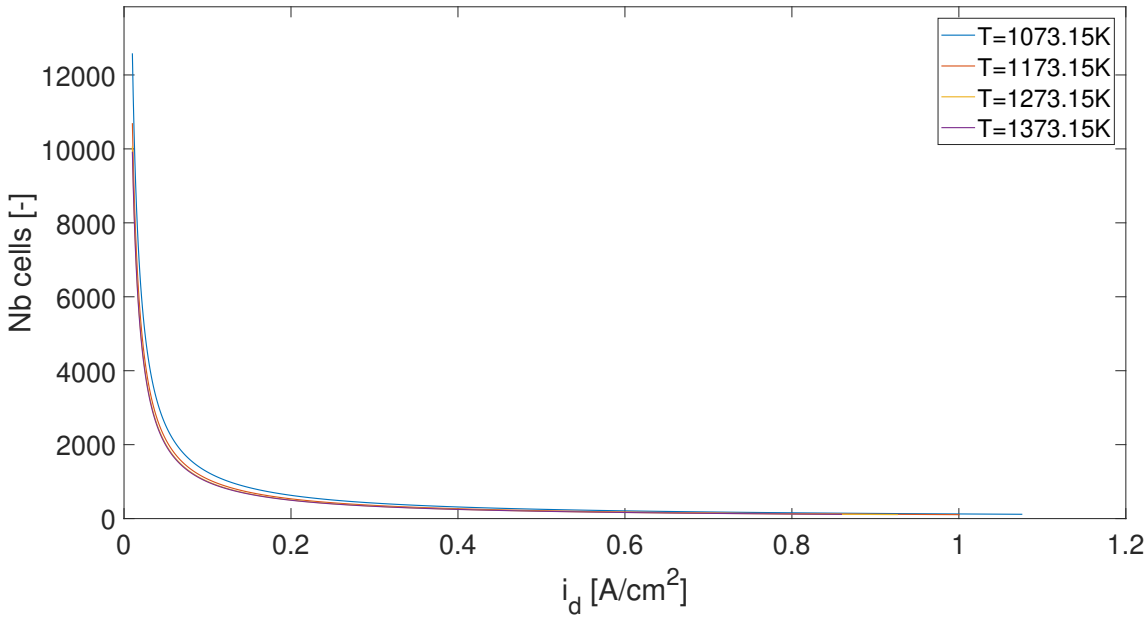

Figure D.2: Number of cells [-] as a function of the current density [A/cm²] for different temperatures. (R_R = 0.7 [-], p_t = 200 [kPa], U_f = 0.7 [-], λ = 1.5 [-], $\dot{m}_{CH_4}$ = 3.4E-4 [kg/s], $\dot{m}_{H_2O,NR}$ = 8.1E-5 [kg/s]).

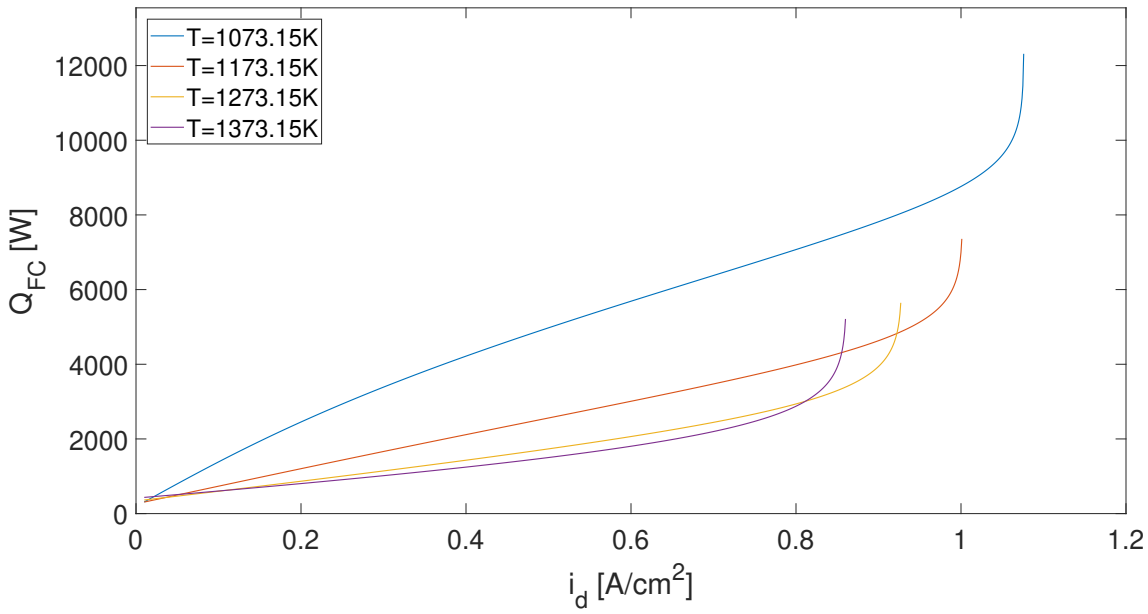

Figure D.3: Generated heat [W] as a function of the current density [A/cm²] for different temperatures. (R_R = 0.7 [-], p_t = 200 [kPa], U_f = 0.7 [-], λ = 1.5 [-], $\dot{m}_{CH_4}$ = 3.4E-4 [kg/s], $\dot{m}_{H_2O,NR}$ = 8.1E-5 [kg/s]).

D.2 Pressure

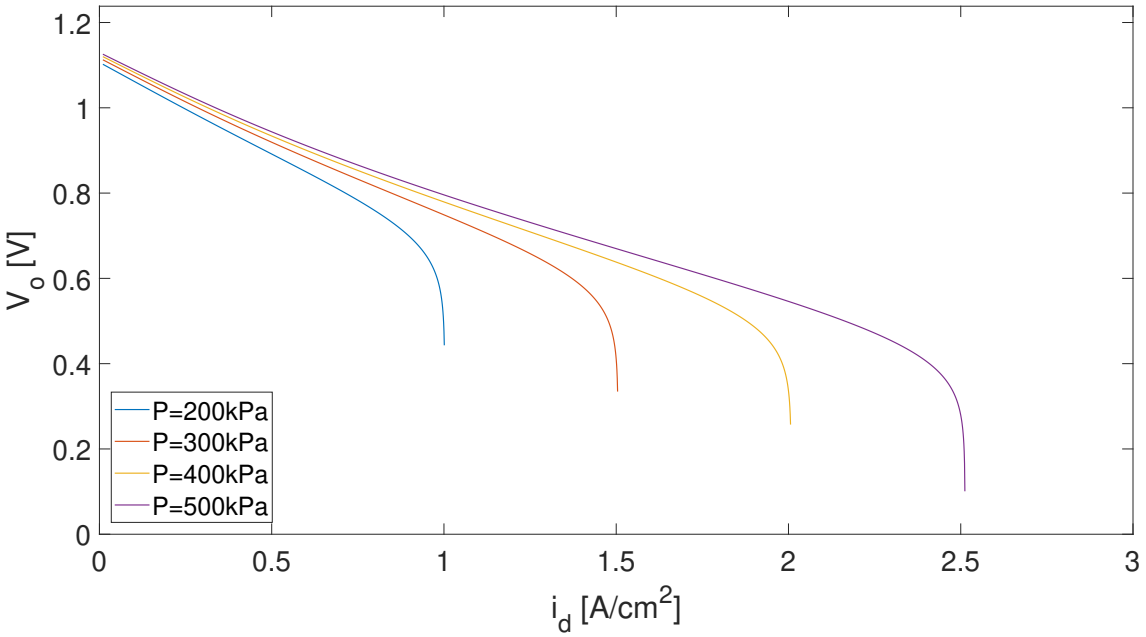

Figure D.4: Output voltage [V] as a function of the current density [A/cm²] for different pressures. (R_R = 0.7 [-], T = 1173.15 [K], U_f = 0.7 [-], λ = 1.5 [-], $\dot{m}_{CH_4}$ = 3.4E-4 [kg/s], $\dot{m}_{H_2O,NR}$ = 8.1E-5 [kg/s]).

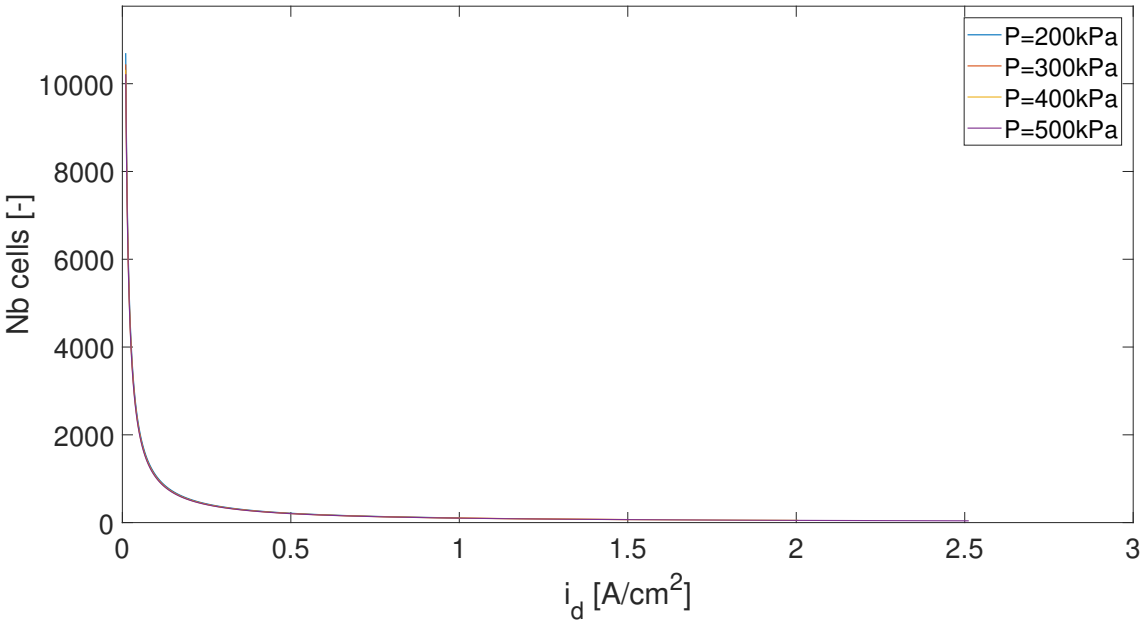

Figure D.5: Number of cells [-] as a function of the current density [A/cm²] for different pressures. (R_R = 0.7 [-], T = 1173.15 [K], U_f = 0.7 [-], λ = 1.5 [-], $\dot{m}_{CH_4}$ = 3.4E-4 [kg/s], $\dot{m}_{H_2O,NR}$ = 8.1E-5 [kg/s]).

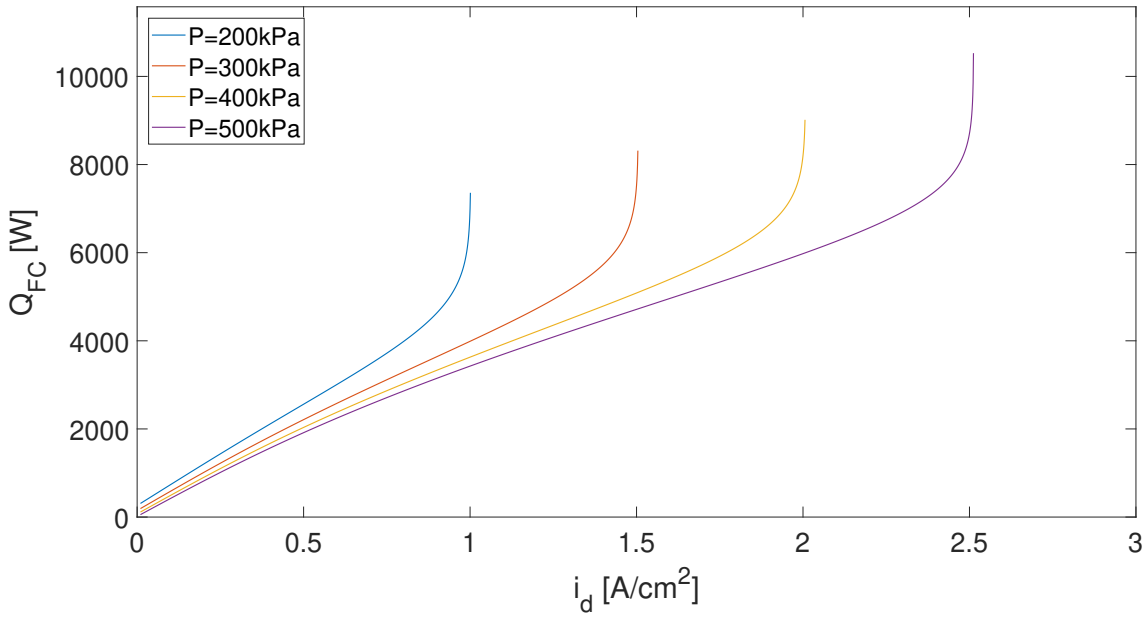

Figure D.6: Generated heat [W] as a function of the current density [A/cm^2] for different pressures. (R_R = 0.7 [-], T = 1173.15 [K], U_f = 0.7 [-], λ = 1.5 [-], $\dot{m}_{CH_4}$ = 3.4E-4 [kg/s], $\dot{m}_{H_2O,NR}$ = 8.1E-5 [kg/s]).

D.3 Air excess

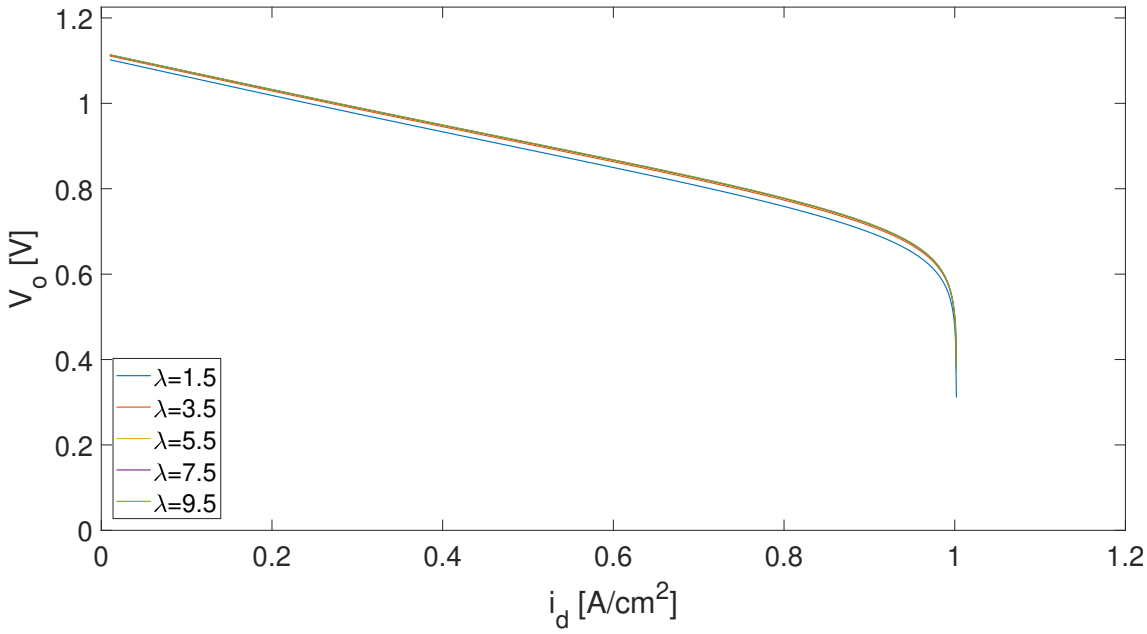

Figure D.7: Output voltage [V] as a function of the current density [A/cm^2] for different air excesses. (R_R = 0.7 [-], T = 1173.15 [K], p_t = 200 [kPa], U_f = 0.7 [-], $\dot{m}_{CH_4}$ = 3.4E-4 [kg/s], $\dot{m}_{H_2O,NR}$ = 8.1E-5 [kg/s]).

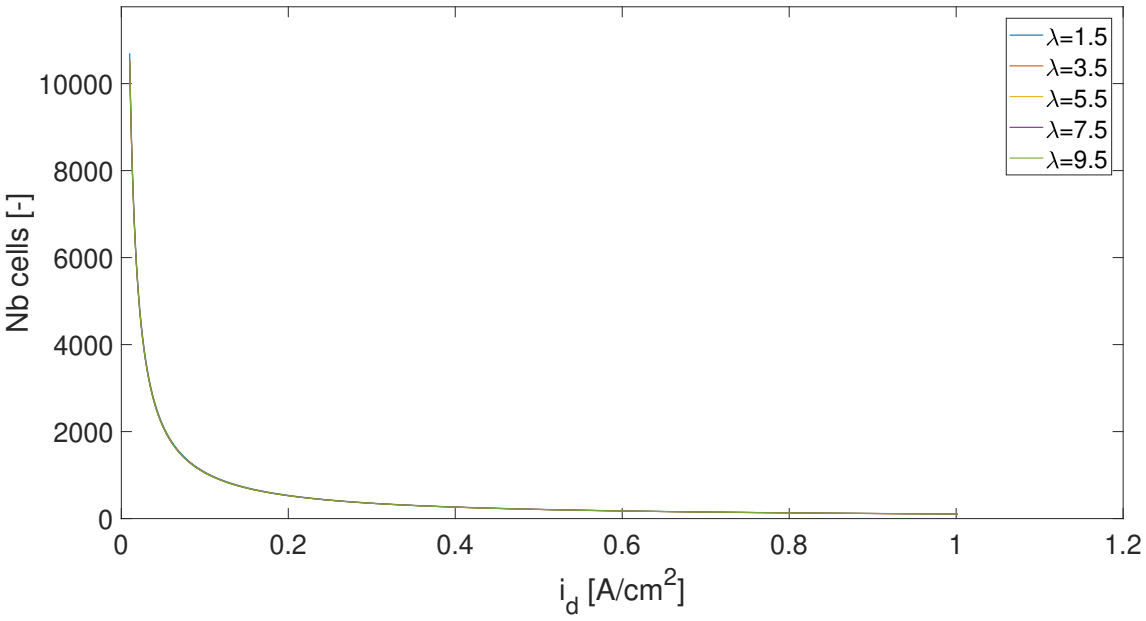

Figure D.8: Number of cells [-] as a function of the current density [A/cm²] for different air excesses. (R_R = 0.7 [-], T = 1173.15 [K], p_t = 200 [kPa], U_f = 0.7 [-], $\dot{m}_{CH_4}$ = 3.4E-4 [kg/s], $\dot{m}_{H_2O,NR}$ = 8.1E-5 [kg/s]).

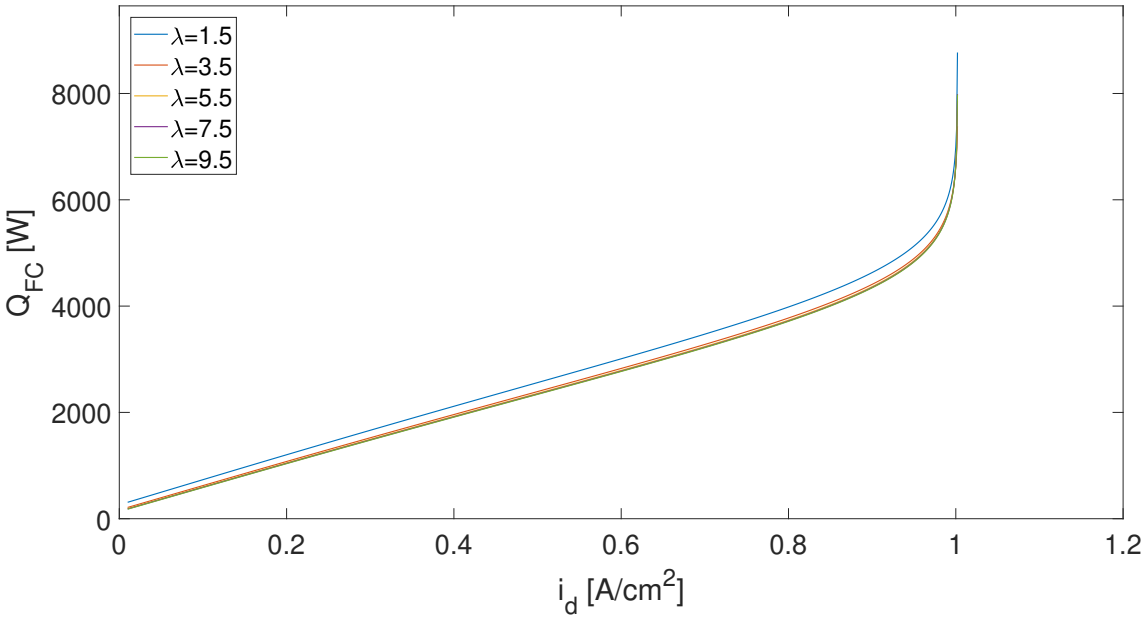

Figure D.9: Generated heat [W] as a function of the current density [A/cm²] for different air excesses. (R_R = 0.7 [-], T = 1173.15 [K], p_t = 200 [kPa], U_f = 0.7 [-], $\dot{m}_{CH_4}$ = 3.4E-4 [kg/s], $\dot{m}_{H_2O,NR}$ = 8.1E-5 [kg/s]).